Table of Contents

List of Figures

List of Tables

Glossary

cAMP	Adenosine 3',5'-cyclic monophosphate
AP	Action potential
AR	Adrenergic receptor
BDM	2,3-butanedione monoxime
CaN	Calcineurin
CaMKIIδ	Ca^{2+}/calmodulin-dependent protein kinase IIδ
CICR	Ca^{2+}-induced Ca^{2+} release
CSV	Comma-separated variables
DHPRs	Dihydropyridine receptors
DMSO	Dimethyl sulphoxide
EC	Excitation-contraction
FFR	Force-frequency relationship
HEPES	4-(2-hydroxyethyl)-1-piperazineethanesulfonic acid
ISO	Isoproterenol
I-V	Current-voltage
KB	Kraft-Brühe
LCC	*L*-type Ca^{2+} channel
LV	Left ventricle
NCX	Na^{+}- Ca^{2+} exchanger
NE	Norepinephrine
PKA	cAMP-dependent protein kinase
PKC	Protein kinase C
PKG	Protein kinase G
RV	Right ventricle
RT_{50}	Time from peak force to 50% relaxation

RYR	Ryanodine receptor
SA	Sinoatrial
SFR	Stress-frequency relationship
SR	Sarcoplasmic reticulum
SERCA	SR Ca^{2+} pump
TD	Twitch duration
Tm	Tropomyosin
TnC	Troponin C
TnI	Troponin I
TnT	Troponin T
TPF	Time to peak force

Chapter 1

Introduction

To understand the fundamental properties of the heart itself and how nervous and mechanical mechanisms modify or control cardiac function firstly requires an investigation of ventricular contractility in terms of mechanical and electrophysiological properties. Only then can we assess the pathophysiological mechanisms underlying cardiovascular diseases. Ventricular wall stress provides a fundamental measure of the underlying ventricular mechanics. Different stresses acting in the ventricular walls may reflect different contractile properties between left and right ventricles in a normal heart as well as reflecting the different ventricular pressures. To date, there have been no studies that have systematically examined the differences in stresses between isolated left and right ventricular muscles under physiological conditions. This study compared two fundamental processes that differently regulate left and right ventricular mechanics and investigated the contributions to these of various subcellular processes.

1.1 Basic Heart Physiology

The heart is a mechanical pump for the circulation of blood to the whole body. This modern concept of circulation (Figure 1.1) was proposed by William Harvey (1578-1657) as an alternative to the ancient concept of “vital spirit”. Since then, a variety of discoveries relating to the physiology and pathophysiology of the heart have brought us a substantial understanding of heart function and insights that can help solve the problem of cardiovascular disease.

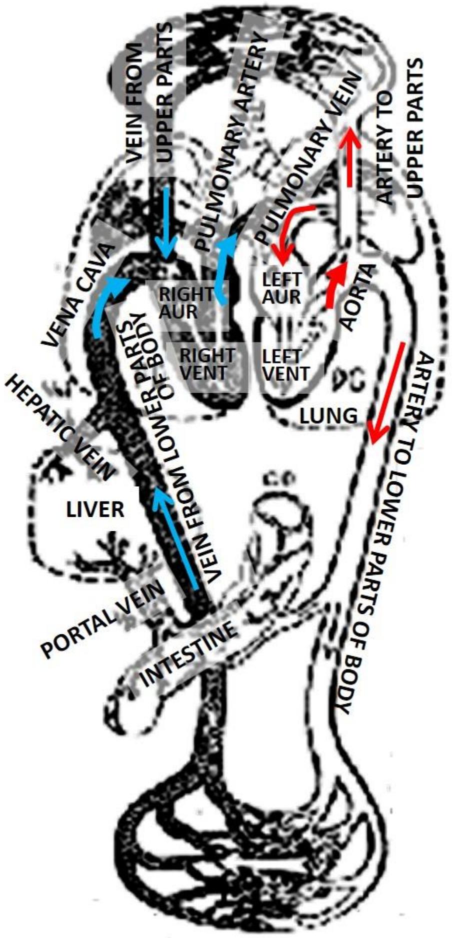

Figure 1.1. The heart and normal circulation of the human body, as modified from “Anatomical Treatise on the Motion of the Heart and Blood in Animals (1628)”. Harvey provided the foundation for our understanding of normal blood circulation - arteries and veins are functionally connected in the lungs and the peripheral tissues - and of the presence of valves in the veins for circulation toward the heart.

1.1.1 Basic Functioning of the Heart

The pumping of the heart is not simple as the action of cardiac contraction needs to be coordinated through synchronicity of the discrete regions of the heart including its electrical activity and mechanical coupling. Ventricular contraction is required for the proper functioning of both the pulmonary and the systemic circulations. Consequently, the wall of the left ventricle is thicker than that of the right ventricle to respond to the higher pressures in the aorta and left ventricle (LV) than in the pulmonary artery and right ventricle (RV).

The basic phases of the cardiac cycle are (i) ventricular filling, (ii) isovolumic contraction, (iii) ejection, and (iv) isovolumic relaxation, which generate the pressure to pump blood received from the lungs to the body via the aorta in the left heart, and to propel blood received from the body to the lungs via the pulmonary artery in the right heart (Figure 1.2).

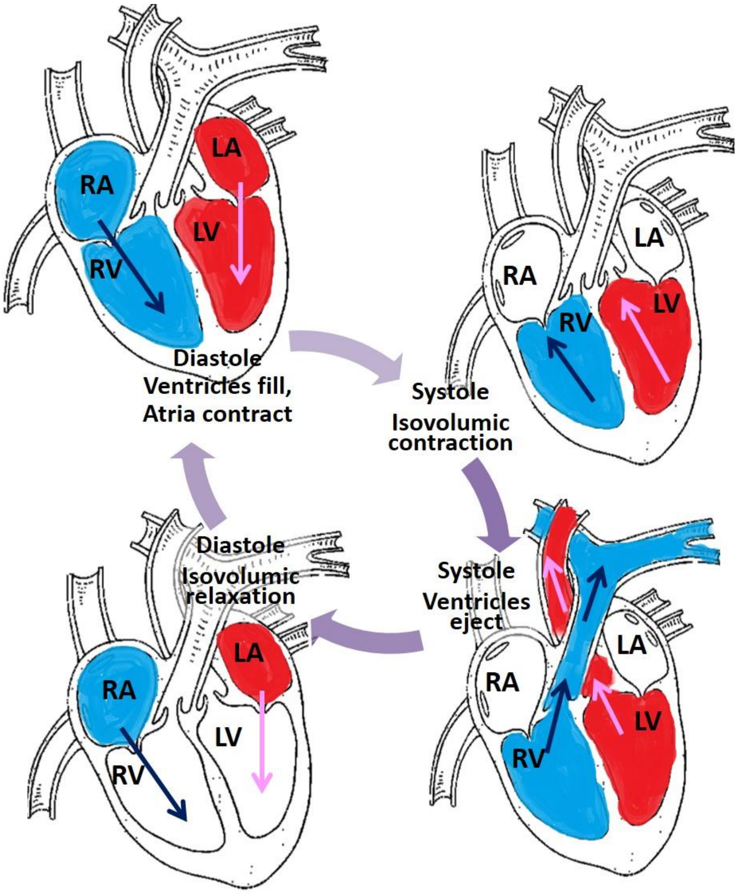

Figure 1.2. The cardiac cycle.

1.1.2 Cardiac Cells and Subcellular Organelles

Cardiomyocytes or contractile muscle cells are the main functional unit of myocardial contraction. Although there are many different components of the myocardium, including pacemaker and conducting fibres, blood vessels, fibroblasts and the extracellular matrix in the myocardium, cardiomyocytes occupy approximately 75% of the total volume of the myocardium (Weber and Brilla, 1991).

The myocytes make contact with neighbouring myocytes through intercalated discs which consist of gap junctions, fascia adherens junctions, and desmosomes. The gap junctions regulate the passage of ions and small molecules and allow electrical impulses to pass preferentially between cells; a functional impairment of the cardiac gap junction is one of the essential causes of arrhythmias (Imanaga, 2010). The fascia adherens junctions are where the actin filaments insert and anchor myocytes firmly by linking the myocyte membrane to the actin cytoskeleton (Sheikh et al., 2009). The desmosomes are also major cell adhesion junctions that anchor the myocyte membrane and consist of cadherins, plakoglobins and plakins (Sheikh et al., 2009).

Each myocyte is bounded by sarcolemma and is made up of bundles of contractile proteins (myofibrils), sarcoplasmic reticulum (SR), nucleus, and mitochondria. The sarcolemma forms T-tubules that penetrate into the intracellular space. T-tubules are specialized tube-like invaginations that facilitate the spread of the wave of electrical excitation within the cell (Brette and Orchard, 2003).

Myofibrils consist of the two chief contractile proteins: the thick myosin filaments and the thin actin filaments. The sarcomere is limited on either side by the Z-line. During contraction, the filaments slide over each other to move the Z-lines. During sliding, the filaments pull together the two ends of the sarcomere which is the fundamental contractile unit (Rayment et al., 1993). This repetitive interaction, involving the myosin heads binding and unbinding with actin, is called cross-bridge cycling.

The SR is a fine network of Ca^{2+} ion storage compartments that lie in very close opposition to the T-tubules (Scales, 1981). During systole, the SR releases Ca^{2+} ions into the cytosol *via* ryanodine receptors to trigger shortening of the sarcomeres. During diastole, the SR rapidly takes up Ca^{2+} ions from the cytosol to the interior via the Ca^{2+} pump which is located on the SR membrane. The nucleus (usually only one) is located near the centre of the cell and contains almost all the genetic information required to maintain and repair cell structure.

Mitochondria lie in between the myofibrils and occupy a large portion of the volume of the cell. Mitochondria play a primary role as the powerhouse of the cell, producing the ATP that is required for cell survival and function (Warda et al., 2013).

1.1.3 Cardic Ion Channels and Ion Transporting Proteins

Cardiac muscle is an excitable tissue. The electrical properties of cardiac muscle influence the mechanical pumping function of the heart as it circulates the blood. The entire ventricles are rapidly activated and create synchronized contraction through the electromechanical integration of cardiomyocytes. Therefore, understanding the cell membrane and its related signaling proteins is indispensable for examining cardiac function.

The cell membrane is composed of a lipid bilayer of phospholipid molecules (phosphatidylcholine and phosphatidylethanolamine). The nonpolar hydrophobic tail ends of the phospholipid molecules project toward the middle of the membrane, and the polar hydrophilic heads border on the water phase at each side of the membrane (Figure 1.3).
The thickness of the cell membrane is approximately 70 Å - 100 Å. Cholesterol molecules are present in high concentrations in the cell membrane. Large protein molecules are also inserted in the lipid bilayer matrix. Some proteins are inserted through the entire membrane (e.g., Na^+-K^+ ATPase and the various ion channel proteins), whereas other proteins are inserted into either the inner or outer layer only (e.g., neurotransmitter receptors and adenylate cyclase enzyme). The membrane has a fluidity which gives the protein and lipid molecules freedom to move around in the plane of the membrane (Singer and Nicolson, 1972).

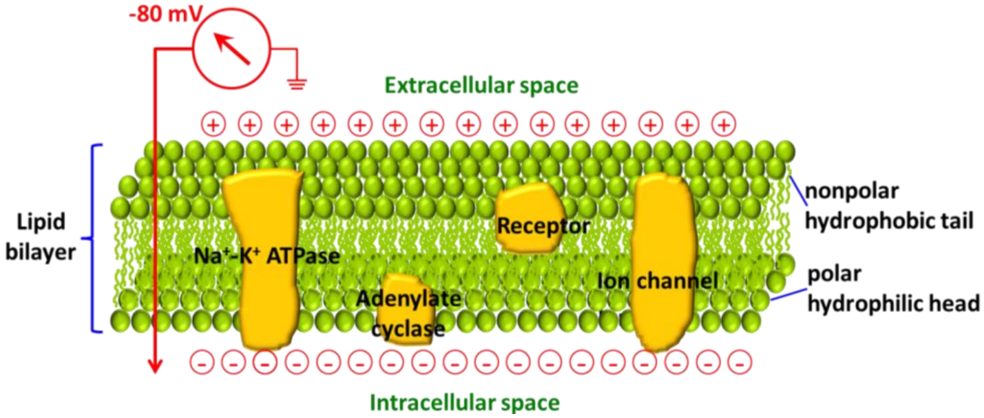

Figure 1.3. Schematic illustration of cell membrane structure consisting of a lipid bilayer and various proteins. For simplicity, the cholesterol and glycoprotein molecules are not shown.

In normal conditions, myocytes maintain an internal ion concentration markedly different from that in the extracellular space, which underlies the resting potential and excitability. The transmembrane resting potential of ventricular myocytes is about -80 mV (Figure 1.4). The extracellular space (interstitium) of the myocyte is high in Na^+ (~145 $mmol \cdot L^{-1}$) and Cl^- (~120 $mmol \cdot L^{-1}$), but low in K^+ (~4 $mmol \cdot L^{-1}$). The free Ca^{2+} concentration is about 2 $mmol \cdot L^{-1}$. In contrast, the intracellular fluid (cytosol) has a low concentration of Na^+ (< 15 $mmol \cdot L^{-1}$) and Cl^- (~6 $mmol \cdot L^{-1}$), but a high concentration of K^+ (~150 $mmol \cdot L^{-1}$). The free intracellular Ca^{2+} concentration is < 10^{-7} $mol \cdot L^{-1}$, but during contraction rises to 10^{-5} $mol \cdot L^{-1}$ or 10^{-4} $mol \cdot L^{-1}$. These electrophysiological properties of myocytes result from the activities of the proteins inserted into the cell membrane. The ion distributions and related pumps are depicted in Figure 1.4.

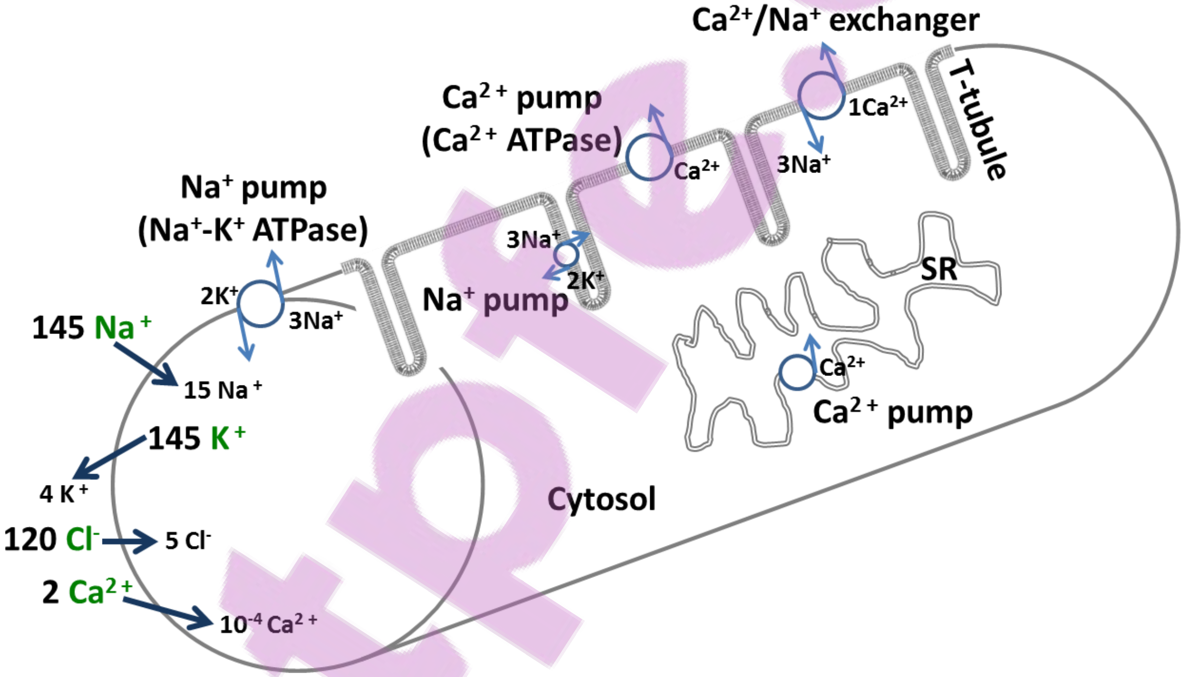

Figure 1.4. Schematic illustration of ion distributions across the cell membrane. This shows only intracellular and extracellular ion distribution and related pump proteins. The Na^+ pump is located in the sarcolemma and the T-tubule. The Ca^{2+} pump is located in the sarcolemma and SR membrane. The Ca^{2+}-Na^+ exchange carrier is located in the sarcolemma. Arrows indicate the direction of the net electrochemical gradient of each ion.

1.1.4 Excitation-Contraction Coupling

Excitation-contraction coupling (EC coupling, Figure 1.5) is the process that couples an action potential (excitation) with cross-bridge cycling and contraction (shortening and force development) of the heart. Increasing intracellular Ca^{2+} concentration is the key mediator of EC coupling (Bers, 2002).

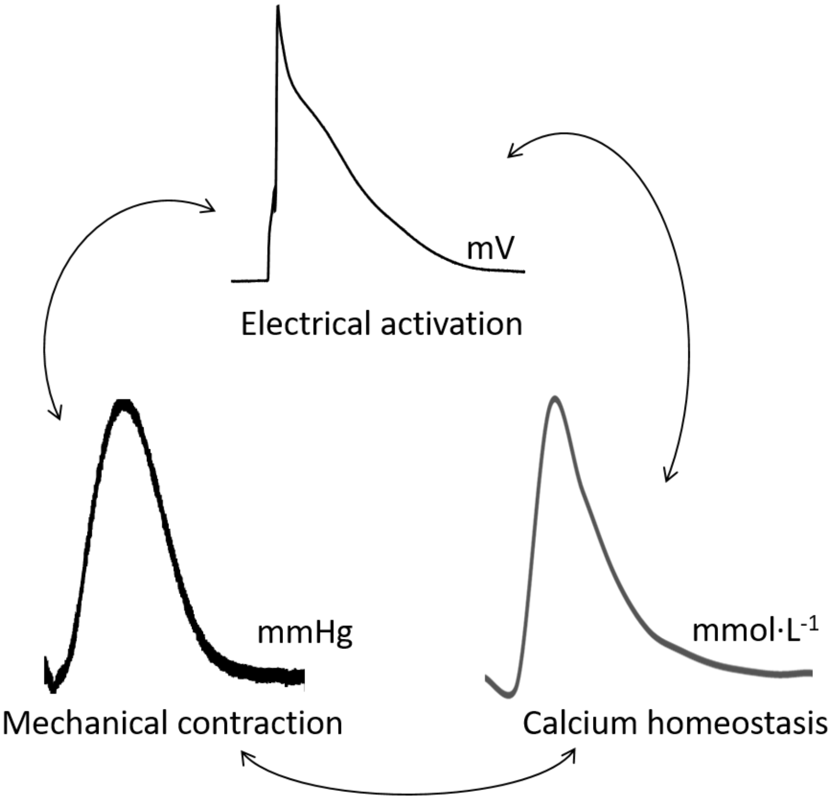

Figure 1.5. Schematic representation of the coupling electrical activation and mechanical contraction through Ca^{2+} homeostasis.

The action potential (AP) is initiated in the pacemaker (sinoatrial (SA) node) and propagates throughout the myocardium by electrical transmission through gap junctions. When the electrical impulse reaches the ventricular cells, EC coupling occurs within the narrow dyadic subspaces, regions of restricted space bounded by the T-tubular and SR membrane, to connect the depolarization of the sarcolemma/T-tubule to Ca^{2+} release from the SR which leads to myocardial contraction.

The depolarization of the membrane potential due to activation of Na^+ channels opens voltage-dependent K^+ channels (transient outward K^+ channels and delayed rectifier K^+ channels) and *L*-type Ca^{2+} channels (dihydropyridine receptors, DHPRs). These currents determine AP duration. Inward rectifier K^+ channels also activate late during the AP, which controls resting membrane potential.

Small but varying amounts of Ca^{2+} enter the cell through DHPRs and trigger large amounts of Ca^{2+} release from the junctional SR by opening Ca^{2+} release channels (ryanodine receptors, RYRs). This is referred to as 'Ca^{2+}-induced Ca^{2+} release' (CICR) (Piacentino et al., 2000). The resultant elementary Ca^{2+} release events from the RYRs can be visualized as Ca^{2+} sparks (Copello et al., 2007). When many Ca^{2+} sparks occur together synchronously, global Ca^{2+} transients are produced which increase intracellular Ca^{2+} concentrations. When free Ca^{2+} binds to the troponin complex, a conformational change takes place and the myosin-binding site on the actin filament is exposed. The interaction of actin and myosin is thus facilitated and contraction takes place.

After contraction, relaxation follows by removal of Ca^{2+} from the cytosol. A large amount of the activator Ca^{2+} is taken up into the SR by the SR Ca^{2+} pump (SERCA). The remaining Ca^{2+} is removed by Na^+-Ca^{2+} exchanger (NCX) and the sarcolemmal Ca^{2+} pump. Figure 1.6 shows the key pathways of Ca^{2+} transport in cardiomyocytes. Finally, intracellular Na^+ and K^+ homeostasis is maintained by the Na^+ pump and the resulting current leads to membrane repolarization and the resting membrane potential partly.

Therefore, EC coupling relies on well-controlled intracellular Ca^{2+} cycling. The SR plays a particularly important role in regularly repeating Ca^{2+} release and uptake, billions of times during the entire lifespan. In particular, the Ca^{2+} release unit, the hub of a huge macromolecular complex, formed by a DHPR and an RYR, is critical to the overall EC coupling process.

I briefly summarise the common features of major ion currents and Ca^{2+} handling proteins, myofibrillar proteins, and the differences of those between the LV and the RV.

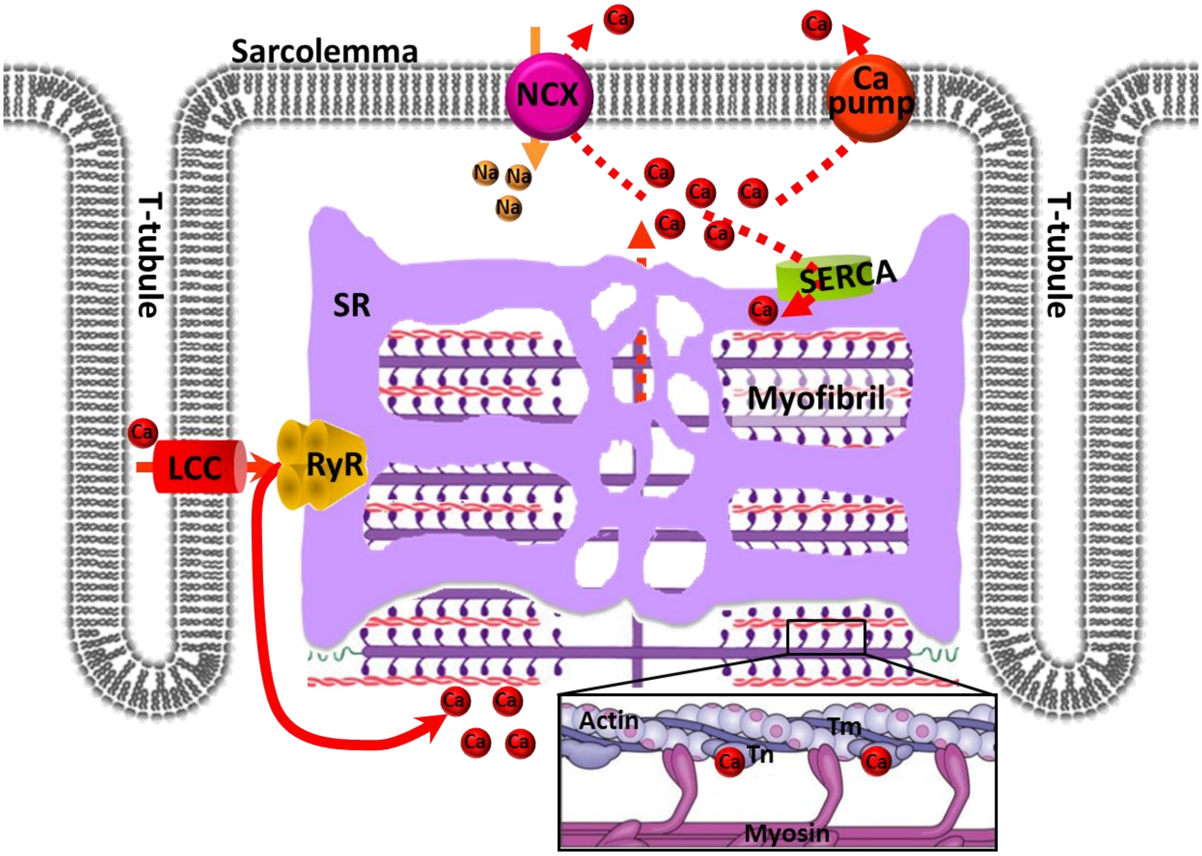

Figure 1.6. Schematic illustration of Ca^{2+} transport in EC coupling. CICR increases cytosolic Ca^{2} concentration sufficiently for contraction. As Ca^{2+} ions are taken back into the SR by SERCA, relaxation starts. Some of the Ca^{2+} that has entered during excitation is removed by NCX and the sarcolemmal Ca^{2+} pump. Tn: troponin, Tm: tropomyosin, Solid arrow: Ca^{2+} influx, Dotted arrow: Ca^{2+} return.

Na^+ channel

The upstroke of the AP of myocytes is due to a transient increase in membrane permeability to Na^+ ions. The Na^+ channel current (I_{Na}) is responsible for the very rapid rising rates in APs (Undrovinas et al., 2002). When the cell membrane is depolarized beyond -65 mV, this inward current is initiated to rise to a peak and then to decline within a few milliseconds. I_{Na} is regulated by time- and voltage-dependent activation and inactivation states. When the AP plateaus, most of the channels are inactivated. At diastolic potentials, the time course of removal of this Na^+ channel inactivation determines the availability of these channels for impulse conduction and consequently the refractory periods.

Martin et al. demonstrated that wild type myocytes possessed similar peak I_{Na} magnitudes in the RV and LV, these were decreased in both the RV and LV in a heterozygotic SCN5A$^+$/$^-$ mice model, but with a greater reduction in RV than LV (Martin et al., 2012).

Ca^{2+} channel

The Ca^{2+} channel current (I_{LCC}) is carried principally by Ca^{2+} ions which create an appreciable membrane current in the inward direction when the cell membrane is depolarized (Reuter, 1967). It underlies impulse conduction in sinoatrial and atrioventricular nodes and is crucial to the maintenance of the plateau phase of the APs of myocytes. It is enhanced by catecholamines and blocked by ions such as Mn^{2+}, La^{3+}, Co^{2+}, and Ni^{2+}. Its voltage dependence and the kinetics of these state parameters are distinct from I_{Na} so that I_{LCC} can be activated by potentials at which I_{Na} is almost completely inactivated. I_{LCC} accounts for the properties of Ca^{2+}-dependent upstrokes.

I_{LCC} has been reported not significantly different between RV and LV from mouse (Kondo et al., 2006) and canine heart (Molina et al., 2014), however, my previous study showed that the LV I_{LCC} density is larger than that of RV in rat heart (Kim et al., 2010).

Transient outward K^+ channel current (I_{to})

The very rapid repolarization of the AP is generated by a transition from inward to outward current. K^+ ions are the major charge carrier for this outward current, typically referred to as the transient outward K^+ channel current (I_{to} or I_{to1}). I_{to} consists of two components with distinct recovery kinetics: the fast ($I_{to,f}$) and slow ($I_{to,s}$) components (Niwa and Nerbonne, 2010). I_{to} contributes to the "notch" configuration of the AP. The time course of I_{to} is not entirely controlled by modulation of the I_{to} conductance by voltage-dependent states but this conductance is enhanced by the concentration of intracellular Ca^{2+} which changes in a phasic manner during depolarization of the AP.

Regarding different electrophysiological phenotypes between the LV and the RV, although there are disagreements among the various species and experimental settings, the results from studies of I_{to} is a notable exception. Most studies report that I_{to} is consistently larger in RV than LV (Di Diego et al., 1996; Kondo et al., 2006; Martin et al., 2012).

Delayed rectifier K^+ channel current (I_{Kv})

The delayed rectifier K^+ channel current (I_{Kv}) makes major contributions to repolarization of the AP (Schram et al., 2002). This current activates slowly (compared to I_{to}) in response to the voltage changes initiated by depolarization. I_{Kv} consists of rapid and slow delayed rectifier K^+ channels current (I_{Kr} and I_{Ks}, respectively). Sometime I_{Kv} is the same as I_{Kr} used by some authors. Note that I_{Ks} is not considered here because this channel has very low expression levels in rat myocytes.

I_{Ks} density but not I_{Kr} was significantly larger in RV than LV M cells in canine (Volders et al., 1999), however, I_{Kr} genes (Kv1.4, Kv1.5, Kv2.1, Kv4.2 and Kv4.3) were decreased in the LV compared to the RV in rat (Huang et al., 2001).

Inward rectifier K^+ channel current (I_{K1})

The inward rectifier K^+ channel current (I_{K1}) stabilizes the resting membrane potential of the cardiomyocyte near the negative K^+ equilibrium potential (Lopatin and Nichols, 2001). "Inwardly-rectifying" means that the current passes more easily in the inward direction (into the cell) than in the outward direction (out of the cell). Its conductance increases under hyperpolarization (K^+ entry) and decreases under depolarization (K^+ exit).

There are not significantly different in I_{K1} between the LV and the RV from dog (Volders et al., 1999) and mouse (Kondo et al., 2006), however, in the guinea pig heart, the levels of mRNA encoding Kir2.1 and Kir2.3 channel proteins are significantly greater in the LV than in the RV (Warren et al., 2003).

Na^+ pump (Na^+-K^+ ATPase)

The major ion pump in myocytes is the Na^+ pump. It provides the only significant Na^+ efflux mechanism from the cytosol and is therefore vital for maintaining normal electrical activity and the transmembrane Na^+ gradient (Kaplan, 2002). It pumps Na^+ out from the cytosol while simultaneously pumping K^+ into the cytosol, against their respective electrochemical gradients, via the process of ATP hydrolysis. The coupling of Na^+ and K^+ pumping is obligatory, and a 3:2 coupled ratio of Na^+ pumped out to two K^+ pumped in is most common. Therefore, the pump is electrogenic and directly produces a small potential difference causing the membrane potential to be negative. Under normal steady-state conditions, the contribution of the Na^+ pump to the membrane potential in myocytes is only a few millivolts.

Ca^{2+} pump (Ca^{2+} ATPase)

Because the electrochemical gradient of Ca^{2+} ion across the cell membrane is large, there must be a mechanism for removing Ca^{2+} from the cytosol. It has been reported that there are Ca^{2+}-ATPases in the sarcolemma and the SR membrane. Sarcolemmal Ca^{2+}-ATPase actively transports Ca^{2+} outward against its electrochemical gradient, utilizing ATP in the process. In particular, the SR Ca^{2+}-ATPase, known as *SERCA*, actively pumps Ca^{2+} from the cytosol into the SR lumen. This sequestration of Ca^{2+} by SERCA is essential for muscle relaxation during cardiac diastole and protein levels of SERCA determine the systolic contractile reserve (Hasenfuss et al., 1994b).

It has been reported that there are similar levels of SERCA units in RV and LV in mouse (Kondo et al., 2006) and rat (Sathish et al., 2006), however, another study in rat showed different SR Ca^{2+} uptake activity between the LV and the RV (Afzal and Dhalla, 1992).

Na^+-Ca^{2+} exchanger (NCX)

The resting Ca^{2+} influx and the extra Ca^{2+} influx that occurs during the AP must be returned to the interstitial fluid. The Na^+-Ca^{2+} exchanger (NCX) exchanges one internal Ca^{2+} ion for 3 external Na^+ ions via a membrane carrier, which is facilitated by ATP (not by ATP hydrolysis) (Ottolia et al., 2013). NCX utilizes the Na^+ electrochemical gradient for the pumping of Ca^{2+} against its large electrochemical gradient. Therefore, the energy required for this Ca^{2+} transport is derived from the Na^+ pump. Thus the Na^+ pump indirectly helps to maintain the Ca^{2+} electrochemical gradient across the cell membrane. During the cardiac cycle, the energetics would be adequate for an exchange ratio of 3 Na^+: 1 Ca^{2+} (Blaustein and Lederer, 1999). This exchange reaction depends on the relative concentrations of Ca^{2+} and Na^+ between interstitium and cytosol and on the relative affinities of the binding sites for Ca^{2+} and Na^+. In addition, if the intracellular concentration of Na^+ ion increases, these exchange carriers would exchange the ions in reverse and lead to increased Ca^{2+} influx.

NCX mRNA expression was significantly lower in the RV than in the LV in rat (Correia Pinto et al., 2006), however, no differences in NCX mRNA expression between the LV and the RV were identified in mouse (Kondo et al., 2006).

Myofibrillar protein

Troponin complex consists of Troponin I, T, and C subunits. Troponin C (TnC) has the regulatory Ca^{2+} binding site. Troponin I (TnI) inhibits actin-myosin interaction. Troponin T (TnT) binds to TnC, TnI, and tropomyosin. When Ca^{2+} binds to TnC, conformational change of TnI takes place and the myosin-binding site on the actin is exposed, which initiates contraction.

Tropomyosin (Tm) is a two-stranded α-helical coil situated in the actin groove. When Tm is shifted out of the actin groove, actin can bind to myosin, which allows tension to develop. Myosin has an ATP binding site. Hydrolysis of an ATP molecule causes conformational change in the myosin head, which moves the location of the myosin head along the actin filament. The myosin head then binds to an exposed myosin-binding site on the actin. As the myosin head releases the products of ATP hydrolysis (ADP and an inorganic phosphate), it undergoes a conformational change to ATP-non-bound state. As myosin expends the energy, this movement is called the 'power stroke'. Many of these power strokes result in 'pulling in' of the actin filaments closer together, thereby shortening the length of the sarcomere. These length changes of the myofibrils manifest as cardiac contraction. After the removal of bound Ca^{2+} from TnC, Tm blocks the actin binding sites, crossbridges detach, and finally cardiac relaxation take places.

Different Ca^{2+} sensitivity of LV versus RV myofilaments in the rat has been reported (Perreault et al., 1990). This difference has been attributed to a larger proportion of the V_1 (heavy chain α) isozyme of myosin in the RVs versus the LVs of rats (Brooks et al., 1987), since the higher content of the V_1 isozyme can hydrolyze ATP at a higher rate and thereby supports a faster rate of cross-bridge cycling than the V_2 or V_3 (heavy chain β) isozymes. This appears to correlate with the more rapid velocity of shortening of RV versus LV muscles in the rat (Perreault et al., 1990).

1.2 Left and Right Heart

1.2.1 Coordination and Difference

The LV and the RV differ structurally and functionally, and clinical aspects of disease progression have likewise been shown to be quite different as discussed below.

The heart, weighing 300 g, holds approximately 500 mL of blood (LV: 150 mL, RV: 160 mL - 170 mL, and each atrium: 100 mL at diastole). The right and left sides of the heart should operate in parallel to eject the same amount of blood with each beat. The right heart receives venous blood from the body and pumps it to the lungs, whereas the left heart receives blood from the lungs and pumps it to the systemic circulation. The two ventricles pump the blood away from the heart against corresponding pressures. The lungs are a low-resistance system (normal peak systolic pressure ~30 mmHg), whereas the systemic circulation is a higher resistance system (normal peak systolic pressure ~120 mmHg). Consequently the RV has a thinner wall and is more compliant than the LV (Trafford et al., 2001). RV pressure is not only lower than LV pressure and but also shows an earlier systolic peak and more rapid pressure decline than LV pressure (Dell'Italia and Walsh, 1988a).

Some of the hemodynamic properties of the LV and RV in human are summarized in Table 1.1 (derived from Haddad et al. (2008)).

Table 1.1. Comparison of LV and RV hemodynamic properties

Characteristics	**LV**	**RV**
End-diastolic volume, mL	136 ± 30	157 ± 35
Mass, g	98 ± 46	35 ± 18
Wall thickness, mm	7 - 11	2 - 5
Ventricular pressure, kPa	17.33/1.07 [(12 - 18.67)/(0.67 - 1.6)]	3.3/0.53 [(2 - 4)/(0.13 - 0.93)]

Ventricular elastance, kPa·L^{-1}	566.62 - 894.6	82.66 - 382.63
SVR versus PVR, kPa·s·L^{-1}	11 (7 - 16)	0.7 (0.2 - 1.3)
Stroke work index, g·m^{-2} per beat	50 ± 20	8 ± 2

SVR, systemic vascular resistance; PVR, pulmonary vascular resistance.

The shape of the LV approximates to a cone and the septal component of the LV wall is curved, convexing into the RV cavity (Ho, 2009). The LV wall has a typical arrangement of myocardial strands that change orientation from being oblique in the subepicardium to circumferential in the middle and longitudinal in the subendocardium, which permits torsion, shortening and thickening of LV contraction simultaneously.

In contrast, the chamber of the RV is triangular and the RV wall consists of a superficial layer arranged circumferentially and parallel to the atrioventricular groove and a deep layer arranged longitudinally (Ho and Nihoyannopoulos, 2006). This structure allows the predominately longitudinal shortening of RV contraction than short-axis (circumferential) shortening.

As the RV wall is thinner, a volume of RV myocardium occupies a greater surface area than the same volume of LV myocardium. This higher surface-to volume ratio of the RV requires a smaller inward motion to eject the same stroke volume as the LV but supports a lower pressure. This accords with a study that the RV myocardium maintains a much lower energy than LV myocardium, commensurate with its lower energy requirements (Itoya et al., 1996). In addition, difference geometries of the LV and the RV would contribute to difference in energy usage; LV kinetic energy was higher in early diastole compared with the RV, while kinetic energy of the RV is greater during systole compared with early diastole (Carlsson et al., 2012).

The differences in the contractile performance between the LV and the RV myocytes in normal heart as well as diseased heart have been examined.

Belin et al. showed that even Ca^{2+}-saturated maximal force between the LV and the RV myocytes from normal heart was not different, myofilament dysfunction was greater in the LV than in the RV in congestive heart failure (Belin et al., 2011) . In contrast, McMahon et al. showed that baseline RV myocyte contractile function was shown to increased compared to LV myocytes in the control group and RV myocyte contractile function remained higher than that for LV myocytes in dilated cardiomyopathy (McMahon et al., 1996). Janssen et al. also showed that in end-stage failing spontaneously hypertensive heart failure (SHHF) rats, RV function was only marginally affected, whereas a severe contractile dysfunction of LV myocardium was present although there was no difference between the LV and the RV contractile function (Janssen et al., 2003).

Significant differences in myocyte size between the LV and the RV are present in rat hearts (Anversa et al., 1986; Gerdes et al., 1986; Olivetti et al., 1987): RV myocytes had significantly smaller volumes and cross-sectional areas compared to LV myocytes. In addition, the mechanical overload of the LV produced concentric and eccentric hypertrophy of the LV, while that of the RV produced only concentric hypertrophy of the RV (Anversa et al., 1986). Myocyte nuclear hyperplasia and cellular hypertrophy both participated to the adaptive response of the RV myocardium in long-standing pressure overload cardiac hypertrophy, while no changes in weight, myocyte size, and nuclear number were observed in the LV myocardium (Olivetti et al., 1987).

Clinical approaches to improving cardiac performance can be equally applicable to the LV and the RV in various forms of heart disease and are based on a general understanding of the laws that define cardiac mechanics. However, in practice, appropriate therapy for LV dysfunction has been shown to be not necessarily ideal for RV dysfunction in review (Walker and Buttrick, 2009).

To date, little attention has been paid to the differences in physiology and biology between the LV and the RV.

1.2.2 Stress Development

The force created by the muscle fibres in ventricular walls during their contraction generates the ventricular pressures needed to drive flow in the systemic and pulmonary circulations (Hefner et al., 1962). Stress is defined as the force divided by the cross-sectional area over which the force acts. The normal ventricles function within a narrow range of both end-diastolic and peak systolic stress values (Hood et al., 1968). In addition, maximum stresses occur at the endocardial surface and decrease to a minimum at the epicardial surface during cardiac contraction, which indicates the importance and dependence of stress not only on the pressure but on the changing geometry of the left ventricle particularly during systole. (Mirsky, 1969).

Myocardial wall stress (or wall tension) increases as the myofilaments undergo cross-bridge cycling during cardiac contraction, so that is used as a measure of myocardial function. Myocardial wall stress is known to be one of the primary determinants of myocardial oxygen consumption (Sarnoff et al., 1958; Strauer et al., 1977). Normalization of wall stress in heart disease with volume/pressure loading has been thought to be the feedback mechanism governing the rate and extent of development of ventricular hypertrophy (Alter et al., 2012; Grossman et al., 1975; Hood et al., 1968).

Therefore, understanding ventricular wall stress can provide important insights into the underlying ventricular mechanics and energetics in compromised hearts. Different stresses acting in the ventricular walls may lead to different contractile properties in the LV and RV in a normal heart. Quantification of ventricular wall stress is necessary for an understanding of both normal and pathological ventricular mechanics.

Modulation by heart rate of force (or stress) generation is one of fundamental aspects of cardiac mechanics. Increasing cardiac frequency by pacing in human has been reported to increase cardiac contractility, known as positive force-frequency relation (Bhargava et al., 1998; Buckley et al., 1972; Hasenfuss et al., 1994a). Also, in other many species, there is a positive force-frequency relation of the heart (Buckley et al., 1972; Ezzaher et al., 1992; Freeman et al., 1987; Palakodeti et al., 1997). The responses of cardiac contractility to increases in the frequency either by adrenergic stimulation or in heart diseases are very important for maintain heart pumping to meet tissue demands. Therefore, comparing stress-frequency relationship (SFR) with/without adrenergic stimulation between the LV and the RV should be examined for understanding of different properties of stress between the LV and the RV.

Although there are no reliable ways to directly measure wall stress in the intact ventricle, one of the best approaches to obtaining a realistic quantitative assessment is to measure quasi-isometric contraction using isolated cardiac muscles (trabeculae carneae and papillary muscles).

1.3 Virtual Cardiac Cell

The basis of cardiac function is EC coupling at the cellular level. Several nonlinear components connecting electrical excitation to Ca^{2+} signals to trigger cell contraction at the cell membrane involve the EC coupling process. The complexity of EC coupling requires the use of mathematical modeling to facilitate understanding. Many mathematical models for EC coupling have been developed at the cellular level for different species and for different regions of the mammalian heart.

1.3.1 History of Cardiac Cell Models

Noble (1962) published the earliest mathematical cardiac cell model for the Purkinje cell. He enhanced the Hodgkin–Huxley model for the AP in the nerve axon. The model included a second type of potassium channel but no calcium currents. After that, several EC coupling models included membrane-bound ion channels, transporters, and intracellular concentration changes for different cardiac tissues and different species.

The first model for the ventricular myocyte was developed by Beeler and Reuter (1977) . The model followed the earlier Purkinje models of McAllister et al. (1975) and added a slow inward current and the changes in intracellular Ca^{2+}. Then Luo and Rudy (1991) developed a biophysically-detailed model of the guinea-pig ventricular myocyte. Jafri et al. (1998) developed a ventricular myocyte model in the guinea pig to provide a detailed description of Ca^{2+} dynamics during EC coupling. This model built upon the Luo–Rudy model, but reformulated the Ca^{2+} dynamics, and has been the foundation of other species models including mouse, rat, dog, and rabbit (Bondarenko et al., 2004; Pandit et al., 2001; Shannon et al., 2004; Winslow et al., 1999).

1.3.2 Properties of Rat Cardiac Cell

The time course of the AP influences the whole-cell intracellular Ca^{2+} transient, which is critical for initiating and coordinating myocyte contraction. Ventricular AP profiles have been found to vary widely between species as well as within discrete regions of the ventricle of the same species (Li et al., 1998; Linz and Meyer, 2000). The APs of rats or mice show spike-like morphologies with a brief late plateau at potentials negative to -20 mV and are significantly shorter (Kaprielian et al., 2002) than those of other species (Li et al., 1998; Linz and Meyer, 2000; Stankovicova et al., 2000). Figure 1.7 shows a representative AP in the rat heart.

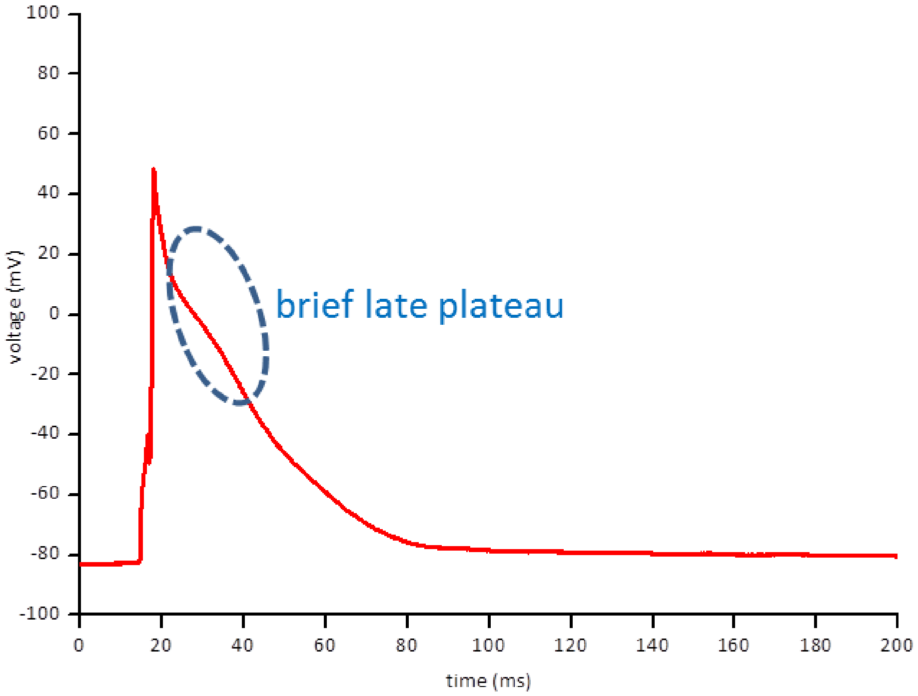

Figure 1.7. A representative AP of the rat ventricular myocyte obtained using patch-clamp recording (unpublished data). Note that the small notch on the AP upstroke is associated with the stimulus current (a large stimulus in fact eliminates this notch).

Variations in the types, kinetics and amplitudes of both inward (depolarizing, e.g., I_{LCC} and I_{Na}) and outward (repolarizing, e.g., I_{to} and I_{Kv}) currents have been suggested to underlie these interspecies differences in AP profiles (Nerbonne et al., 2001; Oudit et al., 2001; Richard et al., 1998). Moreover, there are different expression levels, kinetics and activity in Ca^{2+} handling related proteins in the rat compared to other species (Bers, 2002).

While only a few studies have been published, biophysical models for the rat ventricular myocyte are available (Korhonen et al., 2009; Krishna et al., 2012; Pandit et al., 2001; Pandit et al., 2003; Youm et al., 2011).

1.4 Relationship between Experiments and the Computational Model

The paradigm for studying cardiovascular disease has now shifted to clarifying related biochemical mechanisms rather than studying hemodynamic dysfunction. The existing therapeutic strategy for managing cardiovascular disease is to block the signaling pathways most strongly activated in disease, and most drug targets are membrane-bound proteins for cell signaling. On the other hand, since cell signaling integrates the behaviour of many biological components, knowledge of individual system components is not sufficient in itself to yield mechanistic insights. Validated computational models can be dissected in time, physical space or parameter space, allowing the cellular and subcellular processes underlying normal and abnormal tissue and organ function to be probed at a level of detail impossible to achieve experimentally (Clayton, 2001).

Therefore, a computational model is needed to investigate the physiological and pathophysiological mechanisms of normal and abnormal cardiac function in tandem with experimental studies.

1.5 Thesis Objectives

The objectives of the work described in this thesis are as follows.

- **To perform quasi-isometric contraction experiments to compare different stresses in LV and RV muscles.**

Using instrumentation based on a mechanical testing device, quasi-isometric contraction experiments were performed on cardiac trabeculae. Through the application of electrical field stimulation (at various frequencies) and specific drugs related to cardiac function (e.g. adrenergic agonists) the contraction properties of individual trabeculae were elucidated.

- **To perform Ca^{2+} imaging experiments for comparing different Ca^{2+} modulation between LV and RV myocytes.**

The cellular electrophysiological properties of isolated ventricular myocytes were obtained through confocal microscopic experiments. Ca^{2+} transients were recorded.

- **To implement a mathematical model which couples together multiscale results from experiments, and aids in drawing conclusions.**

Using the CellML encoding standard and OpenCOR, the components of three separate models of cardiomyocyte function (electrophysiology, calcium dynamics and mechanics) were disassembled as each module and validated separately, and then necessary parts were combined into a new integrative model of rat ventricular myocyte. The model was parameterised by applying data provided from experimental results.

Chapter 2

Methods

2.1 Experimental Animals

This investigation conformed to the requirements of the Animal Ethics Committee of the University of Auckland (Approval R595 and R787) and the National Animal Ethics Advisory Committee (The Animal Welfare Act 1999, Schedules 1 to 7). Male Wistar rats (280 g - 380 g, 7 weeks - 8 weeks old) were anesthetised with isoflurane mixed in 100% O_2. After cervical dislocation, the heart was quickly excised following thoracotomy and placed in cold saline solution. The aorta was immediately cannulated and perfused with an oxygenated solution of either low-calcium Tyrode's solution containing 2,3-butanedione monoxime (BDM) or normal Tyrode's solution, for trabecular preparation or single cell preparation, respectively.

2.2 Solutions and Chemicals

All solutions were made using distilled water and anhydrous dimethyl sulphoxide (DMSO) which is for stock solution and analytical grade chemicals.

During the perfusion of the isolated heart and superfusion of trabeculae, a modified Tyrode's solution was used as the standard solution, (in mmol·L^{-1}): 140 NaCl, 5.4 KCl, 1 $MgCl_2$, 0.33 NaH_2PO_4, 1.5 $CaCl_2$, 10 4-(2-hydroxyethyl)-1-piperazineethanesulfonic acid (HEPES), 10 glucose (pH 7.4, adjusted with NaOH).

During the dissection of trabeculae, low-Ca^{2+} Tyrode's solution containing BDM was used, (in mmol·L^{-1}): 140 NaCl, 5.4 KCl, 1 $MgCl_2$, 0.33 NaH_2PO_4, 0.3 $CaCl_2$, 10 HEPES, 10 glucose (pH 7.4) and 20 BDM as a cardioplegic agent for minimizing cutting damage (Mulieri et al., 1989).

During isolation of single myocytes, Ca^{2+}-free Tyrode's solution and modified Kraft-Brühe (KB) solutions were used, (in mmol·L^{-1}): 70 KOH, 50 L-glutamic acid, 30 KCl, 20 taurine, 3 $MgCl_2$, 0.5 EGTA, 10 HEPES and 20 glucose (pH 7.3, adjusted with KOH).

All of the perfusion solutions and superfusates were continuously saturated with 100 % O_2. The Fluo-4 AM loading solution for myocytes consisted of 10 mL KB with 5 µmol·L^{-1} Fluo-4 AM (Invitrogen, Carlsbad, CA) previously dissolved in DMSO, and 5% w/v pluronic F-127 (Texas Fluorescent Laboratories, USA).

Chemical reagents were obtained from Sigma-Aldrich (Carlsbad, CA), unless otherwise stated.

2.3 Trabecular Contraction Experiments

2.3.1 Mechanical testing device

Mechanical experiments were conducted using a mechanical testing device that forms part of a microcalorimeter (Figure 2.1), which was constructed previously by Dr A. Taberner (2009). The device comprises an open-ended measurement chamber, two externally-mounted arrays of non-contact thermopile sensors (not used in these experiments) and an open-topped muscle-mounting chamber. The measurement chamber consists of a glass tube 7 mm in length and 1 mm in width with open ends glued to a gold-plated brass housing. Tubular quartz arms (700 µm OD and 500 µm ID) are inserted into both ends of the glass tube. The open-ended design allows continuous flow of the experimental solution through the glass tube. The upstream quartz arm is attached to a high-speed piezoelectric actuator (Queenagate Instruments, Torquay, Devon, UK) and a low-speed DC actuator (M-227.25 DC-Mike, Physik Instrumente, Karlsruhe, Germany). The downstream quartz arm is attached to a silicon-beam force transducer (KX801 Micro Force Sensor, Kronex Technologies, Oakland, CA).

A trabecula is extended between double-J-shaped platinum hooks attached to the two tubular quartz arms. Field stimulation of the trabecula is achieved by platinum stimulation electrodes. The voltage signals from the force transducer are acquired via LabVIEW2009 software and all the experimental variables including stimulus frequency and voltage are recorded using LabVIEW SignalExpress 2009 (National Instruments, Austin, TX).

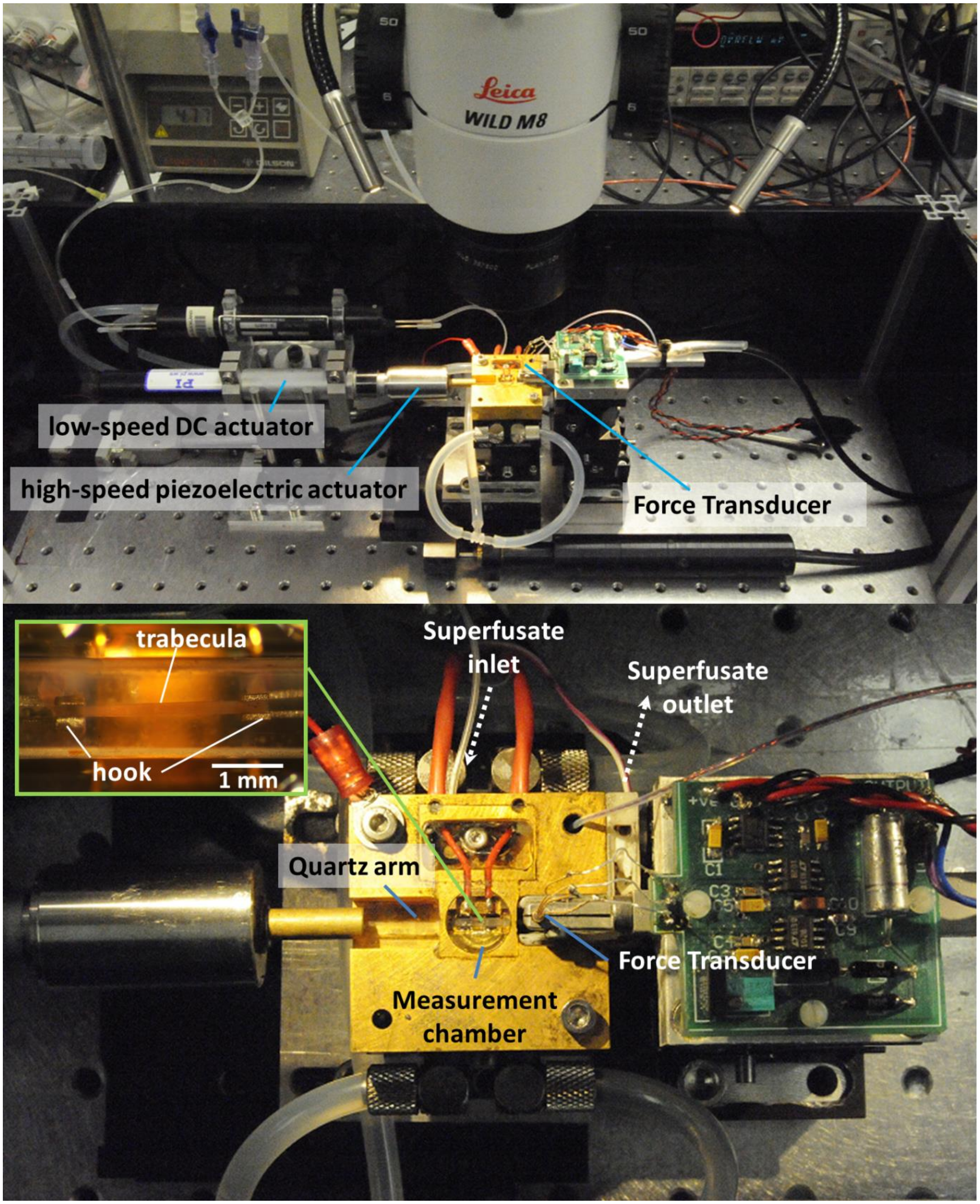

Figure 2.1. Photographs of mechanical testing device. Upper panel shows the overall layout of the device. Lower panel is a close-up view of the chambers of the device; the inset is a top view of a trabecula between two hooks.

2.3.2 Tissue Preparation

LV and RV trabeculae were used to examine cardiac quasi-isometric contraction for assessing cardiac stress. Using an isolated muscle preparation can create a problem with insufficient oxygen supply to the centre of the muscle strips. To avoid this problem, the trabeculae used in this study were approximately cylindrical in shape, with a maximum diameter less than 0.2 mm, which assured uncompromised oxygen delivery to the core of the trabeculae during any of the experimental protocols (Han et al., 2011). This is in agreement with previous studies. For example, Barclay et al. (2005) showed that rat cardiac muscle of ~0.8 mm radius could survive 1 Hz stimulation at 37°C with no anoxic core when supplied oxygen maximally, and that muscles of a radius less than 0.3 mm were not compromised during stimulation at frequencies of up to 8 Hz.

Both LV and RV were carefully opened and thin, unbranched and geometrically uniform trabeculae were carefully dissected in oxygenated low Ca^{2+} Tyrode's solution with BDM to prevent possible dissection damage to the muscles. A small block of tissue at one end from the ventricular free wall and a second block of tissue (valve or free wall depending on the position) attached to the trabecula at the other were dissected out with the trabecula to facilitate mounting. Trabeculae were transferred and mounted between platinum-iridium basket-like hooks from a force transducer and a micromanipulator was used to minimize damage to the muscle, as previously described (Han et al., 2009).

Initially, the trabeculae were superfused with Tyrode's solution (without BDM), after which the calcium concentration of the solution was increased to 1.5 $mmol \cdot L^{-1}$. The chamber was 7 μL in volume and was superfused at a rate of ~0.6 $mL \cdot min^{-1}$, which allowed the entire bath to be refreshed with oxygen continuously during the experiment. The muscle was first kept completely slack while being stimulated at 5 Hz, and allowed to stabilize under these conditions for at least 1 hour before the experimental protocol was initiated. The trabeculae were then gradually stretched to their optimal length (defined by the length at which a small lengthening led to approximately equal increases in both resting tension and active developed tension). This length indicates the maximally attained length *in vivo*, and corresponds to ~2.2 µm sarcomere length (Rodriguez et al., 1992). All experiments were performed at 37.5°C.

2.3.3 Experimental Protocol

Experiments to determine the stress-frequency relationship were performed by measuring active stress production while the stimulus frequency was varied (1, 3, 7, 9, 10, 12 Hz). The order of these 'test' frequencies followed a Latin Square experimental design which allowed examination of the effect of time on contractile behaviour. Specifically, trabecula 1 was presented, in random order, a Latin Square frequency order of 10, 12, 9, 1, 3 and 7 Hz (see Figure 3.1), and each trabecula experienced a unique set of order. The 'reference' stimulus frequency between each test frequency was 5 Hz and twitch force was quantified at the point in time at which a steady-state was reached, prior to changing stimulus frequency.

To test the adrenergic response, cumulative concentration curves were first obtained with a β-adrenergic receptor (β-AR) selective agonist, isoproterenol (ISO, 3×10^{-10} mol·L^{-1} to 3×10^{-7} mol·L^{-1} in semi-log steps) at a baseline frequency of 5 Hz. Its half-maximal concentration (20 nmol·L^{-1}) and 10 times that concentration (200 nmol·L^{-1}) were used in further experiments. In the case of the nonselective agonist, norepinephrine (NE), only a concentration of 20 nmol·L^{-1} was used. The muscle was stimulated at 5 Hz and 7 Hz, encompassing the *in vivo* range of ~4.5 Hz - 8.5 Hz for the rat (Layland and Kentish, 1999; Vornanen, 1992), and also stimulated at 10 Hz to explore its response at a supraphysiological rate.

2.3.4 Analyses

In all experiments, developed force and diastolic force were determined and normalized to the muscle cross-sectional area, which was estimated by imaging muscle diameter at optimal length in a single plane and assuming a circular cross-section. Forces were converted to stress (kPa) by dividing by muscle cross-sectional area. Diastolic stress at 5 Hz was defined as the 0 kPa baseline diastolic stress. Data were collected and analyzed using custom-written software

(LabVIEW, National Instruments, Austin, TX) and Microsoft Excel (Microsoft, Redmond, WA). To assay contractile properties, the time to peak force (TPF), time from peak force to 50% relaxation (RT_{50}) and twitch duration (TD, TPF + RT_{50}) were determined. Student's *t* test or ANOVA were used to determine significant differences at $P < 0.05$. Data are presented as mean ± S.E.M.

2.4 Ca^{2+} Transient Experiments

2.4.1 Confocal Microscopy

The differences between LV and RV myocytes and the effect of ISO in cardiac Ca^{2+} ion flux were assessed using the ion-specific probe Fluo-4 AM (Invitrogen, Eugene, OR, USA). Isolated single myocytes were incubated with 5 $\mu mol \cdot L^{-1}$ Fluo-4 AM at room temperature for 15 minutes, then the stained myocytes were washed out twice with KB solution to allow for de-estrification which took 30 minutes. Stained myocytes were placed on a perfusion chamber of the confocal microscope (LSM 700, Carl Zeiss, Oberkochen, Germany) and were excited by 488 nm light from an argon-ion laser and emission signals over 505 nm were collected at room temperature. Image acquisition was performed in line scan mode using ZEN 2009 software (Carl Zeiss, Oberkochen, Germany). Fluorescence intensity was measured while applying field stimulation on the cells. Regions of interest on the myocytes were selected by plotting a line longitudinal to cell length to monitor changes in fluorescence intensity over time, and background fluorescence was identified in an area without cells.

2.4.2 Single Cell Preparation

Myocytes from LV and RV were dissociated using an enzymatic method as reported previously (Kim et al., 2010). Briefly, after rats were anesthetized, the hearts were removed and immediately cannulated and perfused via the aorta in a Langendorff apparatus with modified Tyrode's solution and then with nominally Ca^{2+}-free Tyrode's solution at 37°C. Thereafter, the hearts were treated with nominally Ca^{2+}-free Tyrode's solution containing 0.5 $g{\cdot}L^{-1}$ collagenase (Yakult Co., Tokyo, Japan) for 15 minutes - 20 minutes and were perfused with KB solution at 37°C. The LV and RV tissues were dissected from the digested heart and placed into separate dishes. Individual myocytes were released from the separated tissue pieces by mechanical agitation, and stored at 4°C in KB solution. Only rod-shaped, quiescent, Ca^{2+}-tolerant myocytes were selected for experiments.

2.4.3 Experimental Protocol

Calcium transients were elicited by field stimulation with cell stimulator (IonOptix, Inc., USA). Cells were first stimulated at 2 Hz for 2 minutes to reach a steady-state before recording. Elicited Ca^{2+} transients will be recorded at 1 Hz. Fluorescence was measured using a 512 pixel line. Scanning occurred with a temporal resolution of 1.53 lines per millisecond.

To further compare the contractile function between LV and RV myocytes on the basis of calcium transients, the cells were treated with ISO. During recording, cells were treated with modified Tyrode's solution for 2 minutes, and then ISO for 5 minutes.

2.4.4 Analyses

Fluorescence levels were normalized by analysing the ratio (F1/F0) of the peak values (F1) to the baseline value (F0), after subtracting autofluorescence in the absence of fluorescent dye (Kim et al., 2012). Calcium decay was obtained and analysed using Origin (v 6.0, Microcal Software, Studio City, CA) by fitting to the ratio using a double exponential equation. All data are presented as mean ± S.E.M. Student's t-test (paired or unpaired) was used to test for overall differences among myocytes and $P < 0.05$ was considered significant.

2.5 Mathematical Modelling

In order to quantitatively investigate the contribution of cardiac LCC as well as the Ca^{2+} handling mechanism to developing APs in LV and RV myocytes, I developed a new biophysical whole cell model of the rat ventricular myocytes. Then I linked this model to an existing Auckland model of force production to see whether the integrated model of force production revealed any difference between the ventricles. This process was to provide a useful comparison to experimental results in Chapter 3.

My combined model thus retains the fundamental features of rat ventricular myocyte electrophysiology originally described by Pandit et al. (2001), while including more detailed representations of CICR and other key aspects of Ca^{2+} regulation originally described by Hinch et al. (2004). In terms of rat electrophysiology, the model formulation is based on the Na^+ channel, the Ca^{2+}-independent K^+ channel, the steady-state K^+ channel, the inward rectifier K^+ channel, the hyperpolarizing-activated channel, the background K^+ channel, the background Na^+ channel, and the Na^+-K^+ pump described by Pandit et al. (2001). Whereas their model has a limitation of the calcium handling in the sarcoplasmic reticulum, the elaborate model of rat cardiomyocyte Ca^{2+} dynamics includes the calcium release unit (the LCC and the RYR), the sarcolemmal and sarcoplasmic Ca^{2+} pump, the Na^+-Ca^{2+} exchanger, the background Ca^{2+} channel, and SR leak Ca^{2+} channel described by Hinch et al. (2004). The model also accounts for dynamic changes in ionic concentrations and fluxes during the AP.

The process of modelling had another specific aim: to demonstrate the model reuse capabilities of OpenCOR, using individual components such as those described above. I constructed each constituent of the model separately. Once I had checked whether each simulation worked well, I obtained all numerical values using the comma-separated variables

(CSV) file. Then I plotted the behaviour of the simulated components and justified them using experimental data provided in reference models. During the incorporation of all components, I updated the LCC kinetics and SERCA activity based on my results, as the interplay between LCC activity and Ca^{2+} transients were critical to this study.

The fully integrated model is a system of ordinary differential equations implemented in OpenCOR (http://*opencor.ws*) using CVODE solver with a relative tolerance (1E-7) and an absolute tolerance (1E-7). Each component, including the child components with it along with their connections and units, was imported into the new model. The parameters for the resulting model were adapted by fitting to experimental measurements from the literature or from my own results. All simulations were performed on a 2.4 GHz Intel® Core™2 Duo CPU computer using a Microsoft Windows XP operating system.

The validation of each component model and the new integrated model are presented in Chapter 5 and a full list of model equations, parameters and initial conditions, are provided in Appendix A.

2.5.1 Model Units

To construct a mathematical model requires strict adherence to consistent units. The units are derived from basic physical quantities defined by the *Système International d'Unites* (SI). By combining two previous models, I could achieve the conversion of several units in a semi-automated manner.

Table 2.1. Summary of units for physical quantities in the modelling framework.

	Quantity	SI units	Units used in model
Base	length	meter (m)	µm
	time	second (s)	ms
	volume	cubic meter (m^3)	µL
	temperature	K	K
	current	ampere (A)	µA
Derived	voltage	volt (V)	mV
	concentration	molar ($mol \cdot L^{-1}$)	$mmol \cdot L^{-1}$
	conductivity	Siemen (S)	mS
	capacitance	farad (F)	pF

To convert the ionic fluxes into compatible currents the following equation was used (Terkildsen et al., 2008).

$$I = j \times z \times F \times vol_{myo} \qquad \text{Eq 2-4}$$

where I is the current in µA, j is the flux of Ca^{2+} ions in $mol \cdot L^{-1} \cdot s^{-1}$, z is the valence (e.g. +2 for Ca^{2+} ion), F is Faraday's constant in $C \cdot mol^{-1}$ and vol_{myo} is the volume of the myoplasm (cytosol) in µL.

2.5.2 Biophysically-based Modelling

Developing a biophysically-based model involves reproducing a cellular phenomenon observed experimentally in terms of the activity of subcellular components including the sarcolemmal/sub-organelle ion channels and transport systems. The activity of subcellular components can be represented by simplified mathematical expressions which are fitted to experimental data.

Most biophysical models of excitable cells are based on the Hodgkin–Huxley equations (Hodgkin and Huxley, 1952). The ion current flows through voltage- and time-dependent ion channels. The Hodgkin–Huxley formulation describes this current flow of an ionic species through a particular area of membrane.

$$I_S = f_S\overline{G_S}(V_m - E_S) \qquad \text{Eq 2-5}$$

where f_S is the proportion of channels in an open state, $\overline{G_S}$ the maximal conductance of the channel, V_m the potential difference across the membrane and E_S the Nernst potential for ionic species (*S)*.

Total current flow through a membrane is expressed as

$$I_{ion} = C_m\frac{dV_m}{dt} + \sum I_n \qquad \text{Eq 2-6}$$

where C_m is the capacitance of the cell membrane per unit area, V_m the transmembrane voltage and I_n the current per unit area flowing through individual ion channels, exchangers and pumps.

The dynamic changes of ionic concentrations during the AP are given by

$$\frac{d[x]}{dt} = -\left(I_x \times \ A_{Cap}\right)/(V_c \times Z_x \times F) \qquad \text{Eq 2-7}$$

where [*x*] is the concentration of ion X, I_x is the sum of ionic currents carrying ion X, A_{Cap} is the capacitive membrane area, V_c is the volume of the compartment where *[X]* is updated, Z_x is the valence of ion X, and *F* is the Faraday constant.

Chapter 3

Comparison of Stress Development between Left and Right Trabeculae in the Rat Heart

---

Trabeculae carneae are the smallest intact units of functional myocardium and have advantages for experimentation in that the production of force is uniaxial and the small radii of trabeculae enable the avoidance of anoxic conditions. The contractile performance (i.e. force-production) of trabeculae carneae is generally normalized to the cross-sectional area of the contractile machinery to yield estimates of muscle stress, which are impossible to measure in the whole heart due to technical limitations. *In vivo* heart rate range or load-dependent effects can be performed in the isolated trabeculae, more easily than in isolated myocytes.

3.1 Stress-Frequency Relationships

In order to compare the SFR between LV and RV trabeculae, a range of stimulus frequencies was applied to muscles equilibrated at optimal length. To ensure stability, I returned to the reference frequency of 5 Hz after each varying stimulus frequency.

Figure 3.1 shows the original recordings of the developed stresses measured at different frequencies. When the frequency was changed, the initial stress was quite different, but at steady-state the developed stress levels converged to a constant value. The change in diastolic stress between the intermediate reference frequency (5 Hz) and each test frequency was usually obvious.

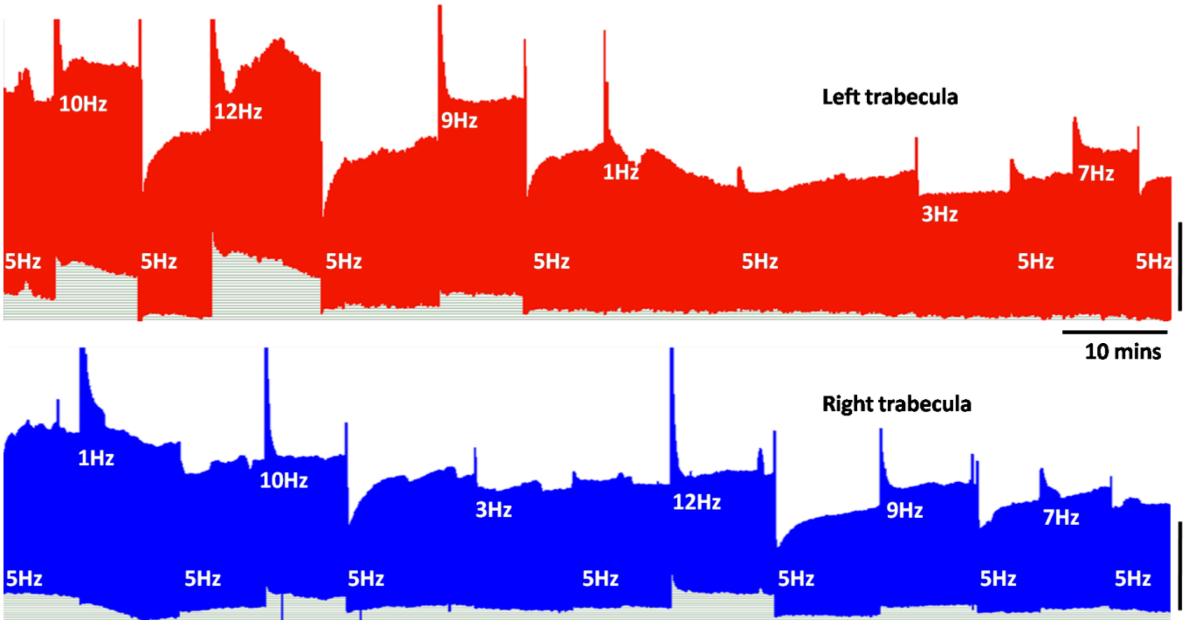

Figure 3.1. Typical developed stress responses to different stimulation rates. Representative raw developed stress signals were recorded from LV and RV trabeculae stimulated in order (10, 12, 9, 1, 3, and 7) Hz and (1, 10, 3, 12, 9, and 7) Hz between exposures to the reference frequency of 5 Hz, respectively.

I analysed the characteristics of each quasi-isometric twitch at each of the stimulation frequencies. The developed stress corresponding to each frequency tested was measured at steady-state, and then normalized to the stress at 5 Hz.

Twitch time constants (TPF and RT_{50}) and the maximum rate of stress development (dS/dt^{c}_{max}) during contraction were also evaluated (Figure 3.2).

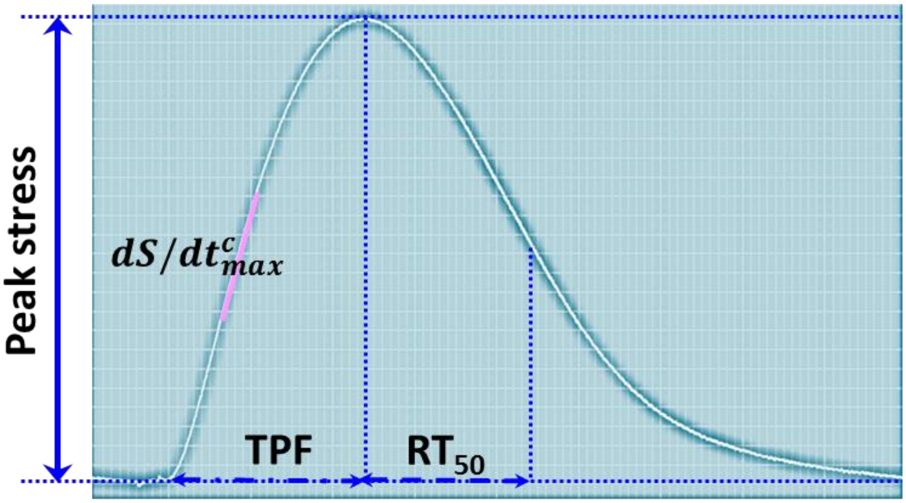

Figure 3.2. Schematic representations of total duration of a single twitch partitioned into peak stress, twitch duration (TD = TPF + RT_{50}), time to peak force (TPF), time to return to 50% of peak force (RT_{50}), and the maximum rate of stress development (dS/dt^{c}_{max}) during contraction.

Figure 3.3 shows each developed stress measured at steady-state at frequencies corresponding to the raw data shown in Figure 3.1. The effect of shortening twitch duration was more obvious than reduction in developed stress, as frequency was increased.

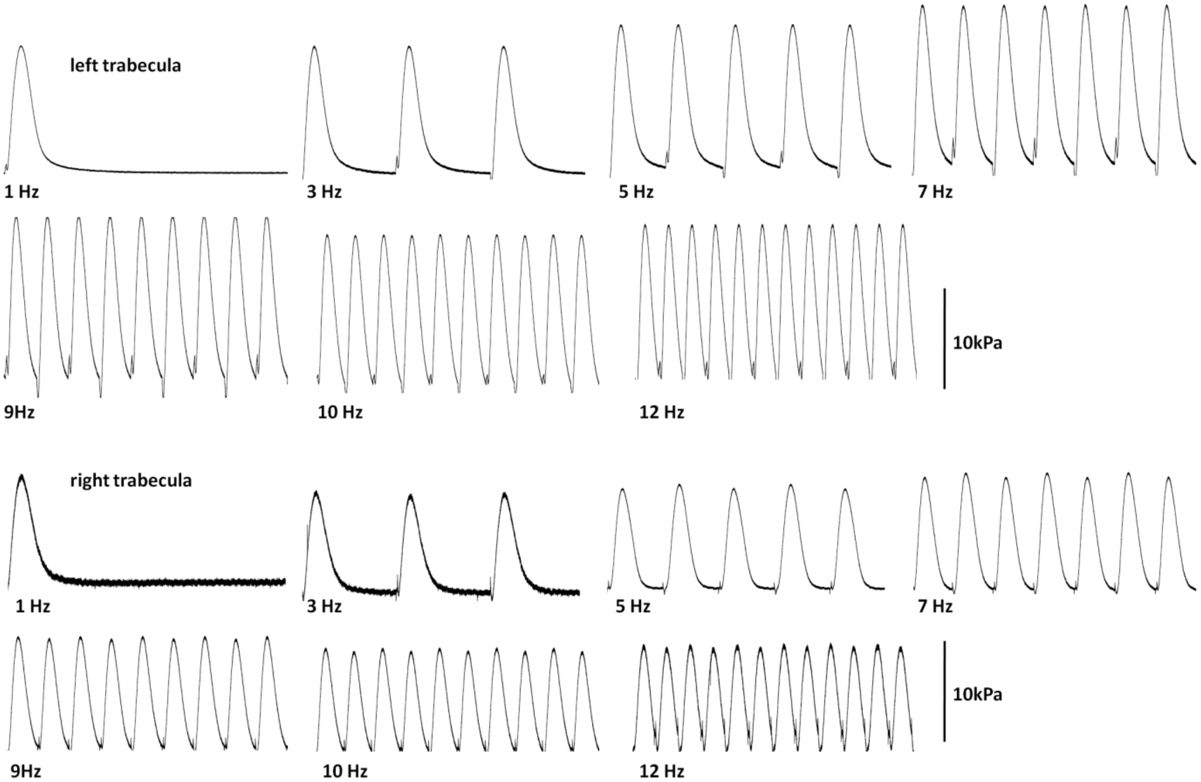

Figure 3.3. Representative developed stresses at steady-state from data of Figure 3.1. The time duration of each block is 1 second.

Figure 3.4 shows average data for SFR in LV and RV trabeculae. Over the range of stimulation frequencies used, stress production remained approximately constant, with a minimum of ~12 kPa at 3 Hz and ~10 kPa at 7 Hz and maximum of ~14 kPa at 5 Hz and ~12 kPa at 1 Hz in LV and RV trabeculae, respectively.

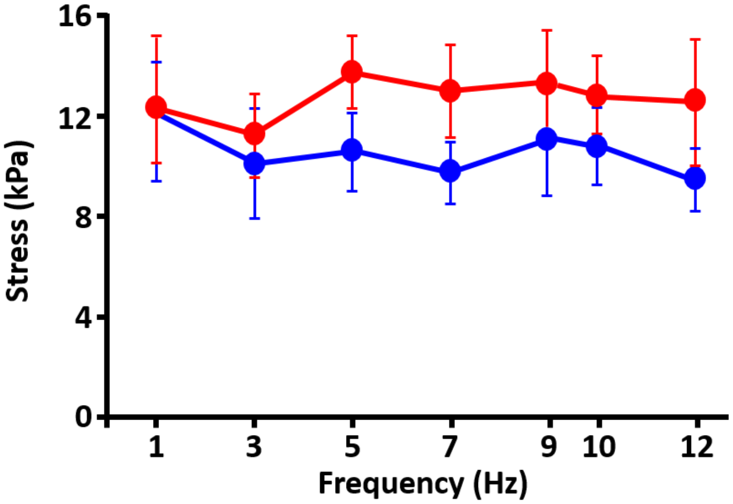

Figure 3.4. Stress-frequency relationships in LV and RV trabeculae at 37.5°C. Average results for SFR in LV (red circles, n = 7) and RV (blue circles, n = 9) trabeculae. Data points are mean ± S.E.M.

Both groups showed a similar pattern; the developed stress in the trabeculae displayed a flattened pattern as frequency increased from 1 Hz to 12 Hz. There was no significant difference in the developed stress between LV trabeculae and RV trabeculae.

The influence of frequency on diastolic stress is shown in Figure 3.5. The diastolic stress-frequency relationship was positively linear in both groups and at 7 Hz and 9 Hz there was a significant difference between diastolic stress in LV trabeculae and that in RV trabeculae.

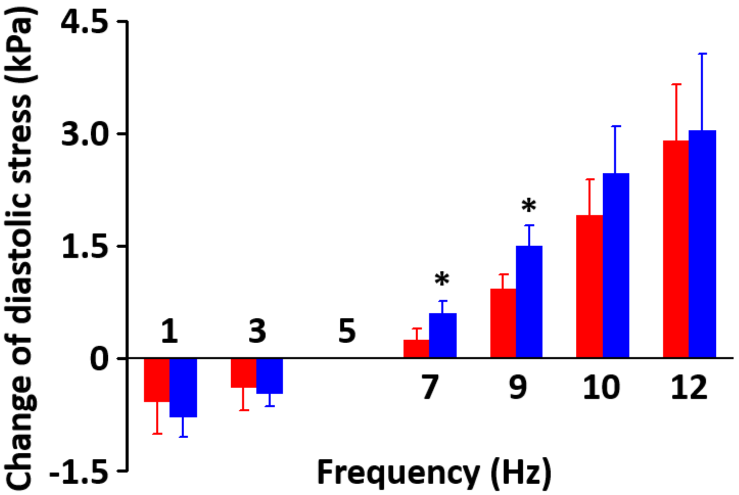

Figure 3.5. The averaged diastolic stress-frequency relationship in LV (red column; n = 4*)* and RV (blue column; n = 5) trabeculae. The data were expressed as difference in stress measured at 5 Hz. Data points are mean ± S.E.M. **P* < 0.05 compared to left trabecula.

TPF diminished with increasing frequency in both groups, and was significantly slower in LV trabeculae than in RV trabeculae (Figure 3.6A). Similarly, RT_{50} also declined with increasing frequency in both groups and was significantly slower in LV trabeculae than in RV trabeculae (Figure 3.6B). The value of TD for LV trabeculae is greater than that of RV trabeculae (Figure 3.6C). Significant differences between LV and RV trabeculae were observed in all parameters at all frequencies.

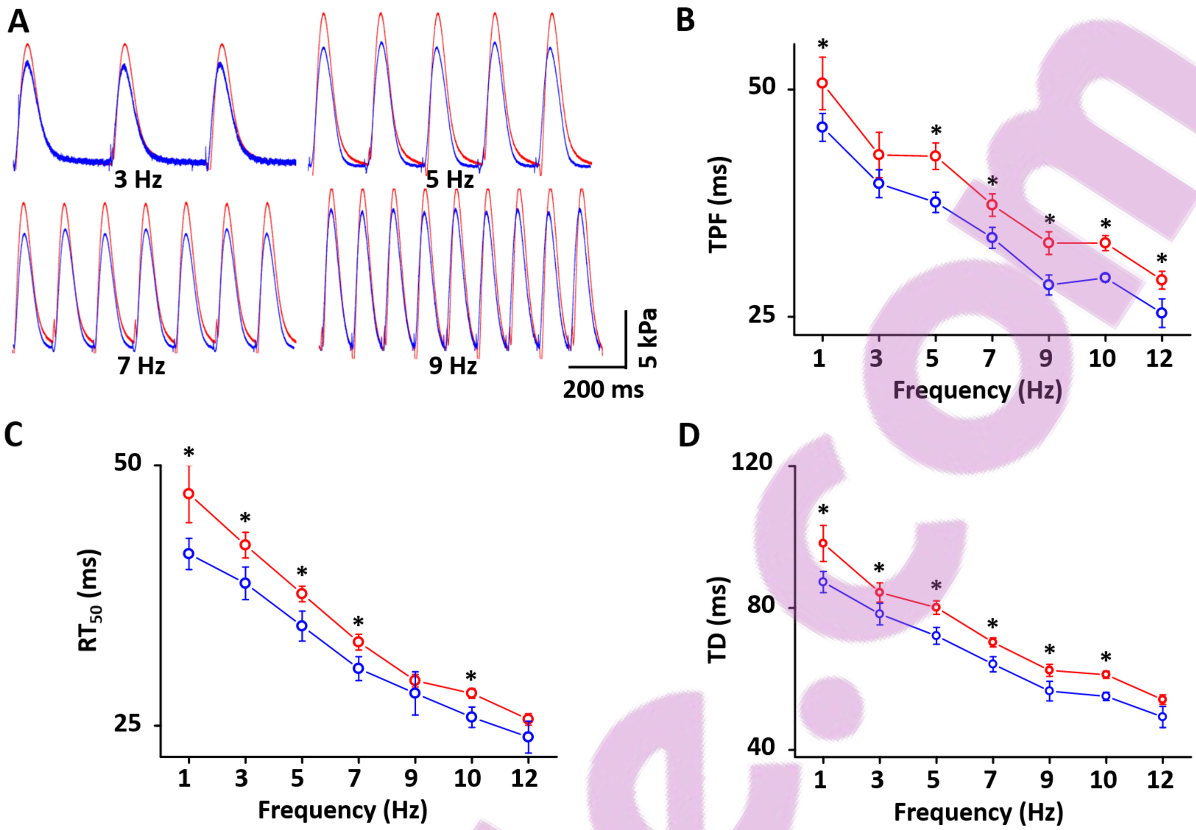

Figure 3.6. Summary of twitch time constants. A: The overlapped traces of representative stresses measured at 3, 5, 7, and 9 Hz in LV and RV trabeculae. B: the averaged TPF-frequency relationship in LV and RV trabeculae. C: the averaged RT_{50}-frequency relationship in LV and RV trabeculae. D: the averaged TD-frequency relationship in LV and RV trabeculae. LV (n = 7), red circle. RV (n = 8), blue circle. Data points are mean ± S.E.M. *$P < 0.05$ compared to left trabecula.

For further experiments (Chapter 3.2 and 3.3) I selected the three stimulus frequencies (5, 7, and 10 Hz) that lie within an acceptable physiological range: the resting heart rates of rats lie within the range of 5 Hz - 7 Hz at 37°C (Vornanen, 1992) and a frequency of 9 Hz - 10 Hz is maximal for a rat *in vivo* (Basile-Filho et al., 1991).

3.2 β-Adrenergic Response

Next, I investigated the effect of ISO (β-adrenergic stimulant) on SFR (peak stress). Increasing heart rate is expected to be accompanied by sympathetic activation *in vivo*. To clarify this anticipated β-adrenergic regulation of SFR, I treated the trabeculae with ISO and proceeded to measure the SFR.

Figure 3.7 shows the cumulative concentration-response curve obtained by raising the ISO concentration in semi-log steps from 1 nmol·L^{-1} to 1 μmol·L^{-1}; EC$_{50}$ was 22.5 nmol·L^{-1} ± 16.6 nmol·L^{-1} (n = 3).

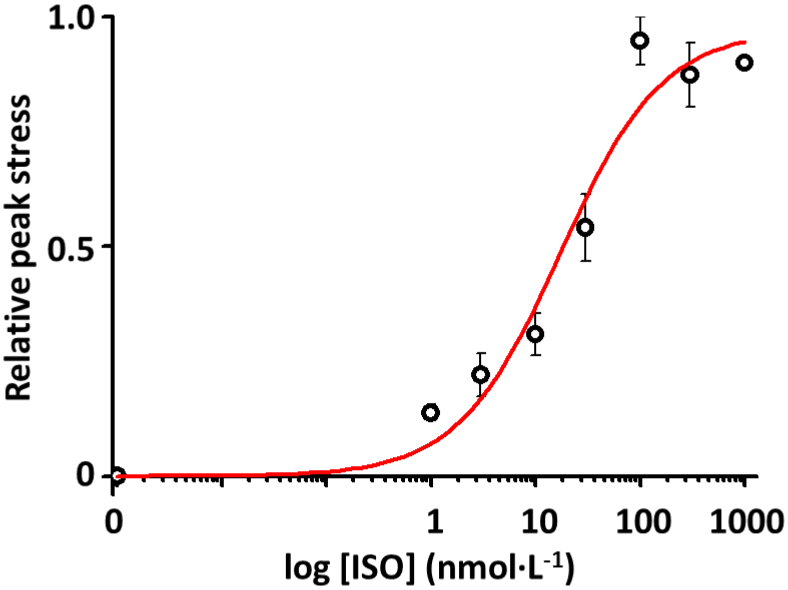

Figure 3.7. Dose-response relationship of ISO in LV trabeculae (n = 3). At 37.5°C and a stimulation frequency of 5 Hz, EC$_{50}$ was calculated by fitting with the Hill equation.

Based on this result, further experiments were performed with 20 nmol·L^{-1} ISO, and 200 nmol·L^{-1} ISO as a higher dose. I measured the SFR in the presence of ISO and normalized each stress measurement to that measured without ISO at each frequency. Figure 3.8 shows typical raw traces demonstrating the effects of ISO on LV and RV trabeculae. These results are summarized in Figure 3.9.

The effect of ISO on SFR was different between LV and RV trabeculae. ISO, at a predetermined EC_{50} of 20 nmol·L^{-1}, slightly increased stress at 5 Hz and 7 Hz and significantly increased stress at 10 Hz in both trabeculae. At a concentration of 200 nmol·L^{-1}, ISO significantly increased stress at all frequencies in trabeculae from either ventricle. Interestingly, in RV trabeculae, the response was significantly augmented compared to LV trabeculae. To clarify the SFR induced by ISO, I measured the stresses at steady-state and normalized each stress to that produced at 5 Hz. Frequency treppe ('staircase') was observed only in RV trabeculae without ISO treatment, although this phenomenon was clearly revealed in both LV and RV trabeculae with ISO treatment.

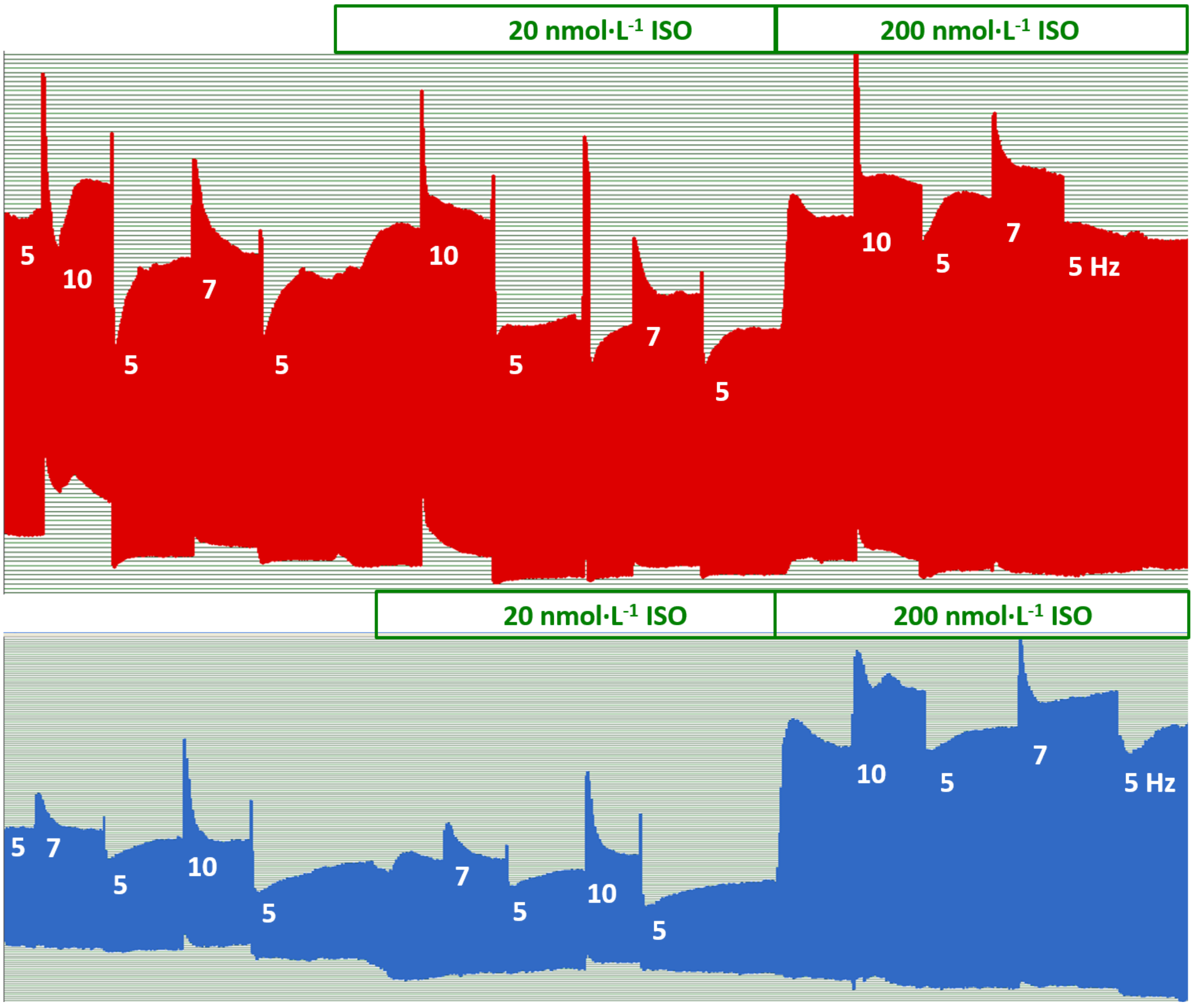

Figure 3.8. Typical developed stress response to ISO. Representative raw developed stress signals were recorded from LV (red trace) and RV (blue trace) trabeculae. See Figure 3.1 for scales.

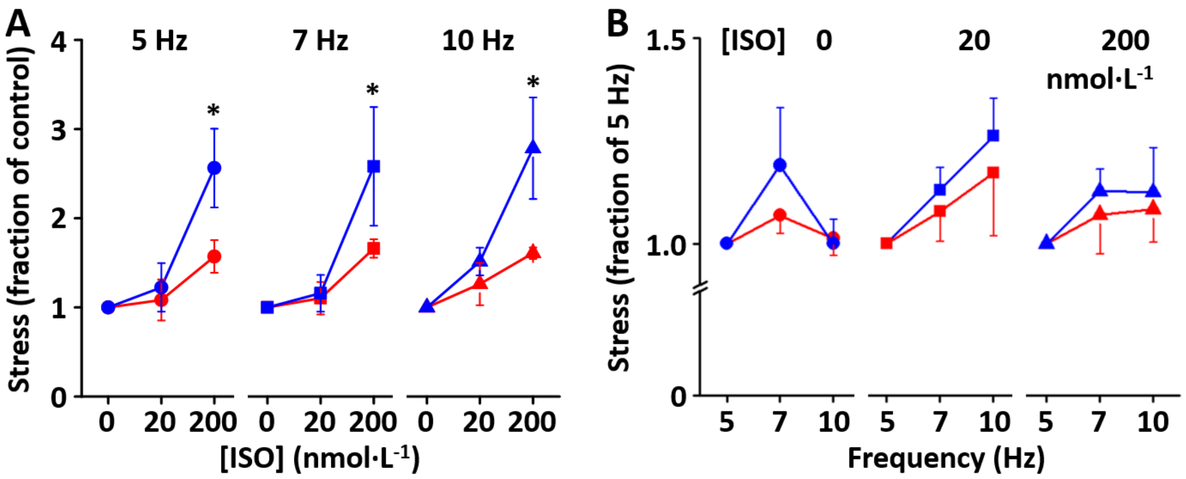

Figure 3.9. Comparison of the effect of ISO on SFR between LV and RV trabeculae at 37.5°C. A. The averaged effect of ISO treatment on LV (red, n = 5) and RV (blue; n = 5) trabeculae at each frequency (5 Hz; circle, 7 Hz; square, 10 Hz; triangle). B. The averaged stress-frequency relationship to ISO treatment in LV (red, n = 5) and RV (blue; n = 5) trabeculae. SFR is normalized to the stress at 5 Hz of each LV and RV trabecula. The concentration of ISO is reflected in the plot by symbol shape (circle = 0, square = 20, triangle = 200 nmol·L^{-1}). Note that the SFR at zero ISO is flat in both but the SFR at 20 nmol·L^{-1} (a physiological concentration) has a positive slope only in RV trabeculae. Data points are mean ± S.E.M. *$P < 0.05$ compared to left trabecula.

Interestingly, ISO diminished diastolic stress across most of the measured SFRs. When I examined the change of diastolic stress at 5 Hz, 20 nmol·L^{-1} ISO significantly lowered diastolic stress in both LV and RV trabeculae but 200 nmol·L^{-1} ISO did not (Figure 3.10A). With ISO, diastolic stress decreased on average by 6% from 5 Hz to 7 Hz in RV trabeculae while it remained constant in LV trabeculae (Figure 3.10B). These changes in diastolic stress in response to ISO took place in both LV and RV trabeculae from 5 Hz to 10 HZ.

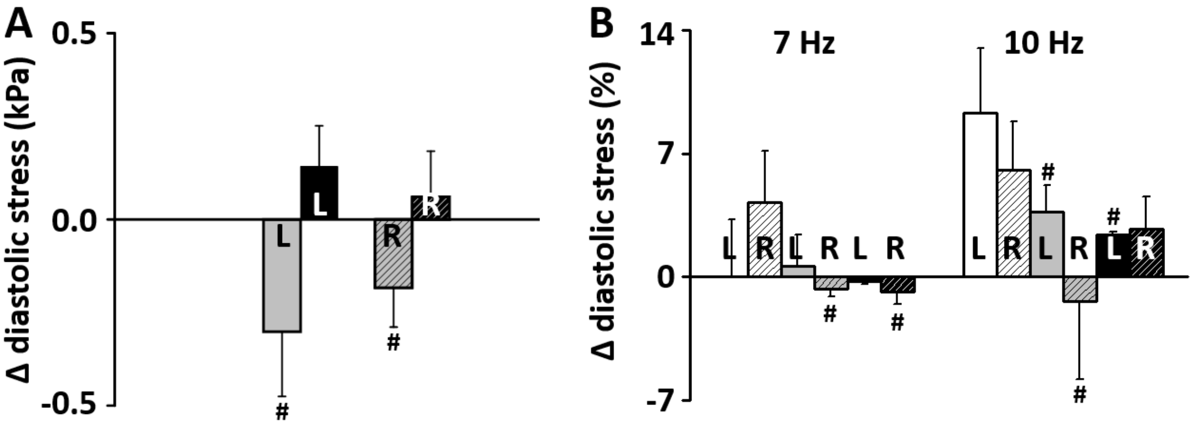

Figure 3.10. A. Summary of the changes in diastolic stress at 5 Hz in LV (non-textured columns, n = 5) and RV (textured columns; n = 5) trabeculae. B. Summary of the changes in diastolic stress from 5 Hz to 7 Hz or 10 Hz in LV (non-textured columns, n = 5) and RV (textured columns; n = 5) trabeculae. Data points are mean ± S.E.M. The concentration of ISO is reflected in the plot as increasing colour intensity (white = 0, grey = 20, black = 200 nmol·L^{-1}). #*P* < 0.05 compared to the control.

Figure 3.11 shows that twitch time constants declined with increasing concentrations of ISO; the response was significant at 5 Hz and 7 Hz in both trabeculae; however, at higher frequency these changes occurred only at 200 nmol·L^{-1} ISO in trabeculae from both ventricles.

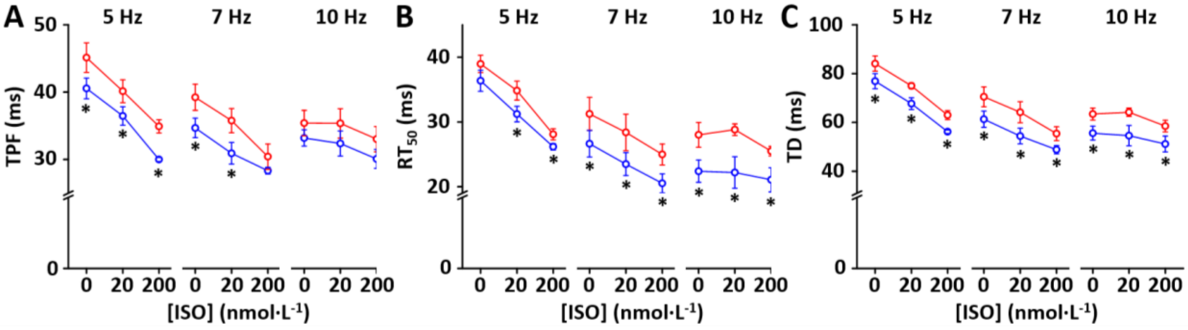

Figure 3.11. Summary of twitch time constants: A. The averaged TPF-frequency relationship with ISO treatment in LV and RV trabeculae. B. The averaged RT$_{50}$-frequency relationship with ISO treatment in LV and RV trabeculae. C. The averaged TD-frequency relationship with ISO treatment in LV and RV trabeculae. LV (n = 5), red circle. RV (n = 5), blue circle. Data points are mean ± S.E.M. **P* < 0.05 compared to left trabecula.

3.3 Non-selective Adrenergic Response

To elucidate the effect of NE on the SFR, I measured the stress at 20 nmol·L^{-1} NE, which is the concentration required to produce measurable hemodynamic or metabolic changes *in vivo* in the rat (Watanabe et al., 2003). The effect of NE on SFR was somewhat different from that of ISO. NE showed a similar increase in developed stress against the identical control trace in both trabeculae (Figure 3.12).

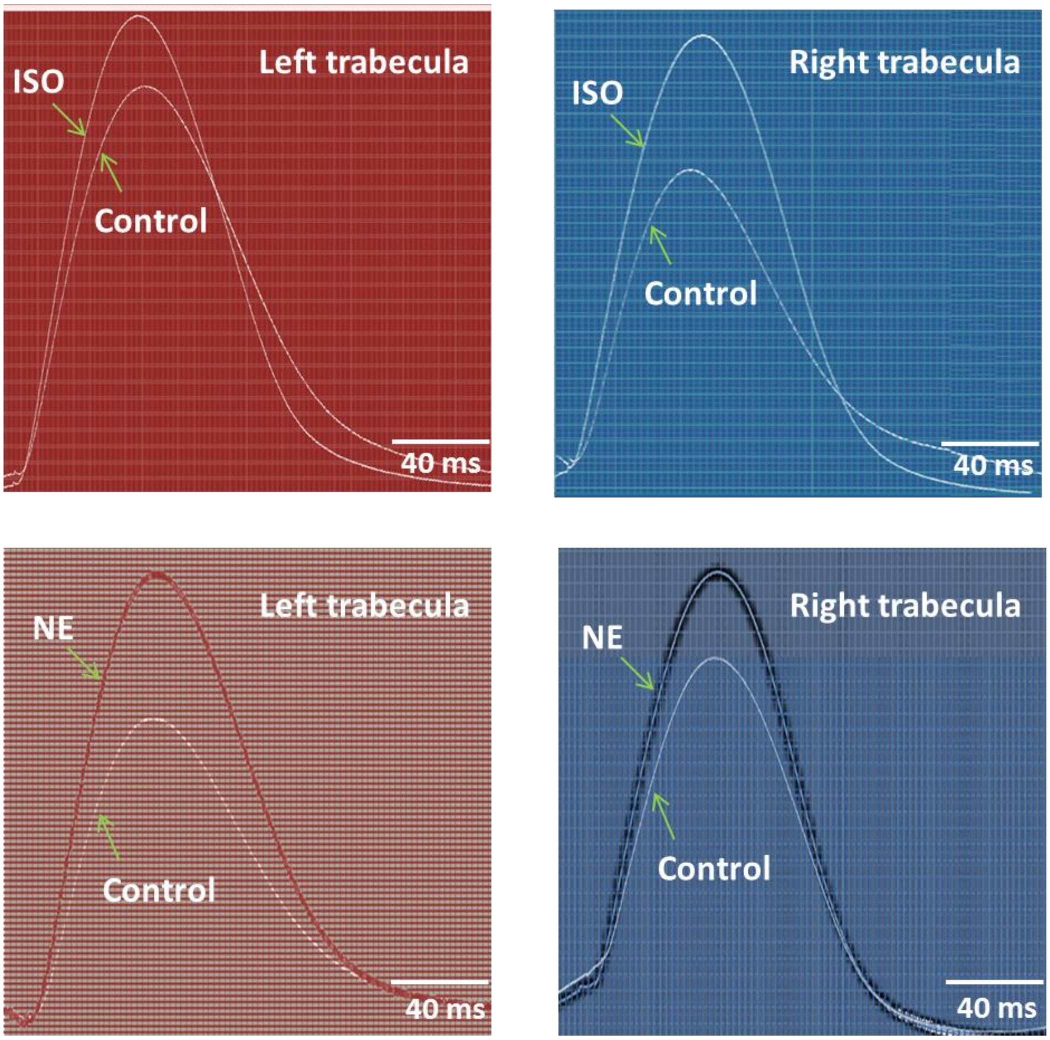

Figure 3.12. Representative developed stress response to ISO or NE. These raw traces of developed stress signals were recorded from LV and RV trabeculae at 5 Hz. Each control trace is normalized.

The effects of NE on SFR in LV and RV trabeculae are summarized in Figure 3.13. The degree of stress increment is similar across the two groups.

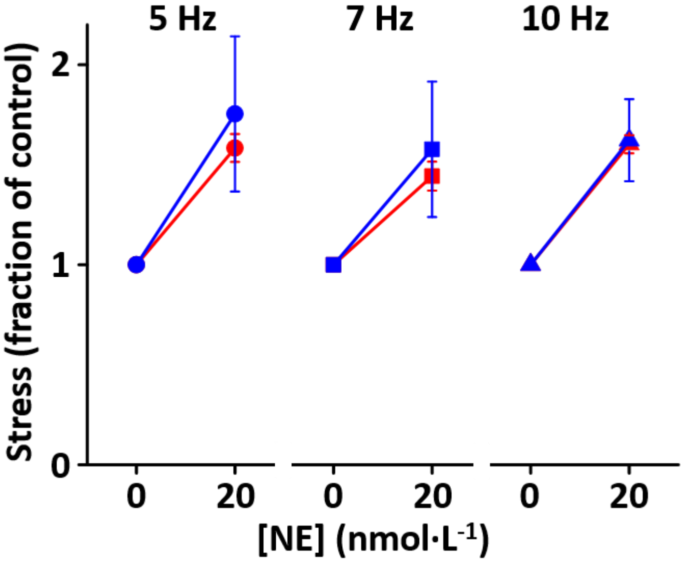

Figure 3.13. Comparison of the effect of NE on SFR between LV and RV trabeculae at 37.5°C. The averaged stress-frequency relationship to NE treatment in LV (red, n = 4) and RV (blue; n = 2) trabeculae at each frequency (5 Hz; circle, 7 Hz; square, 10 Hz; triangle). Data points are mean ± S.E.M.

Interestingly, diastolic stress significantly increased at 7 Hz in both RV and LV trabeculae, and significantly decreased at 10 Hz in RV trabeculae (Figure 3.14). As shown in Figure 3.15, twitch time constants were not significantly changed by NE in either group of trabeculae.

I also analysed and compared the SFR and the maximum rate of stress development (dS/dt^{c}_{max}) in ISO or NE treatment (Figure 3.16). The positive SFR properties of both RV and LV trabeculae responded to ISO or NE. When comparing dS/dt^{c}_{max} at a concentration of 20 nmol·L^{-1}, NE showed a low slope compared to ISO.

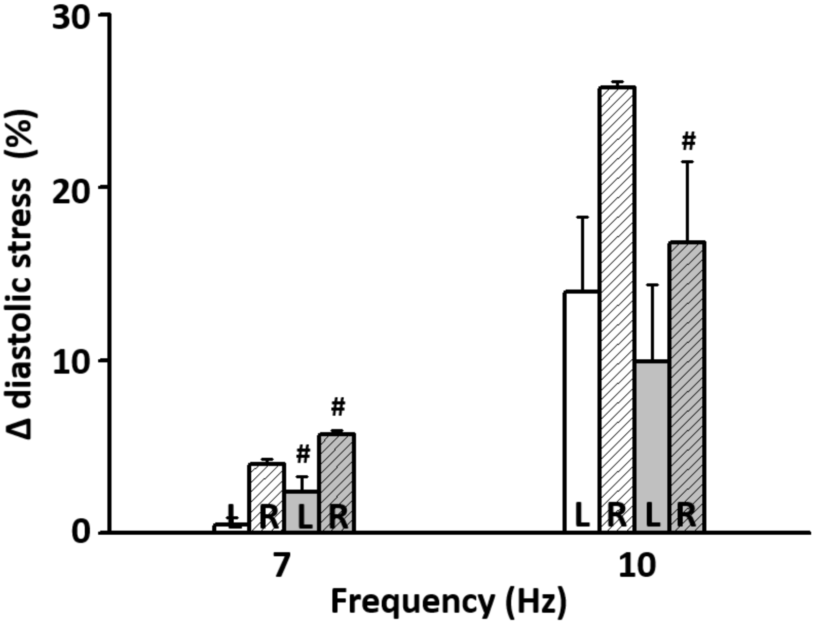

Figure 3.14. Summary of the change in diastolic stress from 5 Hz to 7 Hz or 10 Hz in LV (non-textured columns, n = 4) and RV (textured columns; n = 2) trabeculae. Data points are mean ± S.E.M. Grey scale indicates NE treatment (white = 0, grey = 20 nmol·L^{-1}). #P < 0.05 compared to the control.

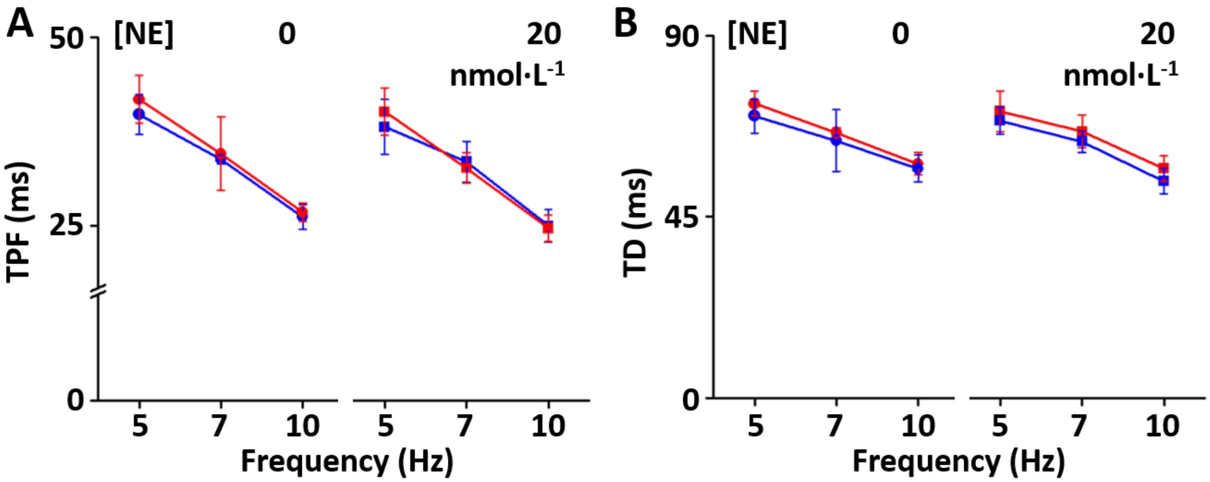

Figure 3.15. Summary of twitch time constants. A. The averaged TPF-frequency relationship to NE treatment in LV (red, n = 4) and RV (blue, n = 2) trabeculae. B. The averaged TD-frequency relationship to NE treatment in LV (red, n = 4) and RV (blue, n = 2) trabeculae. The concentration of NE is reflected in the plot by symbol shape (circle = 0, square = 20 nmol·L^{-1}). Data points are mean ± S.E.M.

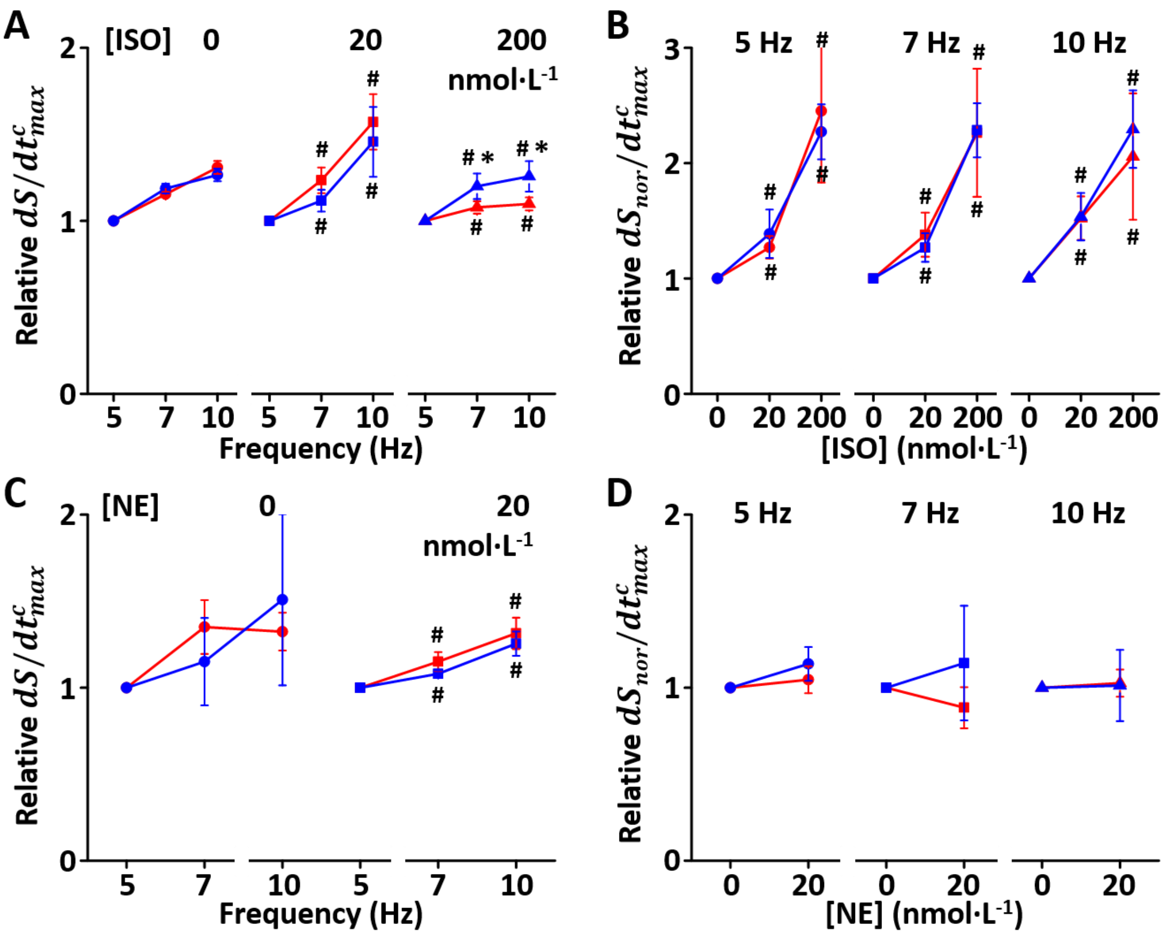

Figure 3.16. Plot showing the relationship between frequency and maximum rate of stress development (dS/dt^c_{max}) in the presence of ISO or NE. A and B. The average dS/dt^c_{max}-frequency and dS/dt^c_{max}-concentration relationships in response to ISO treatment, respectively, in LV (red, n = 5) and RV (blue, n = 5) trabeculae. C and D. The average dS/dt^c_{max}-frequency and dS/dt^c_{max}-concentration relationships to NE treatment, respectively, in LV (red, n = 4) and RV (blue, n = 2) trabeculae. dS/dt^c_{max} is represented as percentage change from that measured at the baseline frequency (5 Hz). *$P < 0.05$ compared to the LV trabeculae. #$P < 0.05$ compared to the control.

3.4 Discussion

The main findings of the present study are: (1) stress did not differ significantly between LV and RV trabeculae and the SFR in both groups was flat in the range of physiological frequencies applied at 37°C; (2) β-adrenergic stimulation resulted in a positive SFR with significant reduction in the twitch time constants and increase in the maximum rate of stress development in both groups in the range of physiological frequencies at 37°C; and (3) non-specific adrenergic stimulation produced increased stress, but unchanged flattened SFR and twitch time constants in both groups in the range of physiological frequencies at 37°C.

3.4.1 Stress and Frequency

The SFR in trabeculae or correspondingly the force-frequency relationship (FFR) in whole heart, with the Frank-Starling law, is well-known as one of the most important intrinsic factors responsible for control of cardiac contractility in physiological conditions (Holubarsch et al., 1996). The Frank-Starling law is based on a length-tension relationship, and is quite clearly manifest in the LV, which is far more preload dependent than the RV (Santamore and Dell'Italia, 1998). Wall thickness is far less and elastance is lower in the RV than the LV; therefore, the RV is far more afterload-dependent than the LV (Walker and Buttrick, 2009). In addition, the structural and mechanical properties of the RV are distinct from those of the LV. Despite these differences, to immediately meet the demand of vital organs, the ventricles should contract synchronously with identical cardiac output under various circumstances.

In this study, for any given frequency, each trabecula has mostly similar steady-state stress regardless of marked differences in the initial stress. Also there was no difference in inherent stress between trabeculae from the LV and the RV; however, RV trabeculae had a shorter time to peak force and relaxation time than LV trabeculae. These results are supported by other studies. Rouleau et al. (1986) demonstrated that RV muscles shortened faster and their time to attain peak total tension was shorter than that of LV muscles in dogs (Rouleau et al., 1986). Suga et al. (1973) provided evidence that increases in the paced heart rate proportionally shorten the time to peak systole without any effect on the peak value of end-systolic elastance (Suga et al., 1973). Under normal circumstances, the right chamber pressure presents a lower load against which the RV ejects blood than does the left chamber, and also shows an earlier systolic peak and more rapid pressure decline (Dell'Italia and Walsh, 1988b). In support of this, a model of pulmonary hypertension showed adaptation of the RV by decreasing muscle shortening velocity and by increasing the time to attain peak total tension to eject against a high pressure system (Alpert and Mulieri, 1982).

The above results suggest that mechanical differences exist between LV and RV myocardium in term of either cellular components or Ca^{2+} regulating mechanisms.

The mechanisms involved in SFR have been suggested to centre primarily on increased Ca^{2+} availability to the contractile proteins as consequence of the following: the increased number of APs per minute leads to increase SR Ca^{2+} storage with augmented Ca^{2+} transients through the activation of LCCs (Borzak et al., 1991; Wier and Yue, 1986); reduced Ca^{2+} efflux through the NCX in diastole leads to increase cytosolic Ca^{2+} accumulation (Subramani et al., 2005; Vila Petroff et al., 2003). Recently, Ca^{2+}/calmodulin-dependent protein kinase IIδ (CaMKIIδ) phosphorylation of RYR2 has been suggested to play an important role in mediating positive FFR in the heart, with defective regulation of RYR2 by CaMKIIδ-mediated phosphorylation being associated with the loss of positive FFR in failing hearts (Kushnir et al., 2010).

Changes in the time to attain peak total tension and the velocity of muscle shortening have a close relationship with changes in AP duration. For example, an increase in AP duration occurs in hypertrophied myocardium in response to an increase in afterload, which leads to an increase in the time to attain peak total tension, and a decrease in the velocity of muscle shortening (Keung and Aronson, 1981). Furthermore, Watanabe et al. (1983) showed that the shorter AP duration of the RV as compared to the LV is accompanied by a shorter time to attain peak total tension and by a slower velocity of muscle shortening in rats.

The differences observed in muscle mechanics in my study, as well as in other studies, may be related to differences in the expression and activity of Ca^{2+} modulation-related proteins. Some differences in cellular calcium kinetics between RV and LV myocardium have been described (Saari and Johnson, 1980) and I examined these further to compare Ca^{2+} handling between LV and RV myocytes (see Chapter 4).

Brooks et al. (1987) showed that the force generation of RV papillary muscle per unit mass is similar to that of LV papillary muscle, although the shortening velocity of isolated RV muscle is greater than that of the LV. They measured the difference in myosin heavy chain isozyme expression that is associated with a higher ATPase activity in the RV and LV; that is, the level of α-myosin heavy chain isozyme in the RV is significantly higher than in the LV in both rats and rabbits.

The SFR/FFR has an important effect when myocardial performance reduces as systolic volume decreases (Frank-Starling relation), because SFR leads to an increase in contractile strength and so compensates for the Frank-Starling effect. However, my observation of the SFR (relatively flattened), suggests that innate myocardial stress is independent of frequency, which does not agree with the biphasic or positive SFR results in previous studies (Kassiri et al., 2000; Layland and Kentish, 1999). This discrepancy could be due to differences in experimental conditions: in case of biphasic SFR, only RV trabeculae of rat heart were stimulated at 0.2, 0.5, 1, and 2 Hz at room temperature; in the case of positive SFR, the protocol to stimulate the trabeculae was repeated for successively increasing test frequencies (0.1 - 12 Hz) and then repeated with decreasing stimulation frequency.

In this study, both groups of trabeculae showed a significant depression of stress beyond the maximal physiological range (12 Hz), in accordance with previous studies which demonstrated an increase of contractile force as heart rate increased, followed by a decline with excessive increase in heart rate (Alpert et al., 1998). In contrast, my results are different from a previous study (Wang et al., 2008) in which RV trabeculae in the mouse showed a positive SFR in the range of frequencies investigated (4 Hz - 14 Hz).

3.4.2 Adrenergic Stimulation and SFR

Cardiac output is the product of stroke volume and heart rate. However, increased heart rates reduce diastolic filling time, which reduces stroke volume. For example, during exercise, tachycardia is accompanied by a decrease in end-diastolic volume despite a progressive increase in filling pressure, so that stroke volume is maintained by a decrease in end-systolic volume (Higginbotham et al., 1986). This suggests that positive FFR (see Figure 3.9B) can prevent the reduction of stroke volume at faster heart rates and ensure an enhanced cardiac output.

Under physiological conditions, increasing heart rate is accompanied by autonomic system input. Therefore, understanding the control mechanism for cardiac contractility requires the application of adrenergic stimulation to verify the regulation of SFR.

When I explored the effect of β-adrenergic stimulation, I found that the SFR of both LV and RV trabeculae showed a positive relationship. This finding is consistent with others in the literature (Kambayashi et al., 1992; Kassiri et al., 2000; Ross et al., 1995).

The change of SFR in response to adrenergic stimulation has been mainly demonstrated as a net result of cardiac and systemic vascular responses *in vivo*. Interestingly, my results suggest that the positive SFR property of cardiac muscle per se mainly responds to β-adrenergic stimulation since the effect of NE on SFR was slightly augmented compared to that of ISO. This phenomenon is supported by a previous study that showed that β-AR stimulation opposes the α-AR effect of NE in cardiac muscle (Danziger et al., 1990).

The different responses of β-adrenergic stimulation in LV and RV trabeculae would possibly act to coordinate ventricular pumping action according to different flow circumstances. The RV adaptation to lower pressure leads to ejection of blood with lower resistance in physiological conditions. When β-adrenergic stimulation increases, both ventricles tend not only to increase developed stress but also to decrease twitch time constants. The changes were more prominent in RV trabeculae compared to LV trabeculae. Interestingly, the change in diastolic stress in LV trabeculae was greater than in RV trabeculae.

In particular, the SFR changed differently in the LV and RV trabeculae depending on the type of catecholamine. Only β-adrenergic stimulation significantly enhanced stress itself, in addition to SFR in both trabeculae, but especially in RV trabeculae. Furthermore, the slope of the SFR was steeper at 20 nmol·L^{-1} ISO than at 200 nmol·L^{-1} ISO. The profound change of SFR in RV trabeculae in response to β-adrenergic stimulation was accompanied by a decline in diastolic stress as well as shorter TPF and RT$_{50}$ compared to LV trabeculae. This different response between the LV and RV trabeculae could be explained by other study that β-AR density was higher in the RV than in the LV of normal hearts and an alteration of this density distribution was found in failing hearts (Bristow et al., 1992).

Mechanisms underlying augmentation of SFR by β-adrenergic stimulation might include many factors, from activation of the membrane β-AR to SR Ca^{2+} modulation, which could increase the Ca^{2+} transient beyond that caused by increased frequency alone.

β-adrenergic stimulation activates a guanosine 5’-triphosphate-binding protein, leading to increased adenylate cyclase activity, which eventually increases the production of adenosine 3’,5’-cyclic monophosphate (cAMP). Increased cAMP results in phosphorylation of LCCs by cAMP-dependent protein kinase (PKA), which further enhances Ca^{2+} entry through the membrane (Piot et al., 1996; Trautwein and Hescheler, 1990). PKA also phosphorylates phospholamban (Kranias and Solaro, 1983; Lindemann et al., 1983), leading to disinhibits SERCA (Sasaki et al., 1992), which accelerates relaxation and enhances SR Ca^{2+} loading.

In contrast, the addition of nonspecific agonists (both α- and β-agonist) enhanced stress to the same extent in both RV and LV trabeculae without affecting twitch time constants and with slightly increased diastolic stress. The effect of NE on twitch time constants was consistent with a previous study (Rouleau et al., 1986). In fact, when cardiac muscle is stimulated by sympathetic nerves, NE simultaneously stimulates both α- and β-ARs. Therefore, verifying the effect of NE on SFR provides considerable understanding of the control mechanism of cardiac contractility under physiological conditions. Whereas both α- and β-agonists increase peak tension and rate of tension development, when tested each specific agonist separately, β-agonists have the additional effect of contraction and relaxation kinetics, while α-agonists do not (Danziger et al., 1990; Skomedal et al., 1982). In addition, Buxton and Brunton (1986) suggested that α-adrenergic stimulation by NE might attenuate the more predominant effect of β-adrenergic stimulation by NE via affecting the cAMP contents of cardiomyocytes in opposite direction (Buxton and Brunton, 1986). Danziger et al. (1990) also demonstrated that β-mediated effects predominate in the action of the physiological agonist NE on cardiac myocytes: NE decreased resting $[Ca^{2+}]_i$, increased SR Ca^{2+} content and increased LCC activity; β-adrenergic activation produced the same effect on resting $[Ca^{2+}]_i$ and SR Ca^{2+} content, but gave significantly greater activation of LCC activity, than did NE; α-adrenergic stimulation had no effect on resting $[Ca^{2+}]_i$ and SR Ca^{2+} content (Danziger et al., 1990). Interestingly, my study found that the effect of NE on SFR was significantly different from the effect of ISO.

Relaxation and diastolic stiffness is determined both by the cardiomyocyte cytoskeleton, including titin and structural and biochemical changes in the extracellular matrix (Kass et al., 2004). During β-adrenergic stimulation, PKA mediates phosphorylation of titin, which lowers titin-based passive stiffness in heart (Fukuda et al., 2005; Kruger and Linke, 2006). This chamber stiffness has been also known to reside in titin by protein kinase G (PKG) and protein kinase C (PKC) (Hidalgo et al., 2009; Kruger et al., 2009). Taken together, the changes of isoform composition and phosphorylation status of titin have been suggested to alter both diastolic function and myocardial passive properties (Borbely et al., 2009; Nagueh et al., 2004).

Based on this evidence, one of the possible explanations of my results is that the decrease in cardiomyocyte stiffness induced by ISO is associated with the modulation of titin's phosphorylation status by PKA, as shown in the previous studies (Fukuda et al., 2005; Kruger and Linke, 2006).

Chapter 4

Comparison of Ca^{2+} Handling between Left and Right Ventricular Myocytes

Cardiac Ca^{2+} signalling plays an important role in developing tension. The rise of intracellular Ca^{2+} concentration during contraction comes from Ca^{2+} entry across sarcolemma membrane and Ca^{2+} release from the SR. Then cytosolic Ca^{2+} is pumped both out of the cell by NCX (mainly in rat) and back into the SR by the SERCA during relaxation. These factors for Ca^{2+} determine both the magnitude and time course of the Ca^{2+} transient. Moreover, stimulation of the β-AR results in an increase in systolic intracellular Ca^{2+} concentration with a faster time to peak and decline.

Note that study of Ca^{2+} transients at the cellular levels helps to intrinsic properties of cardiomyocyte per se regarding of stress development and response to adrenergic stimulation between the LV and the RV.

4.1 Ca^{2+} Transients

To explain the underlying mechanism behind the different stress in LV and RV trabeculae, I examined the properties of the Ca^{2+} transient in isolated single myocytes from LV and RV at room temperature. A Ca^{2+} transient was elicited by field stimulation (1 Hz, 8 V) in each myocyte as shown in Figure 4.1. The peak fluorescence ratio was similar; however, the kinetics of decay was quite different between the RV and LV cells.

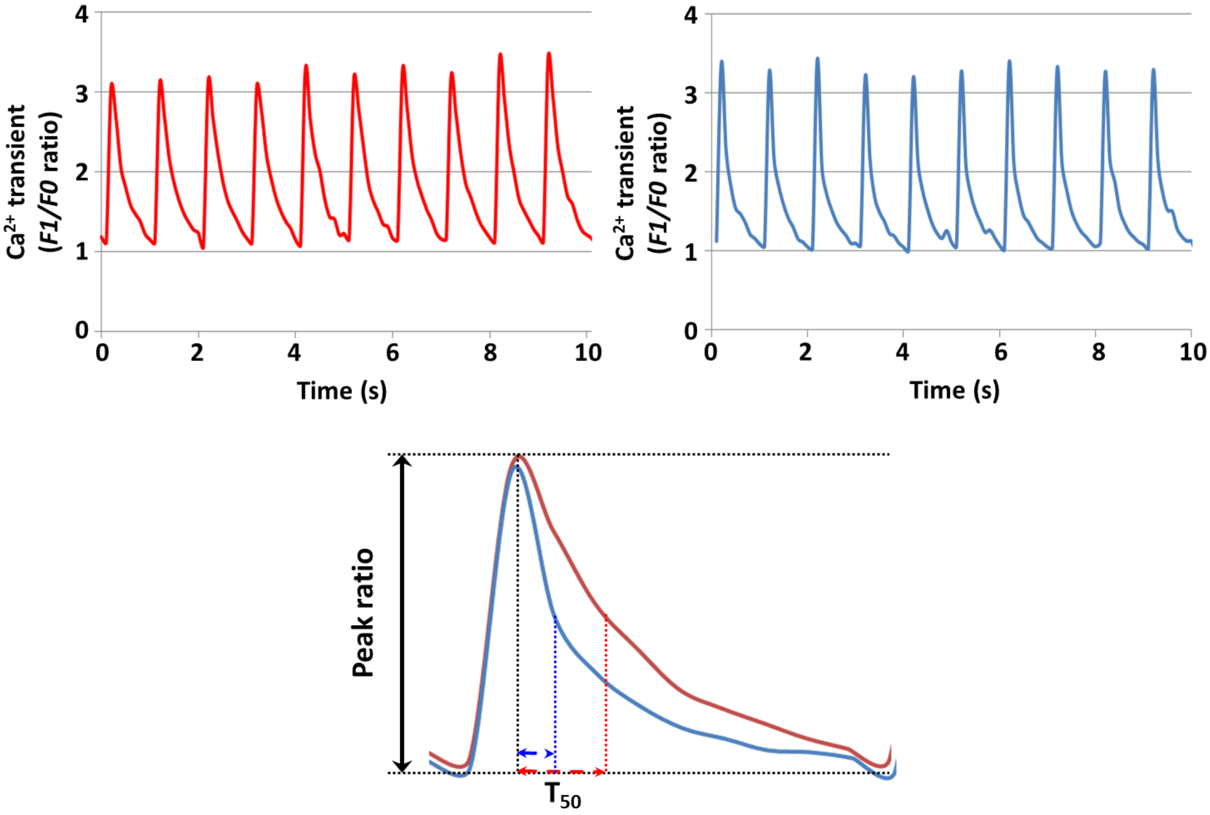

Figure 4.1. Ca^{2+} handling in isolated myocytes from LV and RV at room temperature. Representative tracing of Ca^{2+} transients in myocytes from LV (red line) and RV (blue line) paced at 1 Hz. To analyse the kinetics of decay, T_{50} (time to 50% decay from peak) was calculated and is shown in the lower panel.

In Figure 4.2, the average peak ratio of Ca^{2+} transients in the LV (2.1 ± 0.23, n = 6) and RV (2.88 ± 0.34, n = 6) myocytes was not significantly different; however, the decay of the Ca^{2+} transient was much faster in RV (132.8 ± 15.2, n = 6, $P < 0.05$ versus LV) than in LV myocytes (190.1 ± 24.8, n = 6).

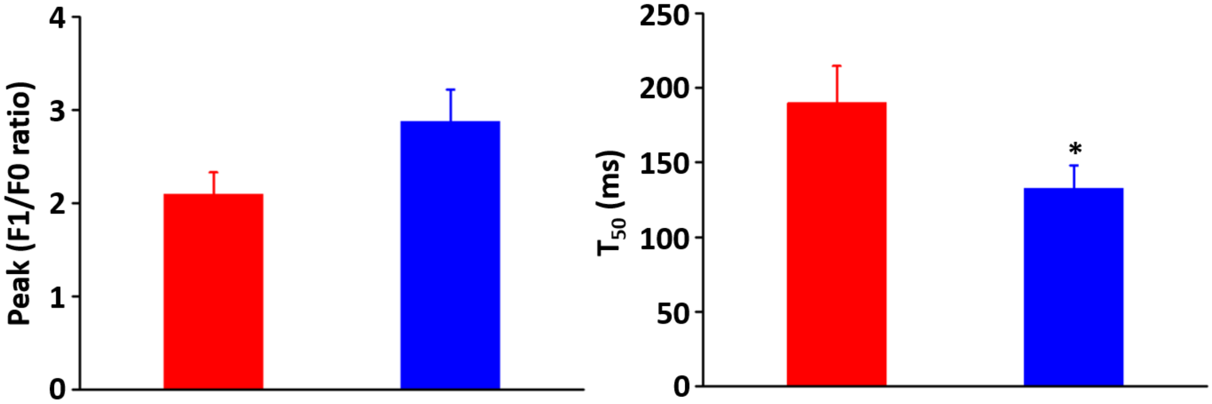

Figure 4.2. Summary data for Ca^{2+} transient peak amplitude and T_{50} in myocytes from LV (red column) and RV (blue column) paced at 1 Hz. Data points are mean ± S.E.M. ***$P < 0.05$*** **compared to LV myocytes.**

Next, I investigated the effect of ISO on Ca^{2+} transients; the traces for Ca^{2+} in myocytes treated with 1 $\mu mol \cdot L^{-1}$ ISO are shown in Figure 4.3 Each Ca^{2+} transient was increased in response to ISO and the change in the ratio of Ca^{2+} transients was more pronounced in RV than in LV myocytes. Interestingly, the diastolic Ca^{2+} transients were decreased by ISO, which is consistent with the data provided in section 3.2.

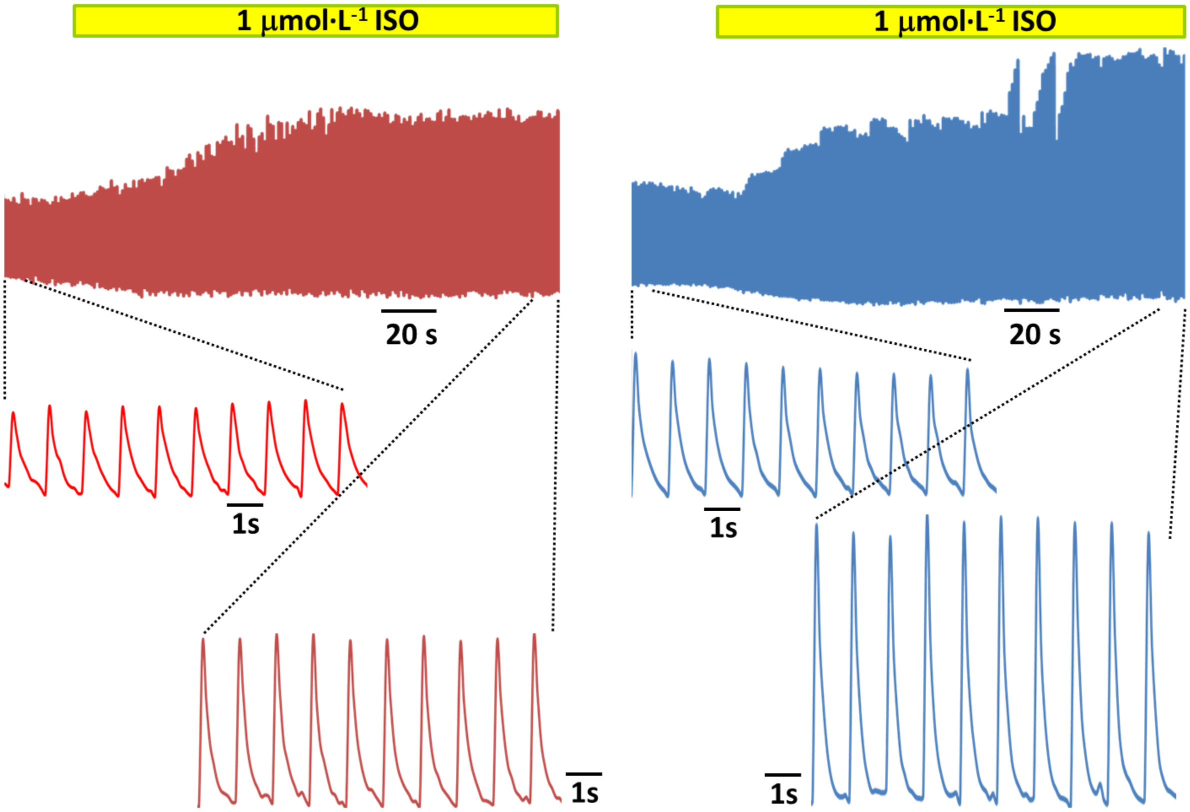

Figure 4.3. Typical developed Ca^{2+} transients in response to ISO. Representative raw Ca^{2+} transient signals recorded from an LV (red trace) and an RV (blue trace) myocytes.

A comparison of the relative increase in the ratio of Ca^{2+} transients in response to ISO with the control ratio (without ISO) at 1 Hz is shown in Figure 4.4. The average relative peak ratio of Ca^{2+} transients between the LV (1.71 ± 0.1, n = 6) and RV (2.24 ± 0.19, n = 6, $P < 0.05$ versus LV) myocytes was significantly different, which could be due to delayed decay kinetics of the Ca^{2+} transient in RV compared to LV myocytes. The increase of peak and delayed decay of Ca^{2+} transients in RV myocytes is consistent with the profoundly increased stress development in RV trabeculae by ISO as shown by the results provided in Chapter 3.

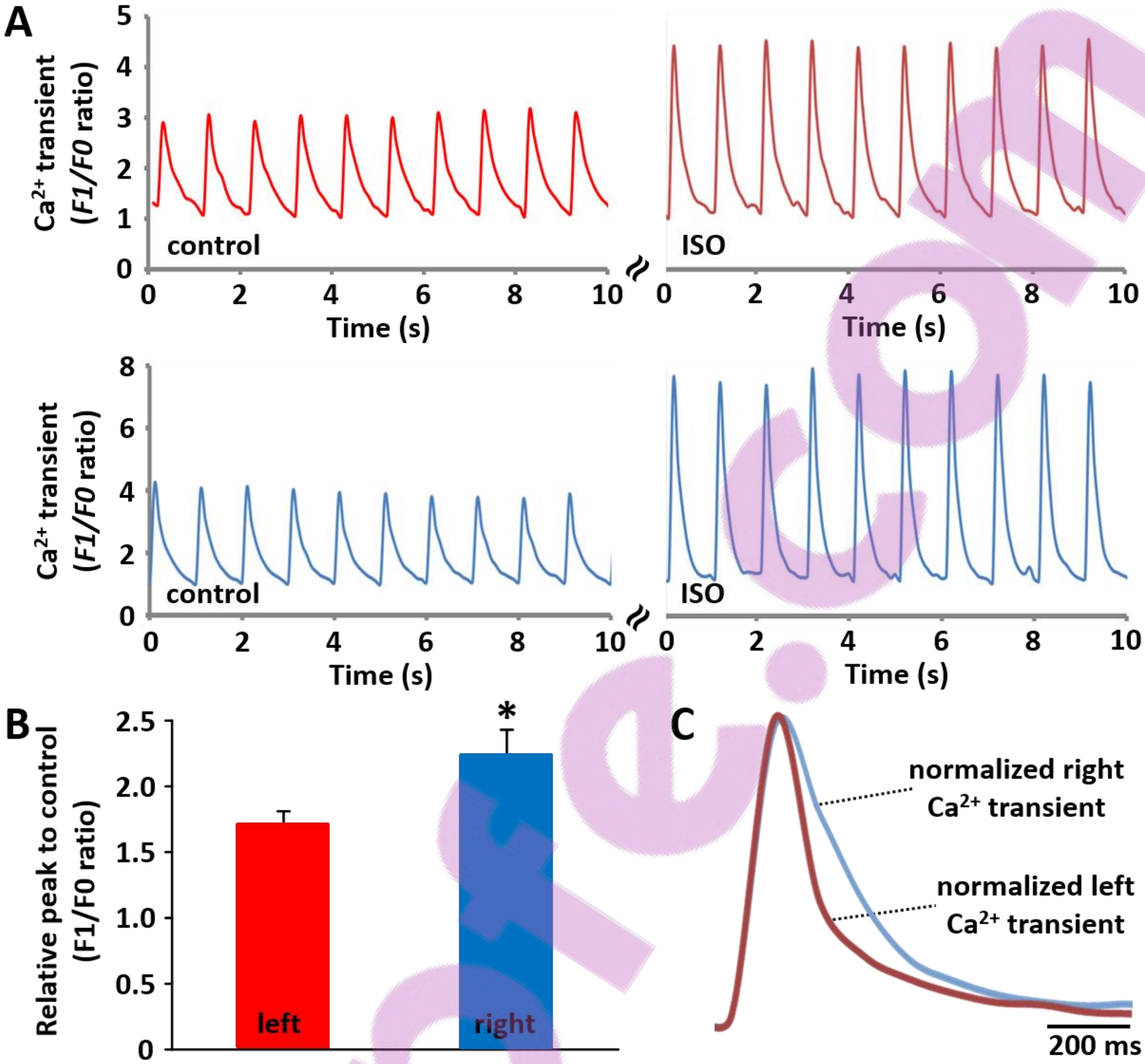

Figure 4.4. Summary of Ca^{2+} transient peak amplitude after treatment with ISO. (A) Representative traces of Ca^{2+} transients following treatment with ISO in myocytes from LV (red line) and RV (blue line) paced at 1 Hz. (B) Summary data for relative Ca^{2+} transient peak amplitude after treatment with ISO in myocytes from LV and RV paced at 1 Hz. Data points are mean ± S.E.M. *$P < 0.05$ compared to LV myocyte. (C) The overlapping traces in the lower panel show the normalized traces after treatment with ISO.

4.2 Discussion

AP morphology and duration are typically associated with the Ca^{2+} transient. I have examined the mechanism possibly responsible for the observations of different stresses between LV and RV muscles.

As shown in Figure 4.1 and 4.2, the decay of the Ca^{2+} transient is faster in the RV myocyte than in the LV myocyte, which could reflect more rapid uptake of $[Ca^{2+}]_i$ after contraction. Compared with the RV myocyte, the LV myocyte releases more Ca^{2+} from the SR via slower decay kinetics of the Ca^{2+} transient rather than increasing peak amplitude. This finding corresponds to other studies of the Ca^{2+} transients in normal RV and LV myocytes (Janssen et al., 2003). These authors also showed that alteration of the Ca^{2+} transient is associated with contractile dysfunction of the LV in spontaneous hypertensive heart failure.

It has been well-known that increasing the Ca^{2+} entry *via* the I_{LCC} increases the amplitude of Ca^{2+} transient and the force of contraction in the heart (Bers, 2002; Cannell et al., 1987). The amplitude of Ca^{2+} transient depends on I_{LCC} and the SR Ca^{2+} content (Dibb et al., 2007), while the decay of the Ca^{2+} transient depends on activities of NCX and SERCA (Trafford et al., 2001).

Changes in SR sequestration by SERCA can account for a fraction of the increased or decreased Ca^{2+} transient amplitude associated with the changes in AP duration that have been observed in many other studies (Bers, 2000, 2002). Therefore, the different decay of Ca^{2+} transient between the LV and the RV is also supposed to be the different kinetics of SERCA. There are evidences that the maximal velocity (V_{max}) and dissociation constants (K_d) in RV SR Ca^{2+} uptake were lower and higher than those in the LV, respectively, which could reflect functional differences between the LV and the RV (Afzal and Dhalla, 1992; Dhalla et al., 1980). On the other hand, an increase of SERCA activity would be expected to increase SR Ca^{2+} content and thereby increase cardiac contractility based on the observation that the amplitude of the systolic Ca^{2+} transient is a linear function of SERCA activity (Bode et al., 2011).

The findings of previous studies, together with my results, indicate that the Ca^{2+} transient in LV myocytes results in a larger total amount of $[Ca^{2+}]_i$, suggesting more contractile force. Other studies also showed that, at the cellular level, maximal sarcomere shortening by smaller Ca^{2+} transients in RV myocytes was significantly less than in LV myocytes, while the diastolic sarcomere length of RV myocytes was not different to that of LV myocytes (Chu et al., 2013; Kondo et al., 2006). The differences in intracellular Ca^{2+} transients between RV and LV myocytes suggest that Ca^{2+} dynamics may play an important role in the mechanical differences in these tissues.

I used Ca^{2+} transient analysis with ISO to further examine possible mechanisms underlying the different stresses observed between LV and RV muscles. When myocytes were treated with ISO, the increments in $[Ca^{2+}]_i$ were approximately 170% and 220% in LV and RV myocytes, respectively. This is the mechanism underlying the augmented response of right trabeculae to β-adrenergic agonists (Figure 3.9). These results are supported by other study that canine RV and LV differ in their β-AR response due to distinct compartmentalized cAMP signals in myocyte β-AR downstream signaling (Molina et al., 2014). β-adrenergic stimulation has been shown to drive the faster acceleration of the Ca^{2+} transient decline due to Ser16 phosphorylation and the faster Ca^{2+} transient time to peak due to CaMKII activation (Roof et al., 2011). The bulk of the Ca^{2+} released for contraction is thought to originate from the SR (Bers, 2000; Taylor et al., 2004). The Ca^{2+} release via RYR from the SR is quantal and directly related to the activity of the LCC (Santana et al., 1996; Taylor et al., 2004). In fact, when the cell repolarizes during the AP, this long-lasting Ca^{2+} influx by LCC in cardiomyocytes would maintain a more prominent plateau in the AP (Kim et al., 2010). Therefore, the increased amount of Ca^{2+} may result from an increase in the amount of ''trigger'' Ca^{2+} supplied by the LCC depending on the range of window current during AP. This remains to be proven and is the subject of current investigation.

In agreement with published data on the effect of ISO on the heart, ISO increased Ca^{2+} transient in LV and RV myocytes. Interestingly, enhancement of the peak, and lengthening of the decline, of the Ca^{2+} transient in RV myocyte suggest that ISO may enhance the phosphorylation of SERCA and increase SERCA pumping of cytosolic Ca^{2+} into the SR, resulting in depressed systolic force.

Here it should be pointed out that other ion channels also can alter AP duration and modulate the Ca^{2+} transient and corresponding contraction: AP waveforms in ventricle has been shown to be dependent on transient outward K^+ current density in rodent (Clark et al., 1993; Kondo et al., 2006) as well as in dog (Di Diego et al., 1996). Therefore, K^+ current might play an important role in different Ca^{2+} transient between the LV and the RV, which remains to be revealed.

Chapter 5

Biophysical Whole Cell Modelling

Mathematical modelling gives us useful ways to understand biological processes or to verify hypotheses by combining individual experimental results. The experiments in Chapter 4 were performed in order to find a possible underlying mechanism for the results obtained in Chapter 3, and biophysical whole cell modelling in this chapter is aimed to confirm the contribution of Ca^{2+} handling to the cellular mechanism for the development of stress in cardiac tissue. This cell model also has the advantage of validation via experimental results obtained directly at the cellular level.

The biophysical whole cell model was developed from model modules that were constructed using the architectural principles of CellML models. The components of three separate models of cardiomyocyte function (electrophysiology, calcium dynamics and mechanics) were disassembled as each module and validated separately, and then necessary parts were combined into a new integrative model of rat ventricular myocyte. The model was implemented in OpenCOR using the Physiome project CellML standard in order to ensure reproducibility.

5.1 Development of Whole Cell Model

Lots of biophysical cellular models have been developed and many frameworks for simulation have been suggested so far. Most researchers wish to share existing models and extend them to ensemble large scale models that address whole-cell level complexity. As one needs to develop a complex model in an efficient fashion, many kinds of simulation tools have been developed. Among them, CellML, a modelling language, has a couple of strengths: (1) it uses MathML to represent the mathematics of a model in a manner which is both human- and computer-readable; (2) it allows modular construction of models via component instances and encapsulation hierarchies, which provides model expandability as well as model reuse capability.

More specifically, in this study, I made component models of individual currents and validate separately each modules to test operability as independent working model.

The components of the existing three separate models of electrophysiology, calcium dynamics and mechanics in rat heart were disassembled and then made into individual working modules. These modules were implemented as CellML components which encompass variables and mathematics, and were validated separately. In turn validated modules were combined into a new integrative model of rat ventricular myocyte in OpenCOR, which was validated against the experimental data.

5.1.1 Structure of Model

The cell membrane was modelled as an electrical equivalent circuit with capacitor, variable resistances and voltage sources representing the different ion channels, pumps, and exchangers in adult rat myocytes. This circuit was coupled with a fluid compartment, which describes the changes in Na^+, K^+, and Ca^{2+} ions in the cytosol as well as the Ca^{2+} dynamics in dyadic space. The whole cell model in this study is integrated from the imported components shown in the schematic diagrams of Figure 5. 1.

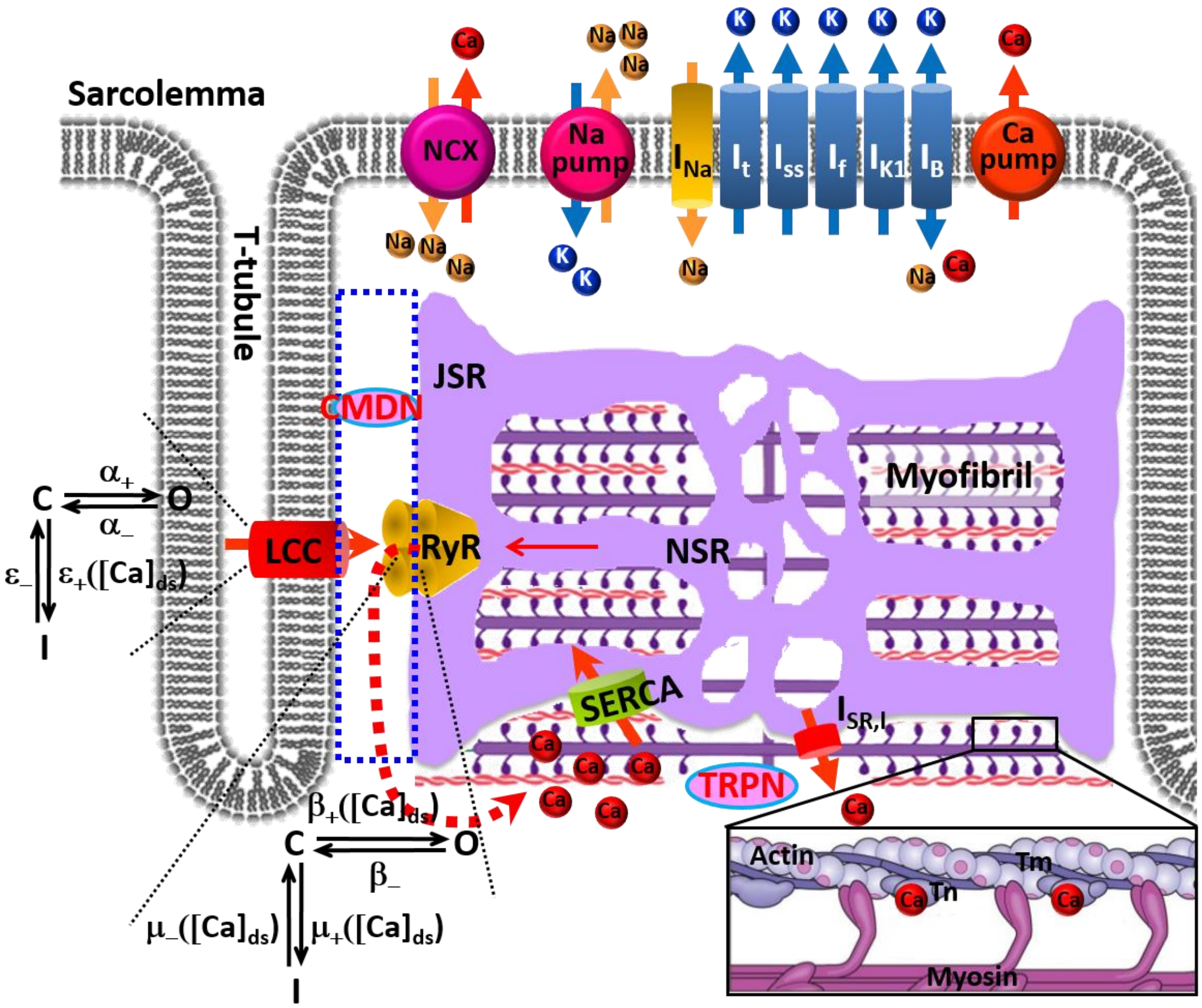

Figure 5.1. Schematic diagram of the currents, ion exchanges, and contractile proteins described by the present study. Insertions show the three-state model of the LCC and the RYR, which are explained in section 5.2.2.9. CMDN: calmodulin, TRPN: troponin, JSR: junctional sarcoplasmic reticulum, NSR: network sarcoplasmic reticulum.

Individual components are available online (https://models.physiomeproject.org/workspace/25c): INa_Pandit, Ito_Pandit, Iss_Pandit, IK1_Pandit, If_Pandit, IBNa_Pandit, IBK_Pandit, INaK_Pandit, CaRU_Hinch, ICaPump_Hinch, INCX_Hinch, IBCa_Hinch, ISRCaLeak_Hinch, ISERCA_Hinch, Icalmodulin_Hinch, Itroponin_NSH, Itropomyosin_NSH, CrossBridge_NSH.

Most of mathematical formulations were abstracted from those of Pandit *et al*. model (2001), Hinch *et al*. model (2004), and Niederer *et al*. model (2006) and parameters and variables were adjusted to the experimental values. I used base physical quantities defined by the *Système Internationl d'Unités* (SI): length (meter or m), time (second or s), amount of substance (mole), temperature (K), current (amp or A). All derived units that CellML defines intrinsically are: Hz (s^{-1}); Newton, N ($kg \cdot m \cdot s^{-2}$); Joule, J ($N \cdot m$); Pascal, Pa ($N \cdot m^{-2}$); Volt, V ($W \cdot A^{-1}$); Siemen, S ($A \cdot V^{-1}$); Ohm, Ω ($V \cdot A^{-1}$); Coulomb, C ($s \cdot A$); and Farad, F ($C \cdot V^{-1}$). All units for this model are illustrated in the following CellML text code:

```
def model unit_for_model as
    def unit millisec as
        unit second {pref: milli};
    enddef;

    def unit per_millisec as
        unit millisec {expo: -1};
    enddef;

    def unit millivolt as
        unit volt {pref: milli};
    enddef;

    def unit per_millivolt as
        unit millivolt {expo: -1};
    enddef;

    def unit millijoule_per_mole_kelvin as
        unit joule {pref: milli};
        unit kelvin {expo: -1};
        unit mole {expo: -1};
    enddef;

    def unit coulomb_per_mole as
        unit coulomb;
        unit mole {expo: -1};
    enddef;

    def unit microA as
        unit ampere {pref: micro};
    enddef;

    def unit milliS as
        unit siemens {pref: milli};
    enddef;

    def unit per_millivolt_millisec as
        unit per_millivolt;
        unit per_millisec;
    enddef;

    def unit milliS_per_millisec as
        unit siemens {pref: milli};
        unit per_millisec;
    enddef;

    def unit mM as
        unit mole {pref: milli};
        unit litre {expo: -1};
    enddef;

    def unit mM_per_millisec as
        unit mM;
        unit per_millisec;
    enddef;

    def unit mM_per_millivolt_millisec as
        unit mM;
        unit per_millivolt_millisec;
    enddef;

    def unit microL as
        unit litre {pref: micro};
    enddef;

    def unit per_mM as
        unit mM {expo: -1};
    enddef;

    def unit per_mM_millisec as
        unit per_mM;
        unit per_millisec;
    enddef;

    def unit per_millisec3 as
        unit millisec {expo: -3};
    enddef;

    def unit microm2 as
        unit meter {pref: micro, expo: 2};
    enddef;

    def unit microm3 as
        unit meter {pref: micro, expo: 3};
    enddef;

    def unit microm3_per_millisec as
        unit microm3;
        unit per_millisec;
    enddef;

    def unit microm3_mM_per_millisec as
        unit microm3;
        unit mM;
        unit per_millisec;
    enddef;

    def unit N_per_mm2 as
        unit newton;
        unit metre {pref: milli, expo: -2};
    enddef;

    def unit microF as
        unit farad {pref: micro};
    enddef;
enddef;
```

The cell was assumed to be a cylinder; compartment volumes and physical constants are described Table 5.1.

Table 5.1 Cell geometry and physical constant parameter

Parameter	Definition	Value	Reference
F	Faraday's constant	96.487 kC·mol^{-1}	
T	Temperature	295 K	
R	Universal gas constant	8.3145 J·mol^{-1}·K^{-1}	
V_{myo}	Volume of myoplasm	25.85 pL	(1)
V_{SR}	Volume of sarcoplasmic reticulum	2.098 pL	(1)
V_{ds}	Volume of dyadic space	20 pL	(2)
N	Number of release units	50000	(2)
Cm	Total membrane capacitance	100 pF	(1)

The cell was assumed to be a cylinder; values for compartment volumes and physical constants were lifted from (1), (2), or (3), and are shown in Table A.1. Values from (1), (Bondarenko et al., 2004) or (2), (Greenstein and Winslow, 2002), (3), (Hinch et al., 2004)

The electrophysiological behaviour was described with the following ordinary differential equation:

$$\frac{dV}{dt} = -\frac{I_{ion} + I_{stim}}{C_m} \qquad \text{Eq 5-1}$$

where V is voltage, t is time, I_{ion} is the sum of all transmembrane ionic currents, I_{stim} is the externally applied stimulus current, and C_m is cell capacitance per unit surface area. The equations used in the model are formulated briefly in the following sections and provided in the Appendix A. All parameters of the model are listed in Appendix A (table A.1 – A.4).

5.1.2 Formulation and Validation of the Individual Model Modules

5.1.2.1 Na$^+$ current (I_{Na}) module

The formulation of the Na$^+$ channel current (I_{Na}) model is from the Pandit et al. model (2001). The original formulations of three gates for I_{Na} were first introduced by Beeler and Reuter (1997):

$$I_{Na} = g_{Na}m^3hj(V - E_{Na}) \qquad \text{Eq 5-2, A.3.1.}$$

where g_{Na} is the maximum conductance of the Na$^+$ channel, *m* is an activation gate, *h* is a fast inactivation gate, *j* is a slow inactivation gate, and E_{Na} is the equilibrium potential for the Na$^+$ channel. The formulation of the equilibrium potential for the Na$^+$ channel is from the Nernst equation:

$$E_{Na} = \frac{RT}{zF} ln \frac{[Na^+]_o}{[Na^+]_i} \qquad \text{Eq 5-3, A.2.1.}$$

where *R* is the ideal gas constant, *T* is the temperature, *z* is the number of moles of electrons, and *F* is the Faraday's constant.

The kinetic properties of I_{Na} were reported to be similar across different species, which gives us a rationale to use these variables: the steady-state activation and inactivation curves and the normalized peak current-voltage (*I*-*V*) relationship are based on experimental results and the maximum Na$^+$ conductance (g_{Na}) was adjusted in the rat (Lee et al., 1999); The time constants for activation (τ_m) and inactivation (τ_h, τ_j) used as model parameters were adapted from the cell model of guinea pig ventricle (Luo and Rudy, 1994) and scaled.

In one fixed condition with $[Na^+]_o$ = 145 mmol·L^{-1} and $[Na^+]_i$ = 11.28 mmol·L^{-1}, the current traces and parameters of I_{Na} corresponded well with published results (Figure 5.3).

The CellML text code for I_{Na} model is as follows:

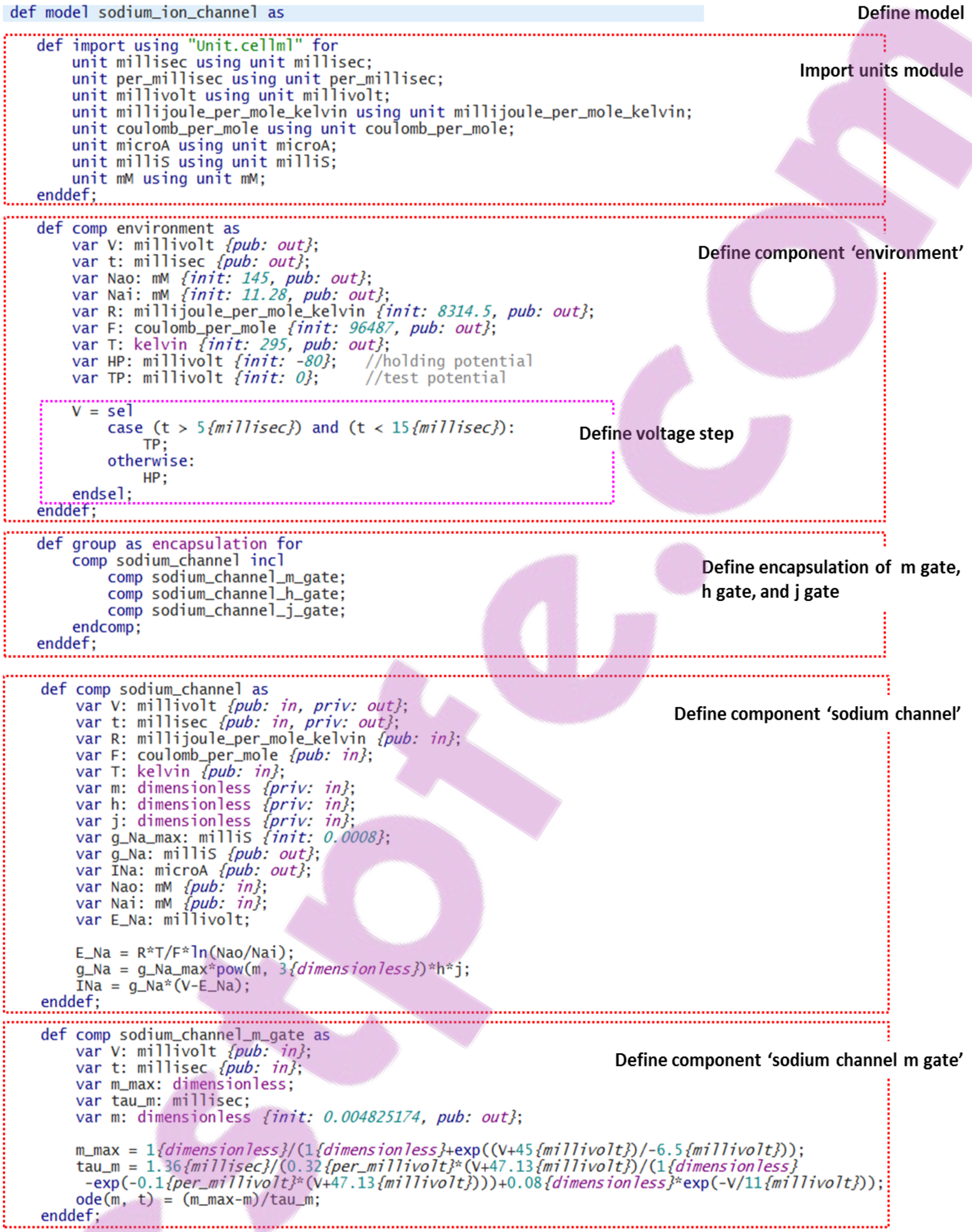

```
def model sodium_ion_channel as
    def import using "Unit.cellml" for
        unit millisec using unit millisec;
        unit per_millisec using unit per_millisec;
        unit millivolt using unit millivolt;
        unit millijoule_per_mole_kelvin using unit millijoule_per_mole_kelvin;
        unit coulomb_per_mole using unit coulomb_per_mole;
        unit microA using unit microA;
        unit milliS using unit milliS;
        unit mM using unit mM;
    enddef;
    def comp environment as
        var V: millivolt {pub: out};
        var t: millisec {pub: out};
        var Nao: mM {init: 145, pub: out};
        var Nai: mM {init: 11.28, pub: out};
        var R: millijoule_per_mole_kelvin {init: 8314.5, pub: out};
        var F: coulomb_per_mole {init: 96487, pub: out};
        var T: kelvin {init: 295, pub: out};
        var HP: millivolt {init: -80};    //holding potential
        var TP: millivolt {init: 0};      //test potential

        V = sel
            case (t > 5{millisec}) and (t < 15{millisec}):
                TP;
            otherwise:
                HP;
        endsel;
    enddef;
    def group as encapsulation for
        comp sodium_channel incl
            comp sodium_channel_m_gate;
            comp sodium_channel_h_gate;
            comp sodium_channel_j_gate;
        endcomp;
    enddef;
    def comp sodium_channel as
        var V: millivolt {pub: in, priv: out};
        var t: millisec {pub: in, priv: out};
        var R: millijoule_per_mole_kelvin {pub: in};
        var F: coulomb_per_mole {pub: in};
        var T: kelvin {pub: in};
        var m: dimensionless {priv: in};
        var h: dimensionless {priv: in};
        var j: dimensionless {priv: in};
        var g_Na_max: milliS {init: 0.0008};
        var g_Na: milliS {pub: out};
        var INa: microA {pub: out};
        var Nao: mM {pub: in};
        var Nai: mM {pub: in};
        var E_Na: millivolt;

        E_Na = R*T/F*ln(Nao/Nai);
        g_Na = g_Na_max*pow(m, 3{dimensionless})*h*j;
        INa = g_Na*(V-E_Na);
    enddef;
    def comp sodium_channel_m_gate as
        var V: millivolt {pub: in};
        var t: millisec {pub: in};
        var m_max: dimensionless;
        var tau_m: millisec;
        var m: dimensionless {init: 0.004825174, pub: out};

        m_max = 1{dimensionless}/(1{dimensionless}+exp((V+45{millivolt})/-6.5{millivolt}));
        tau_m = 1.36{millisec}/(0.32{per_millivolt}*(V+47.13{millivolt})/(1{dimensionless}
         -exp(-0.1{per_millivolt}*(V+47.13{millivolt})))+0.08{dimensionless}*exp(-V/11{millivolt}));
        ode(m, t) = (m_max-m)/tau_m;
    enddef;
```

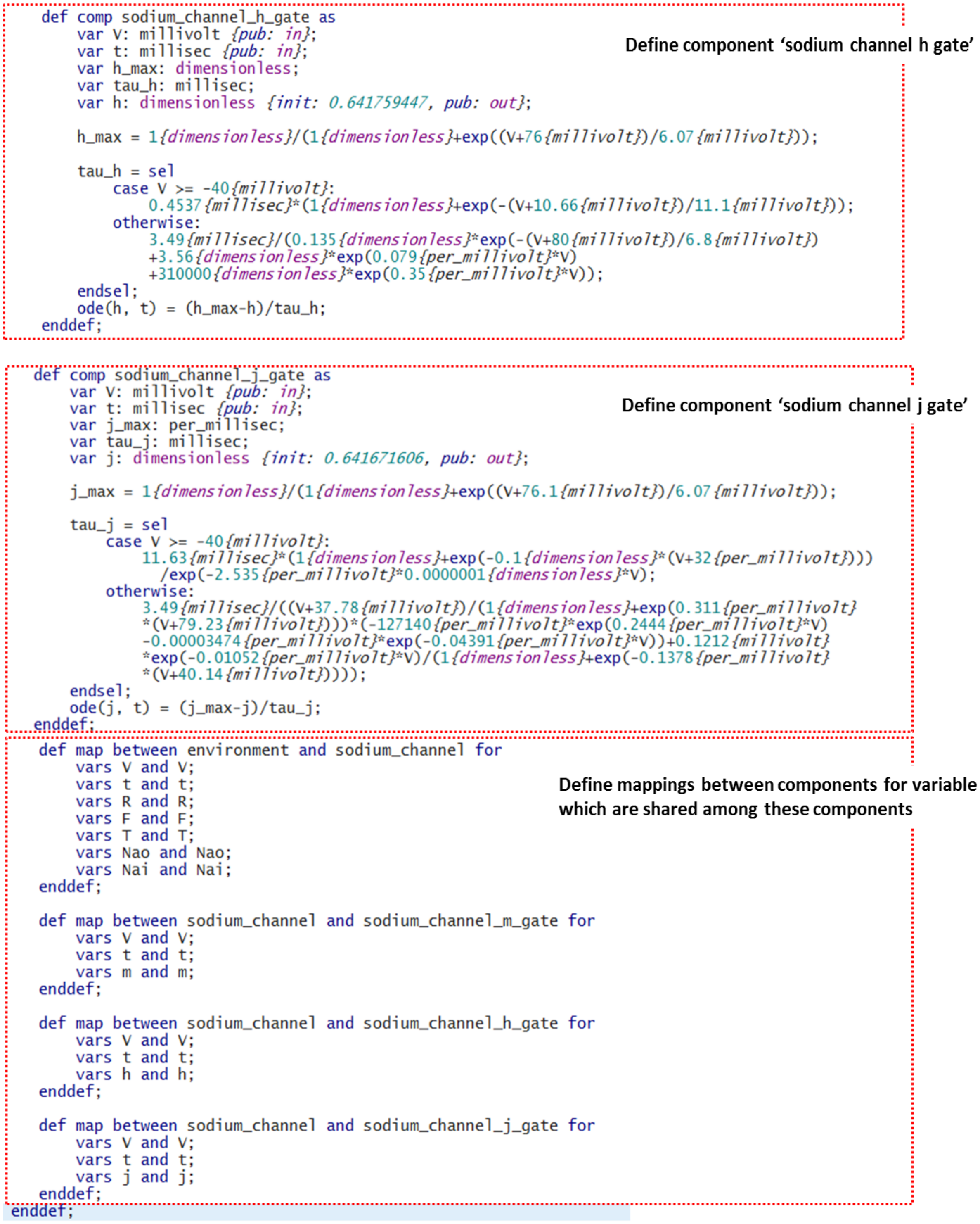

Define component ‘sodium channel h gate’

```
    def comp sodium_channel_h_gate as
        var V: millivolt {pub: in};
        var t: millisec {pub: in};
        var h_max: dimensionless;
        var tau_h: millisec;
        var h: dimensionless {init: 0.641759447, pub: out};

        h_max = 1{dimensionless}/(1{dimensionless}+exp((V+76{millivolt})/6.07{millivolt}));

        tau_h = sel
            case V >= -40{millivolt}:
                0.4537{millisec}*(1{dimensionless}+exp(-(V+10.66{millivolt})/11.1{millivolt}));
            otherwise:
                3.49{millisec}/(0.135{dimensionless}*exp(-(V+80{millivolt})/6.8{millivolt})
                +3.56{dimensionless}*exp(0.079{per_millivolt}*V)
                +310000{dimensionless}*exp(0.35{per_millivolt}*V));
        endsel;
        ode(h, t) = (h_max-h)/tau_h;
    enddef;
```

Define component ‘sodium channel j gate’

```
    def comp sodium_channel_j_gate as
        var V: millivolt {pub: in};
        var t: millisec {pub: in};
        var j_max: per_millisec;
        var tau_j: millisec;
        var j: dimensionless {init: 0.641671606, pub: out};

        j_max = 1{dimensionless}/(1{dimensionless}+exp((V+76.1{millivolt})/6.07{millivolt}));

        tau_j = sel
            case V >= -40{millivolt}:
                11.63{millisec}*(1{dimensionless}+exp(-0.1{dimensionless}*(V+32{per_millivolt})))
                  /exp(-2.535{per_millivolt}*0.0000001{dimensionless}*V);
            otherwise:
                3.49{millisec}/((V+37.78{millivolt})/(1{dimensionless}+exp(0.311{per_millivolt}
                *(V+79.23{millivolt})))*(-127140{per_millivolt}*exp(0.2444{per_millivolt}*V)
                -0.00003474{per_millivolt}*exp(-0.04391{per_millivolt}*V))+0.1212{millivolt}
                *exp(-0.01052{per_millivolt}*V)/(1{dimensionless}+exp(-0.1378{per_millivolt}
                *(V+40.14{millivolt}))));
        endsel;
        ode(j, t) = (j_max-j)/tau_j;
    enddef;
```

Define mappings between components for variable which are shared among these components

```
    def map between environment and sodium_channel for
        vars V and V;
        vars t and t;
        vars R and R;
        vars F and F;
        vars T and T;
        vars Nao and Nao;
        vars Nai and Nai;
    enddef;

    def map between sodium_channel and sodium_channel_m_gate for
        vars V and V;
        vars t and t;
        vars m and m;
    enddef;

    def map between sodium_channel and sodium_channel_h_gate for
        vars V and V;
        vars t and t;
        vars h and h;
    enddef;

    def map between sodium_channel and sodium_channel_j_gate for
        vars V and V;
        vars t and t;
        vars j and j;
    enddef;
enddef;
```

Note that several features have been addressed above: I defined components (i) the environment, (ii) the Na⁺ channel conductivity, and (iii) the dynamics of the m-, h-, and j-gate; I also defined the component maps as certain variables (V, t, R, F, T, Nao, Nai, m, h, and j) are shared between components; I added the event control select case which indicates that the voltage is specified to jump from -80 mV to 0 mV (or others) at t = 5 ms then back to -80 mV at t = 15 ms for testing the Na$^+$ channel model; I used encapsulation to embed the sodium_channel_m_gate, h_gate, and j_gate inside the sodium_channel.

Then I used OpenCOR, with Ending point 40 and Point interval 0.1, to solve the equations for the Na$^+$ channel under several voltage step conditions, the results are shown in Figure 5.2 with plots of *V(t), m(t), h(t), j(t),* $g_{Na}(t)$ and $i_{Na}(t)$ for voltage steps from (a) -80 mV to -40 mV, (b) -80 mV to -20 mV, (c) -80 mV to 0 mV and (d) -80 mV to 20 mV.

(a)

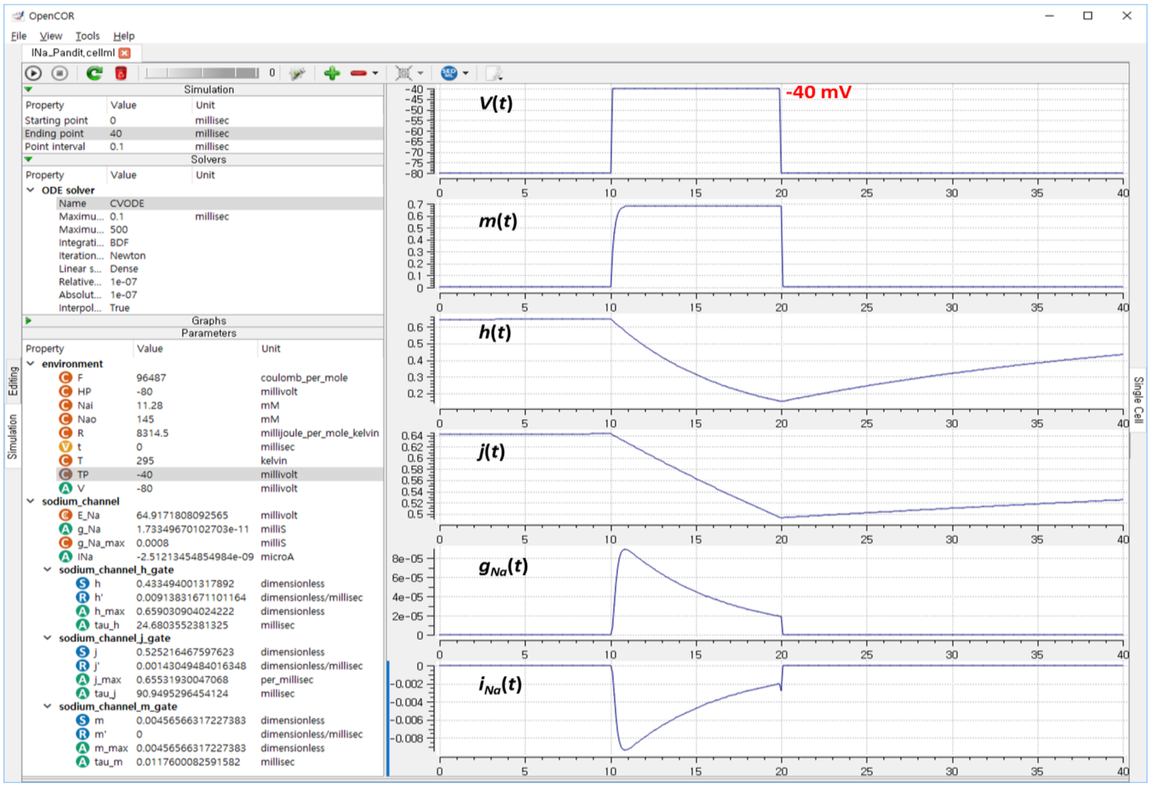

Simulation

Property	Value	Unit
Starting point	0	millisec
Ending point	40	millisec
Point interval	0.1	millisec

Solvers

Property	Value	Unit
ODE solver		
Name	CVODE	
Maximu...	0.1	millisec
Maximu...	500	
Integrati...	BDF	
Iteration...	Newton	
Linear s...	Dense	
Relative...	1e-07	
Absolut...	1e-07	
Interpol...	True	

Graphs

Parameters

Property	Value	Unit
environment		
F	96487	coulomb_per_mole
HP	-80	millivolt
Nai	11.28	mM
Nao	145	mM
R	8314.5	millijoule_per_mole_kelvin
t	0	millisec
T	295	kelvin
TP	-40	millivolt
V	-80	millivolt
sodium_channel		
E_Na	64.9171808092565	millivolt
g_Na	1.73349670102703e-11	milliS
g_Na_max	0.0008	milliS
INa	-2.51213454854984e-09	microA
sodium_channel_h_gate		
h	0.433494001317892	dimensionless
h'	0.00913831671101164	dimensionless/millisec
h_max	0.659030904024222	dimensionless
tau_h	24.6803552381325	millisec
sodium_channel_j_gate		
j	0.525216467597623	dimensionless
j'	0.00143049484016348	dimensionless/millisec
j_max	0.65531930047068	per_millisec
tau_j	90.9495296454124	millisec
sodium_channel_m_gate		
m	0.00456566317227383	dimensionless
m'	0	dimensionless/millisec
m_max	0.00456566317227383	dimensionless
tau_m	0.0117600082591582	millisec

(b)

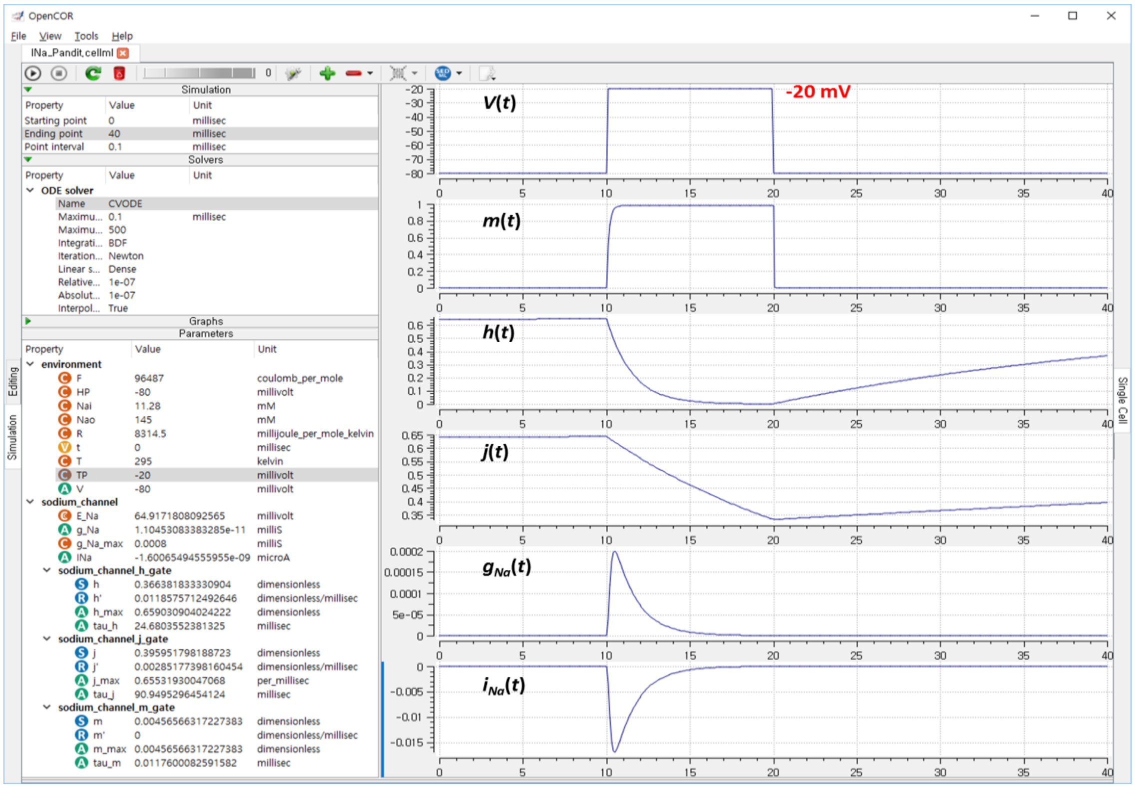

Simulation

Property	Value	Unit
Starting point	0	millisec
Ending point	40	millisec
Point interval	0.1	millisec

Solvers

Property	Value	Unit
ODE solver		
Name	CVODE	
Maximu...	0.1	millisec
Maximu...	500	
Integrati...	BDF	
Iteration...	Newton	
Linear s...	Dense	
Relative...	1e-07	
Absolut...	1e-07	
Interpol...	True	

Graphs

Parameters

Property	Value	Unit
environment		
Ⓒ F	96487	coulomb_per_mole
Ⓒ HP	-80	millivolt
Ⓒ Nai	11.28	mM
Ⓒ Nao	145	mM
Ⓒ R	8314.5	millijoule_per_mole_kelvin
Ⓥ t	0	millisec
Ⓒ T	295	kelvin
Ⓒ TP	-20	millivolt
Ⓐ V	-80	millivolt
sodium_channel		
Ⓒ E_Na	64.9171808092565	millivolt
Ⓐ g_Na	1.10453083383285e-11	milliS
Ⓒ g_Na_max	0.0008	milliS
Ⓐ INa	-1.60065494555955e-09	microA
sodium_channel_h_gate		
Ⓢ h	0.366381833330904	dimensionless
Ⓡ h'	0.0118575712492646	dimensionless/millisec
Ⓐ h_max	0.659030904024222	dimensionless
Ⓐ tau_h	24.6803552381325	millisec
sodium_channel_j_gate		
Ⓢ j	0.395951798188723	dimensionless
Ⓡ j'	0.00285177398160454	dimensionless/millisec
Ⓐ j_max	0.65531930047068	per_millisec
Ⓐ tau_j	90.9495296454124	millisec
sodium_channel_m_gate		
Ⓢ m	0.00456566317227383	dimensionless
Ⓡ m'	0	dimensionless/millisec
Ⓐ m_max	0.00456566317227383	dimensionless
Ⓐ tau_m	0.0117600082591582	millisec

(c)

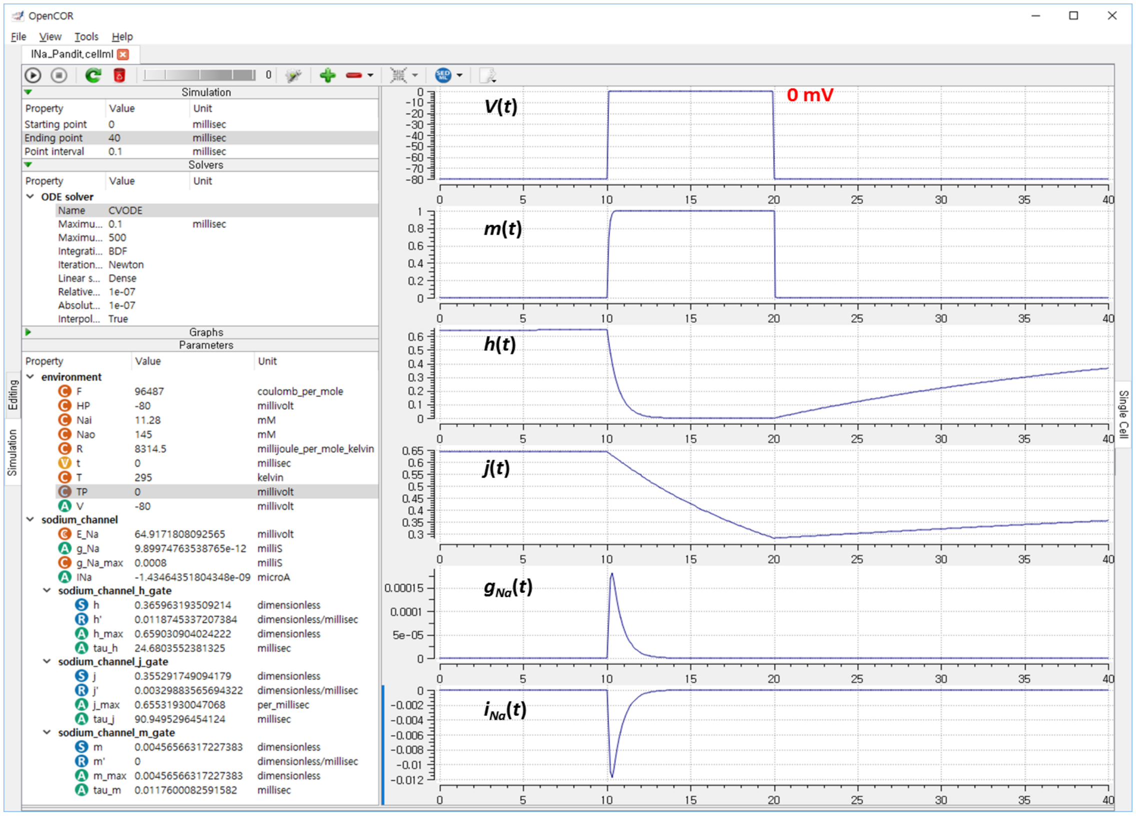

Simulation

Property	Value	Unit
Starting point	0	millisec
Ending point	40	millisec
Point interval	0.1	millisec

Solvers

Property	Value	Unit
ODE solver		
Name	CVODE	
Maximu...	0.1	millisec
Maximu...	500	
Integrati...	BDF	
Iteration...	Newton	
Linear s...	Dense	
Relative...	1e-07	
Absolut...	1e-07	
Interpol...	True	

Graphs

Parameters

Property	Value	Unit
environment		
Ⓒ F	96487	coulomb_per_mole
Ⓒ HP	-80	millivolt
Ⓒ Nai	11.28	mM
Ⓒ Nao	145	mM
Ⓒ R	8314.5	millijoule_per_mole_kelvin
Ⓥ t	0	millisec
Ⓒ T	295	kelvin
Ⓒ TP	0	millivolt
Ⓐ V	-80	millivolt
sodium_channel		
Ⓒ E_Na	64.9171808092565	millivolt
Ⓐ g_Na	9.89974763538765e-12	milliS
Ⓒ g_Na_max	0.0008	milliS
Ⓐ INa	-1.43464351804348e-09	microA
sodium_channel_h_gate		
Ⓢ h	0.365963193509214	dimensionless
Ⓡ h'	0.0118745337207384	dimensionless/millisec
Ⓐ h_max	0.659030904024222	dimensionless
Ⓐ tau_h	24.6803552381325	millisec
sodium_channel_j_gate		
Ⓢ j	0.355291749094179	dimensionless
Ⓡ j'	0.00329883565694322	dimensionless/millisec
Ⓐ j_max	0.65531930047068	per_millisec
Ⓐ tau_j	90.9495296454124	millisec
sodium_channel_m_gate		
Ⓢ m	0.00456566317227383	dimensionless
Ⓡ m'	0	dimensionless/millisec
Ⓐ m_max	0.00456566317227383	dimensionless
Ⓐ tau_m	0.0117600082591582	millisec

(d)

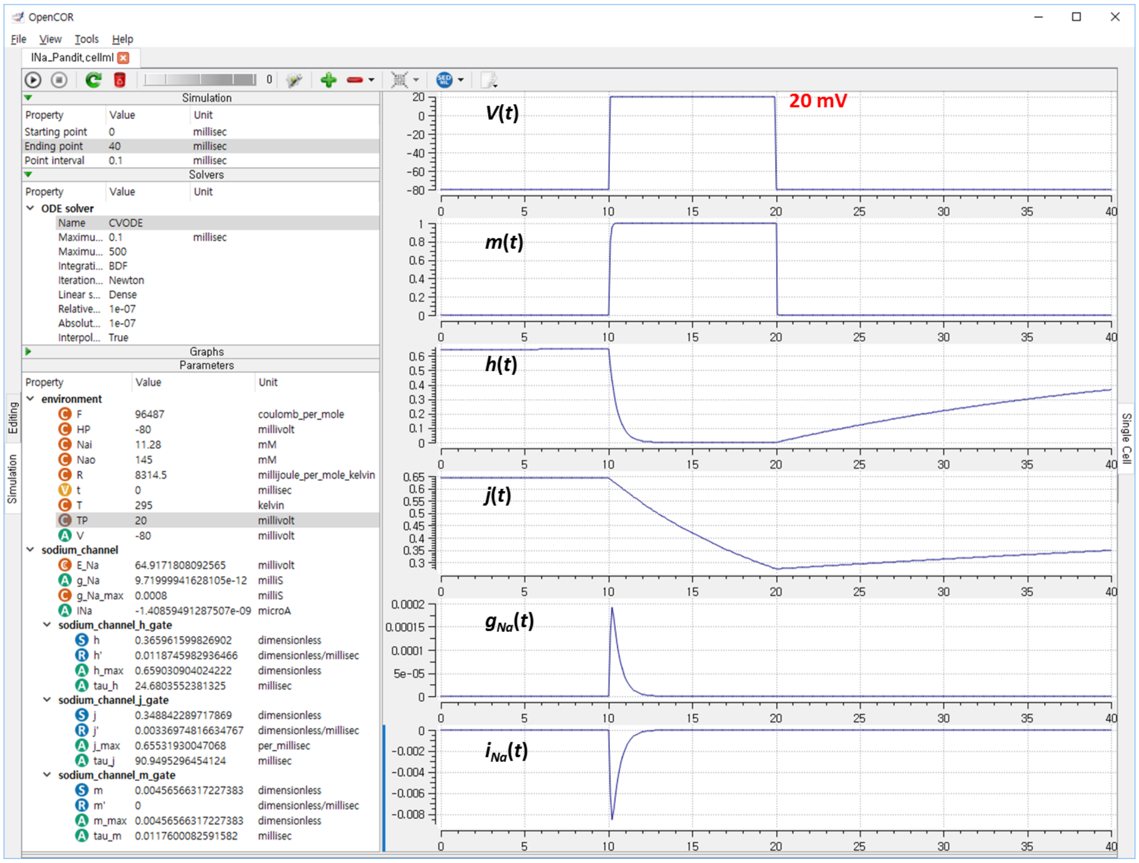

Simulation

Property	Value	Unit
Starting point	0	millisec
Ending point	40	millisec
Point interval	0.1	millisec

Solvers

Property	Value	Unit
ODE solver		
Name	CVODE	
Maximu...	0.1	millisec
Maximu...	500	
Integrati...	BDF	
Iteration...	Newton	
Linear s...	Dense	
Relative...	1e-07	
Absolut...	1e-07	
Interpol...	True	

Graphs

Parameters

Property	Value	Unit
environment		
C F	96487	coulomb_per_mole
C HP	-80	millivolt
C Nai	11.28	mM
C Nao	145	mM
C R	8314.5	millijoule_per_mole_kelvin
V t	0	millisec
C T	295	kelvin
C TP	20	millivolt
A V	-80	millivolt
sodium_channel		
C E_Na	64.9171808092565	millivolt
A g_Na	9.71999941628105e-12	milliS
C g_Na_max	0.0008	milliS
A INa	-1.40859491287507e-09	microA
sodium_channel_h_gate		
S h	0.365961599826902	dimensionless
R h'	0.0118745982936466	dimensionless/millisec
A h_max	0.659030904024222	dimensionless
A tau_h	24.6803552381325	millisec
sodium_channel_j_gate		
S j	0.348842289717869	dimensionless
R j'	0.00336974816634767	dimensionless/millisec
A j_max	0.65531930047068	per_millisec
A tau_j	90.9495296454124	millisec
sodium_channel_m_gate		
S m	0.00456566317227383	dimensionless
R m'	0	dimensionless/millisec
A m_max	0.00456566317227383	dimensionless
A tau_m	0.0117600082591582	millisec

Figure 5.2. Kinetics of the sodium channel gates for voltage steps to (a) -40 mV, (b) -20 mV, (c) 0 mV, and (d) 20 mV. The voltage clamp step is shown at the top, then the m gate first order response, then the h gate, then the j gate, then the channel conductance, then the channel current.

I obtained numerical values for all variables to save them as the comma-separated values (CSV) files and then plotted whole-cell current traces, the *I*-*V* relationship and time constants (Figure 5.3).

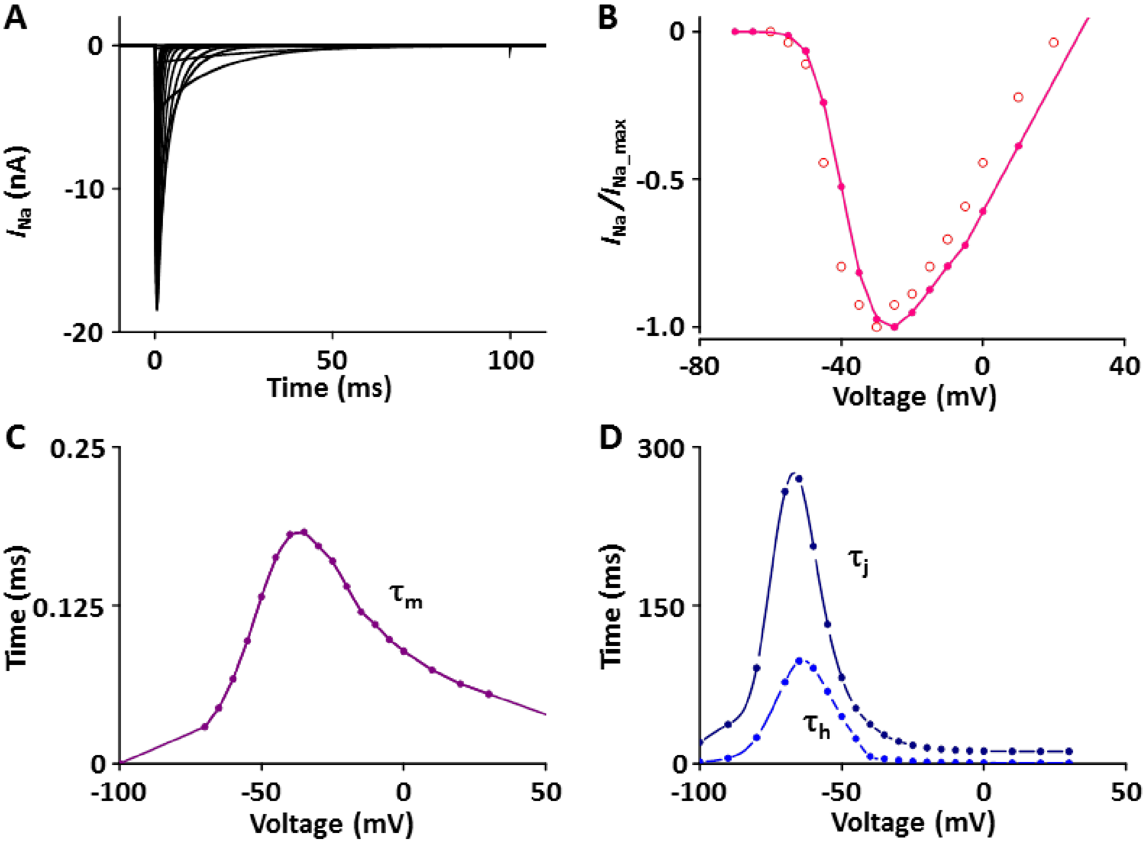

Figure 5.3. Verification of I_{Na} OpenCOR implementation. (A) Simulated current traces of the Na^+ channel. (B) Normalized simulated *I-V* relationship of I_{Na} (o represents experimental data from Lee et al., 1999). (C) Simulated activation time constant (τ_m) (D) Simulated inactivation time constants (τ_h, τ_j).

Each module was modeled in the same way and the values were compared with the experimental data or the results of the other studies.

5.1.2.2 Ca^{2+}-independent transient outward K^+ current (I_{to}) module

The formulation of the Ca^{2+}-independent transient outward K^+ current (I_{to}) model is from the Pandit et al. model (2001).

$$I_{to} = g_t r(as + bs_{slow})(V - E_K) \qquad \text{Eq 5-4, A.3.10.}$$

where g_t is the maximum conductance of the transient outward K^+ channel, E_K is the equilibrium potential for K^+, r is the activation gate, and s and s_{slow} are the fast and slow inactivation gates. The formulation of the equilibrium potential for the K^+ channel is from the Nernst equation:

$$E_K = \frac{RT}{zF} ln \frac{[K^+]_o}{[K^+]_i} \qquad \text{Eq 5-5, A.2.2.}$$

where R is the ideal gas constant, T is the temperature, z is the number of moles of electrons, and F is the Faraday's constant. These all values are based on individual experimental data in the rat heart: the steady-state activation and inactivation values from Stengl et al. study (1998); the time constant for activation from Angus et al. study (1991); the inactivation time constants from Wettwer et al. study (1993); and the recovery time constants from Volk et al. study (2001).

In one fixed condition with $[K^+]_o = 5.4$ mmol·L^{-1} and $[K^+]_i = 138.72$ mmol·L^{-1}, the current traces and parameters of I_{to} corresponded well to published results (Figure 5.4).

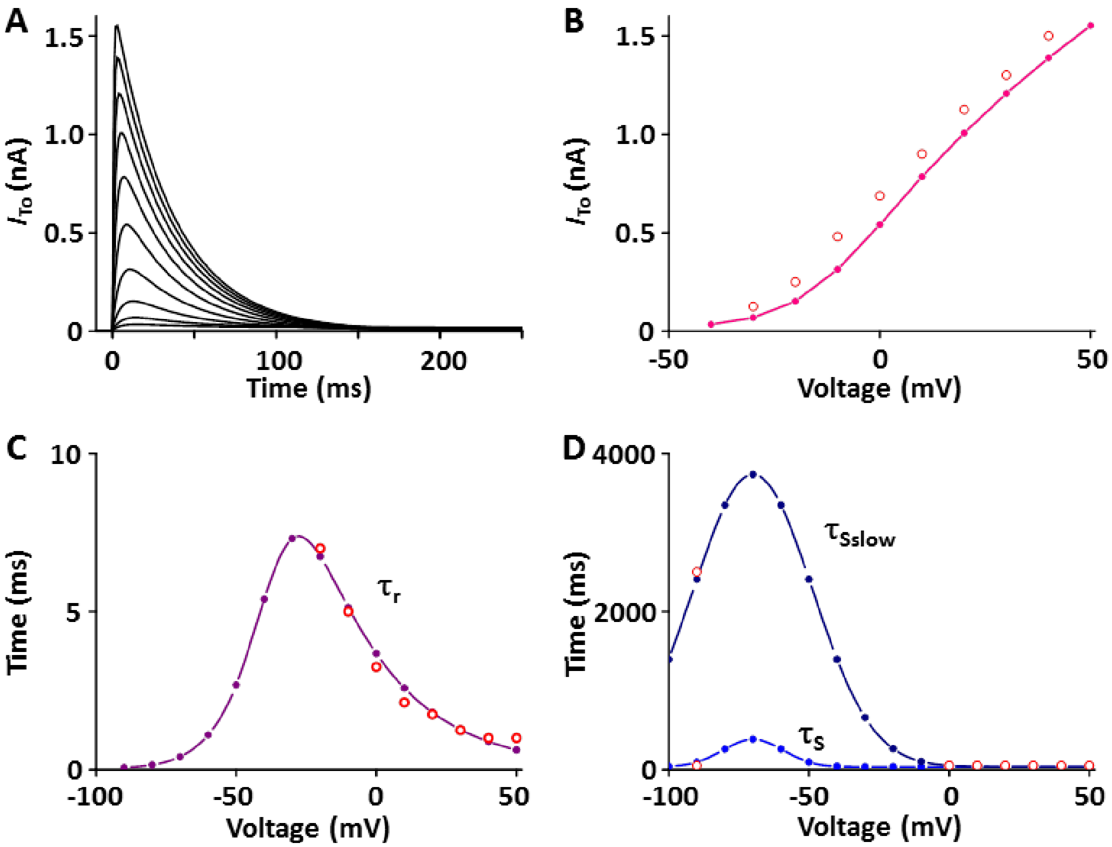

Figure 5.4. Verification of I_{to} OpenCOR implementation. (A) Simulated current traces of Ca^{2+}-independent transient outward K^{+} channel. (B) Simulated *I-V* relationship for I_{to} (pink line). This simulated result is in close agreement with representative experimental result (o, (Clark et al., 1995)). (C) Simulated activation time constant (τ_r, purple line). This simulated result is in close agreement with representative experimental result (o, (Agus et al., 1991)). (D) Simulated inactivation time constants (τ_S, τ_{Sslow}, blue lines). This simulated result is in close agreement with representative experimental result (o, (Wettwer et al., 1993)).

5.1.2.3 Steady-state outward K^+ current (I_{ss}) module

The formulation of the steady-state outward K^+ current (I_{ss}) model was based on the Pandit et al. model (2001).

$$I_{ss} = g_{ss} r_{ss} s_{ss} (V - E_K) \qquad \text{Eq 5-6, A.3.19}$$

where g_{ss} is the maximum conductance of the steady-state outward K channel, r_{ss} is the activation gate, s_{ss} is the inactivation gate, and E_K is the equilibrium potential for K^+. Note that this is the Pandit model approximation for I_{Kr}. These all values are based on individual experimental data in the rat heart: the steady-state activation and inactivation values from Weis et al. study (1993); the time constant for activation, which is 10 times slower than that of I_{to}, from Apkon and Nerbonne study (1991); the time constant for inactivation from Berger et al. study (1998).

In one fixed condition with $[K^+]_o = 5$ mmol·L^{-1} and $[K^+]_i = 140.45$ mmol·L^{-1}, the current traces and parameters of I_{ss} corresponded well with published results (Figure 5.5).

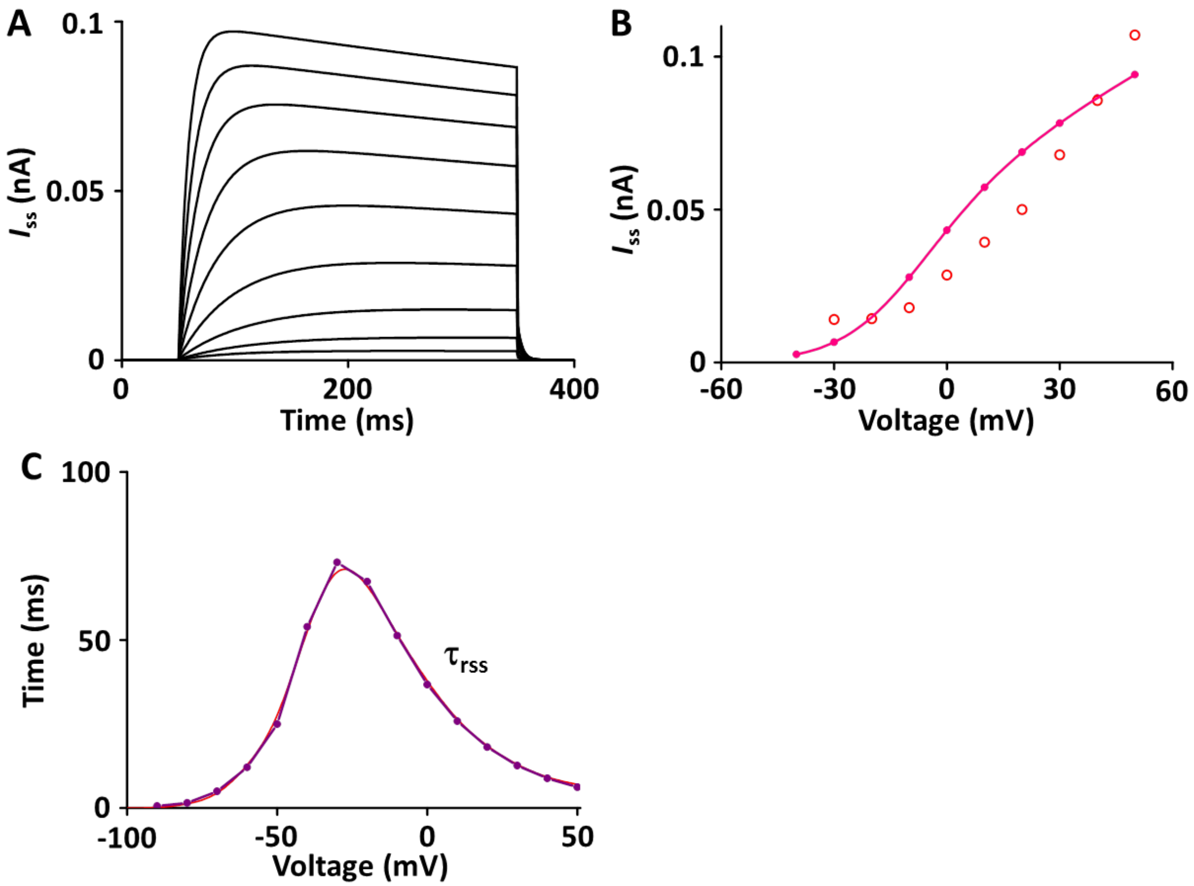

Figure 5.5. Verification of I_{ss} OpenCOR implementation. Values for I_{ss} were obtained at the end of a long (300 ms) depolarized voltage clamp pulse. (A) Simulated current traces of the steady-state outward K^+ channel. (B) Simulated *I-V* relationship of I_{ss} (pink line). This simulated result is in close agreement with representative experimental result (o, Clark et al. (1995)). (C) Simulated activation time constant (τ_{rss}, purple line). This simulated result is in close agreement with representative experimental result (red line, Apkon and Nerbonne (1991)), which is 10 times slower than the corresponding one for I_{to} (Figure 5.4C).

5.1.2.4 Inward rectifier K$^+$ current (I_{K1}) module

The inward rectifier K$^+$ current (I_{K1}) model is from the Pandit et al. (2001) model.

$$I_{K1} = \left[\frac{48}{e^{\frac{(V+37)}{25}} + e^{\frac{(V+37)}{-25}}} + 10\right] \cdot \left[\frac{0.001}{1 + e^{\frac{(V-E_K-76.77)}{-17}}}\right] + \frac{g_{K1}(V - E_K - 1.73)}{(1 + e^{1.613F(V-E_K-1.73)/RT}) \cdot (1 + e^{[K^+]_o - 0.9988/-0.124})}$$

Eq 5-7, A.3.25.

where g_{K1} is the maximum conductance of the inward rectifier K$^+$ channel, R is the ideal gas constant, T is the temperature, and E_K is the equilibrium potential for K$^+$.

To characterize different *I-V* relationship of I_{K1} depending on extracellular K$^+$ concentration ($[K^+]_o$), current traces and *I-V* relationship of I_{K1} were verified in condition with $[K^+]_o$ = 5.4 or 10 mmol·L^{-1}, which were corresponded well with published results (Figure 5.6).

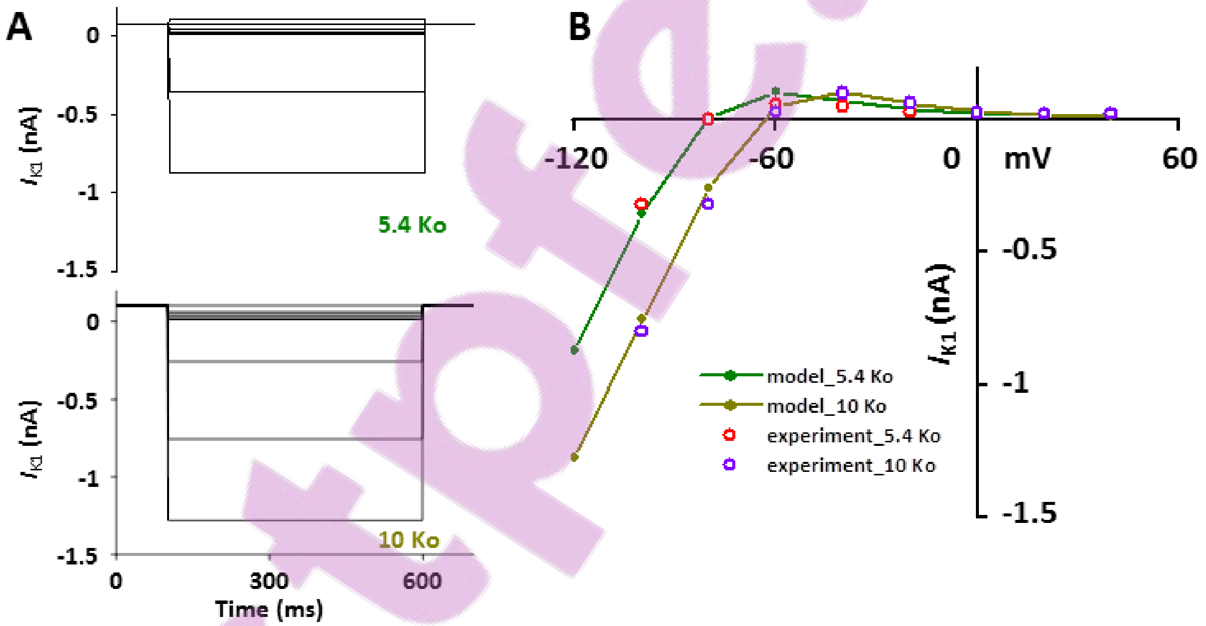

Figure 5.6. Verification of I_{K1} OpenCOR implementation. (A) Simulated current traces of the hyperpolarization-activated channel at extracellular K$^+$ ion concentrations of 5.4 mmol·L^{-1} (5.4 Ko) and 10 mmol·L^{-1} (10 Ko). (B) Normalized simulated *I-V* relationship for I_{K1} (olive and dark yellow lines). This simulated result is in close agreement with representative experimental result (o or o) which were digitized from Pandit et al. (2001)).

5.1.2.5 Hyperpolarization-activated current (I_f) module

The hyperpolarization-activated current (I_f) model is from the Pandit et al. (2001) model.

$$I_f = g_f y[f_{Na}(V - E_{Na}) + f_K(V - E_K)] \qquad \text{Eq 5-8, A.3.26.}$$

where g_f is the maximum conductance of the hyperpolarization-activated channel and y is the inactivation gate, E_{Na} is the equilibrium potential for Na^+, and E_K is the equilibrium potential for K^+. This formulation was adapted from Demir et al. study (Demir et al., 1994) and the values are based on experimental data from previous studies (Cerbai et al., 1996; Demir et al., 1994; Fares et al., 1998).

To isolate I_f, the extracellular and intracellular solution should be modified to reduce the interference of components other than I_f. The experimental condition set the extracellular K^+ and Na^+ concentrations at 25 $mmol{\cdot}L^{-1}$ and 30 $mmol{\cdot}L^{-1}$, respectively. The intracellular K^+ and Na^+ concentrations were 130 $mmol{\cdot}L^{-1}$ and 2 $mmol{\cdot}L^{-1}$, respectively. In addition, several inhibitors of other currents were needed. However, this I_f simulation was performed without these controls, which resulted in a little discrepancy in the current amplitude.

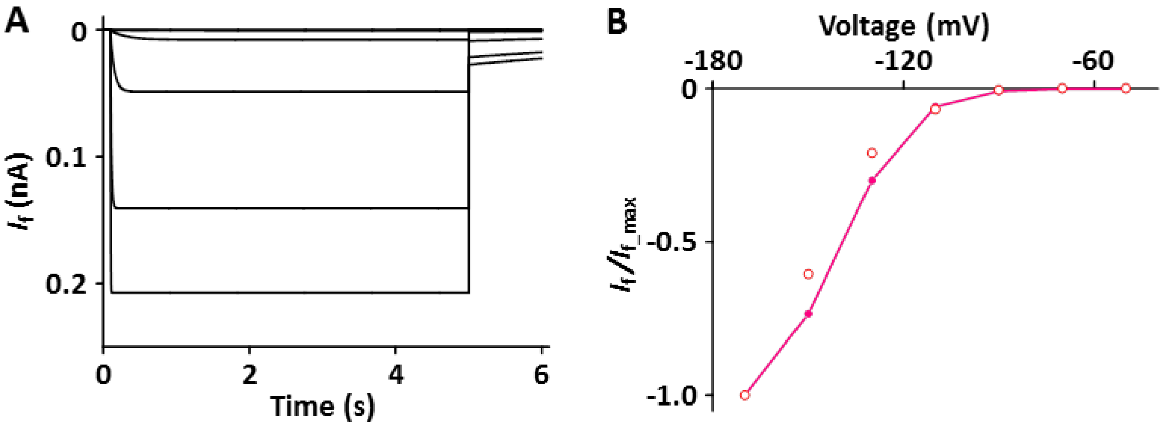

Figure 5.7. Verification of I_f OpenCOR implementation. (A) Simulated current traces of the hyperpolarization-activated channel. (B) Normalized simulated *I-V* relationship for I_f (pink line). This simulated result is in close agreement with representative experimental result (o, Fares et al. (1998)).

5.1.2.6 Background Na$^+$ current (I_{BNa}) module

The background Na$^+$ current (I_{BNa}) model is from the Pandit et al. (2001) model.

$$I_{BNa} = g_{BNa}(V - E_{Na})$$ Eq 5-9, A.3.30.

where g_{BNa} is the maximum conductance of the background Na$^+$ channel and E_{Na} is the equilibrium potential for Na$^+$. The magnitude is adjusted based on experimental data from Demir et al. (1994).

5.1.2.7 Background K$^+$ current (I_{BK}) module

The background K$^+$ current (I_{BK}) model is from the Pandit et al. (2001) model.

$$I_{BK} = g_{BK}(V - E_K)$$ Eq 5-10, A.3.31.

where g_{BK} is the maximum conductance of the background K$^+$ channel and E_K is the equilibrium potential for K$^+$. The magnitude is adjusted based on experimental data from Demir et al. (1994).

5.1.2.8 Na$^+$/K$^+$ pump current (I_{NaK}) module

The Na$^+$/K$^+$ pump (I_{NaK}) model is that of the Pandit et al. (2001) model adapted from earlier work by Luo and Rudy (1994).

$$I_{NaK} = \frac{\left(\overline{I_{NaK}} \cdot \frac{1}{\left(1.0 + 0.1245e^{-\frac{0.1VF}{RT}} + 0.0365\sigma e^{\frac{VF}{RT}}\right)} \cdot \frac{[K^+]_o}{\left([K^+]_o + k_{m,k}\right)}\right)}{\left(1 + \frac{k_{m,Na}}{[Na^+]_i}\right)^4}$$ Eq 5-11, A.3.32

where $\overline{I_{NaK}}$ is the maximum Na$^+$-K$^+$ pump current, σ is the [Na$^+$]$_o$-dependence factor for voltage-dependency, $K_{m,Na}$ is the half-maximum Na$^+$ binding constant for I_{NaK}, and $K_{m,K}$ is the half-maximum K$^+$ binding constant for I_{NaK}.

When normalized to 100 pF, the I_{NaK} model was 0.195 A·F^{-1} at 0 mV, which is close to the value of 0.2 A·F^{-1} at 0 mV in the experimental data of Stimers and Dobretsov (1998).

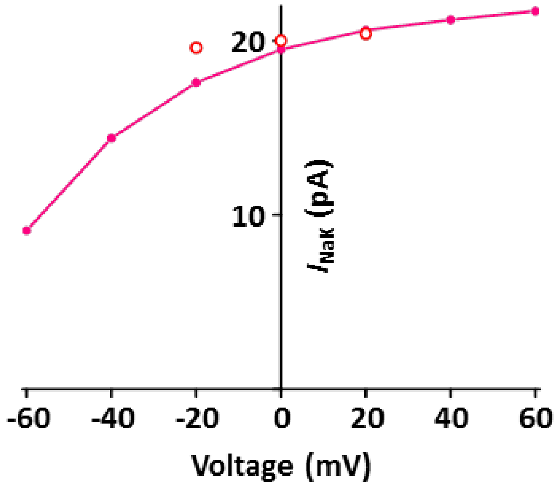

Figure 5.8. Verification of I_{NaK} OpenCOR implementation. Simulated *I-V* relationship for the sodium-potassium pump. o represents experimental data from Stimers and Dobretsov (1998).

5.1.2.9 Ca^{2+} release unit (CaRU) module

A Ca^{2+} release unit (CaRU) consists of one LCC and RYRs and transports Ca^{2+} ions in the dyadic subspace between the T-tubules and the sarcoplasmic reticulum (SR). The LCC and RYRs models are from Hinch et al. (2004) model, which is simplified by six coupled ordinary differential equations for Ca^{2+}-induced Ca^{2+} release.

The 3-state model of the LCC used here is simplified from the original 12-state model of the LCC by Jafri et al. (1998). The original 12-state model consists of 5 closed states ($C_{0,1,2,3,4}$), 5 inactivated states ($I_{0,1,2,3,4}$), 1 zero occupancy state (O_{Ca}), and 1 open state (O). These 12-state model was combined to make a 5-state Markov model and then simplified to a 3-state of LCC (see Figure 5.1 insert and Figure 5.9) based on mathematical assumptions about the separation of timescales that indicate the rates of transition between certain states are rapid relative to those between others. Therefore, the 3-state model of the LCC uses the derived states *I*, *C*, and *O* and the formulation of the open channel current is given by the Goldman-Hodgkin-Katz equation.

$$J_{LCC} = \; J_L \frac{zFV}{RT} \cdot \frac{[Ca^{2+}]_e \cdot e^{-\frac{zFV}{RT}} - [Ca^{2+}]_{ds}}{1 - e^{-\frac{zFV}{RT}}} \qquad \text{Eq 5-12}$$

where J_L is the permeability of single LCC, *z* is the number of moles of electrons, *F* is the Faraday's constant *R* is the ideal gas constant, *T* is the temperature, and $[Ca^{2+}]_{ds}$ is the Ca^{2+} concentration in the dyadic space.

The 3-state model for RYR is also is simplified from the original 5-state model of the RYR by Stern et al. (1999). As with the LCC model, transitions between two close states ($C_{1,2}$) and two inactivated states ($I_{1,2}$) were assumed to be rapid. Therefore, the 3-state model for RYR involves the derived states *I*, *C*, and *O* (see Figure 5.1 insert and Figure 5.9). The Ca^{2+} flux through opening RYR is the difference in [Ca^{2+}] between the SR and the local dyadic space.

$$J_{RYR} = J_R([Ca^{2+}]_{SR} - [Ca^{2+}]_{ds}) \qquad \text{Eq 5-13}$$

where J_R is the permeability of single RYR, $[Ca^{2+}]_{SR}$ is the Ca^{2+} concentration in the sarcoplasmic reticulum, and $[Ca^{2+}]_{ds}$ is the Ca^{2+} concentration in the dyadic space.

The 3-state LCC and the 3-state RYR models were combined to form a 9-state y_{ij} model (where *I, j* = *C, O,* and *I*), which was simplified further to produce a 4-state model of the CaRU (Figure 5.9). All parameters and functions of the model are shown in Appendix A.

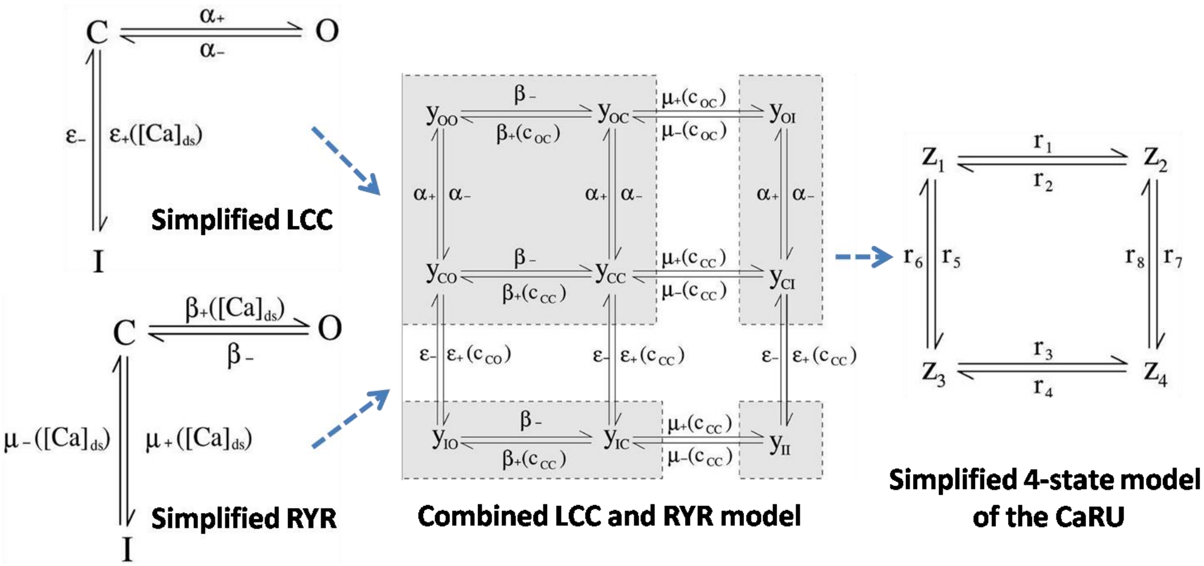

Figure 5.9. Schematic flowchart of the simplified CaRU model. Combined LCC and RYR model was made by combining simplified LCC and simplified RYR to form a 9-state y_{ij} model of the CaRU, where *i* and *j* are C, O or I state of the CaRU in the *i*th state of the LCC and the *j*th state of the RYR. y_{OO}, y_{OC}, y_{CO}, and y_{CC} are grouped together to form state Z_1, y_{OI} and y_{CI} are grouped together to form state Z_2, y_{IO} and y_{IC} are grouped together to form state Z_3, y_{II} forms state Z_1.

In one fixed condition with $[Ca^{2+}]_o$ = 1.2 mmol·L^{-1}, the peak *I-V* relationship for the Ca^{2+} channel was obtained by a voltage step from a holding potential of -50 mV and then compared with that measured experimentally. Simulated and measured currents were normalized so as to make the peak value of both equal to 1 at 0 mV, and both *I-V* curves are in close agreement. One feature of Ca^{2+} release is that the peak of I_{RYR} is shifted by ~10 mV in the hyperpolarizing direction relative to that of I_{LCC}, which is well simulated. Furthermore, EC coupling gain decreases as membrane voltage increases. This feature of simulated result corresponded well to published results (Figure 5.10).

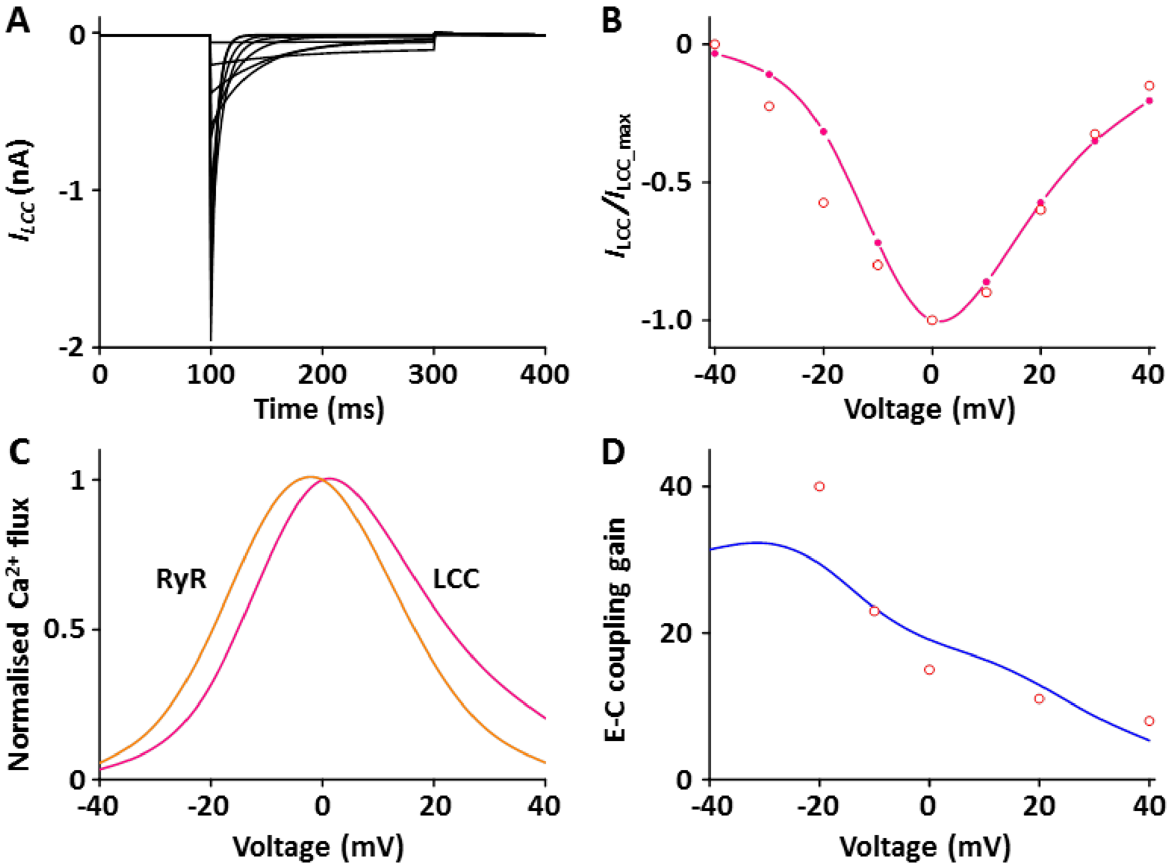

Figure 5.10. Verification of I_{LCC} and I_{RYR} OpenCOR implementation. (A) Simulated current traces for the LCC by a voltage step from -40 mV to 40 mV from a holding potential of -50 mV. (B) Normalised simulated *I-V* relationship for I_{LCC} (pink line). This simulated result is in close agreement with representative experimental result (o, Zahradnikova et al. (2004)). (C) Simulated peak fluxes of LCC (pink line) and RYR (yellow line) as a function of membrane voltage. (D) Simulated EC coupling gain (blue line, maximum of RYR flux/maximum LCC flux) is in close agreement with representative experimental result (o, Wier at al. (1994)).

5.1.2.10 Ca^{2+} pump current module

The SR Ca^{2+} pump, SERCA current (I_{SERCA}) model is from the Hinch et al. (2004) model.

$$I_{SERCA} = g_{SERCA}\frac{[Ca^{2+}]_i^2}{K_{SERCA}^2 + [Ca^{2+}]_i^2} \qquad \text{Eq 5-14, A.5.47.}$$

where g_{SERCA} is the maximum pump rate of SERCA and K_{SERCA} is the half saturation value of SERCA.

To verify the I_{SERCA} model, the calcium dependence of SERCA activity was generated and compared with experimental data (Figure 5.11).

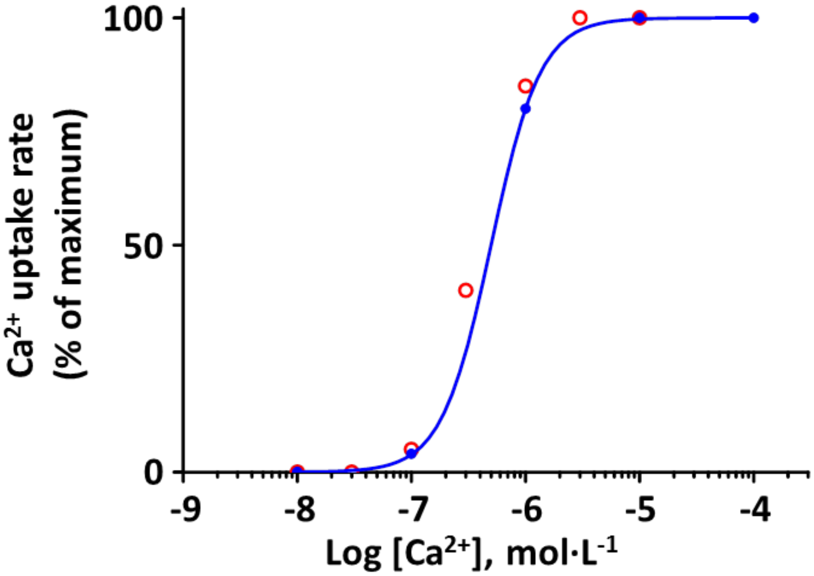

Figure 5.11. Verification of I_{SERCA} OpenCOR implementation. The calcium dependence of the relative rate of simulated SERCA activity is well plotted (blue line). This result is close agreement with representative experimental values (o, Lytton et al. (1992)).

The sarcolemmal Ca^{2+} pump current (I_{pCa}) model is from the Hinch et al. (2004) model.

$$I_{pCa} = g_{pCa}\frac{[Ca^{2+}]_i}{K_{m,pCa} + [Ca^{2+}]_i} \qquad \text{Eq 5-15, A.5.48.}$$

where g_{pCa} is the maximum pump rate of the sarcolemmal Ca^{2+} pump and $K_{m,pCa}$ is the half saturation value for sarcolemmal Ca^{2+} pump.

5.1.2.11 Na$^+$-Ca^{2+} exchanger current (I_{NCX}) module

The Na$^+$-Ca^{2+} exchanger current (I_{NCX}) model is from the Hinch et al. (2004) model.

$$I_{NCX} = g_{NCX}\frac{e^{\eta VF/RT}[Na^+]_i^3[Ca^{2+}]_e - e^{(\eta-1)VF/RT}[Na^+]_e^3[Ca^{2+}]_i}{\left(K_{m,Na}^3 + [Na^+]_e^3\right)\left([Ca^{2+}]_e + K_{m,Ca}\right)\left(1 + k_{sat}e^{(\eta-1)VF/RT}\right)} \qquad \text{Eq 5-16, A.5.49}$$

where g_{NCX} is the pump rate of NCX, η is the voltage dependence of NCX control, K_{mNa} is the sodium half saturation of NCX, K_{mCa} is the Ca^{2+} half saturation of NCX, k_{sat} is the low potential saturation factor of NCX, z is the number of moles of electrons, F is the Faraday's constant R is the ideal gas constant, and T is the temperature.

To isolate I_{NCX}, the extracellular and intracellular solution should be modified to reduce the interference of components other than I_{NCX}. The experimental condition by Li et al. (2013) was that extracellular Ca^{2+} and Na$^+$ concentrations were 1 mmol·L^{-1} and 140 mmol·L^{-1}, respectively and intracellular Na$^+$ and free Ca^{2+} concentrations were 20 mmol·L^{-1} and 1.2 μmol·L^{-1}, respectively. In addition, several inhibitors of other currents were needed. The simulated I_{NCX} model was generated without inhibitors, but the model output (Figure 5.12) shows close agreement with the experimental results of Li et al. (2013).

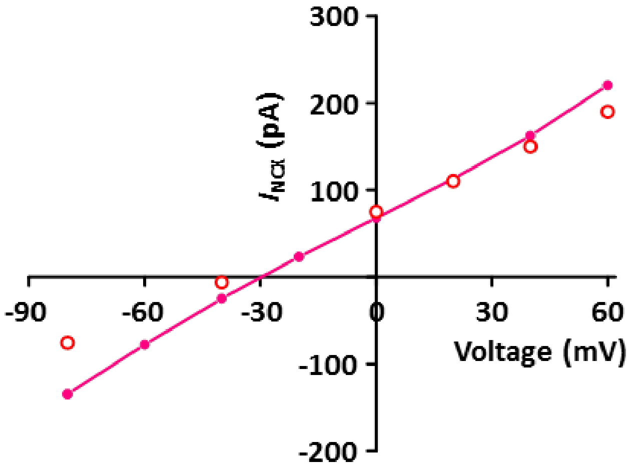

Figure 5.12. Verification of I_{NCX} OpenCOR implementation. Simulated *I-V* relationship for the NCX (pink line). This result is close agreement with representative experimental values (o, Li et al. (2013)).

5.1.2.12 Background Ca^{2+} current (I_{BCa}) module

The background Ca^{2+} current (I_{BCa}) model is from the Hinch et al. (2004) model.

$$I_{BCa} = g_{BCa}(V - E_{Ca}) \qquad \text{Eq 5-17, A.5.50}$$

where g_{BCa} is the maximum conductance for I_{BCa}, and E_{Ca} is the equilibrium potential of the Ca^{2+} channel.

The formulation of the equilibrium potential for the Ca^{2+} channel is from the Nernst equation:

$$E_{Ca} = \frac{RT}{zF} ln \frac{[Ca^{2+}]_o}{[Ca^{2+}]_i} \qquad \text{Eq 5-18, A.2.3.}$$

where *R* is the ideal gas constant, *T* is the temperature, *z* is the number of moles of electrons, and *F* is the Faraday's constant.

5.1.2.13 Calmodulin module

Ca^{2+} is buffered by calmodulin and troponin in the cytosol. The calculation of buffering by calmodulin is from the Pandit et al. (2001) model.

$$\beta_i = \left(1 + \frac{K_{CMDN}[B]_{CMDN}}{(K_{CMDN} + [Ca^{2+}]_i)^2} + \frac{K_m^{EGTA}[EGTA]_{tot}}{(K_m^{EGTA} + [Ca^{2+}]_i)^2}\right)^{-1} \qquad \text{Eq 5-19, A.5.42.}$$

where K_{CMDN} is Ca^{2+} half-saturation constant of calmodulin, $[B]_{CMDN}$ is the total cytosolic calmodulin concentration, K_m^{EGTA} is Ca^{2+} half-saturation constant of EGTA, and $[EGTA]_{tot}$ is total cytosolic EGTA concentration (Wagner and Keizer, 1994).

5.1.2.14 Troponin module

The troponin current (I_{TRPN}) model is from the Niederer et al. (2006) model.

$$I_{TRPN} = k_{on}\big([Ca^{2+}]_{TRPN\_max} - [TRPN]\big) - k_{off}[TRPN][Ca^{2+}]_i \qquad \text{Eq 5-20}$$

where k_{on} is the binding rate of Ca^{2+} to troponin, k_{off} is the dissociation rate of Ca^{2+} from troponin, and $[Ca^{2+}]_{TRPN\_max}$ is the maximum concentration of Ca^{2+} bound to troponin C. Tension-dependent unbinding rate is following:

$$k_{off} = k_{reoff}\left(1 - \frac{T}{\gamma T_{ref}}\right) \qquad \text{Eq 5-21}$$

where k_{reoff} is the unbinding rate in the absence of tension, γ is a measure of the affect of tension on the unbinding rate, T is the active tension, and T_{ref} is the reference tension.

5.1.2.15 Tropomyosin module

The tropomyosin was characterized by the fraction of actin sites available for crossbridge binding (*z*) and *z* is model is from the Niederer et al. (2006) model.

$$\frac{dz}{dt} = \alpha_0\left(\frac{[Ca^{2+}]_{Trpn}}{[Ca^{2+}]_{Trpn50}}\right)^n (1-z) - \alpha_{r1}z - \alpha_{r2}\frac{z^{n_r}}{z^{n_r} + K_z^{n_r}} \qquad \text{Eq 5-22}$$

where α_{r1} and α_{r2}, K_z and n_r are the slow and fast relaxation rates, respectively.

5.1.2.16 Crossbridge module

Tension development associated with crossbridge kinetics was described using the fading memory model (Niederer et al., 2006).

$$\mathrm{T} = \begin{cases} T_0 \dfrac{a\sum_{i=1}^{n} Q_i + 1}{1 - \sum_{i=1}^{n} Q_i}, & \displaystyle\sum_{i=1}^{n} Q_i < 0 \\ T_0 \dfrac{1 + (2+a)\sum_{i=1}^{n} Q_i}{1 + \sum_{i=1}^{n} Q_i}, & \displaystyle\sum_{i=1}^{n} Q_i > 0 \end{cases} \qquad \text{Eq 5-23}$$

where *a* is a measure of the curvature of the force-velocity relation and $\sum_{i=1}^{n} Q_i$ is defined as follows:

$$\sum_{i=1}^{n} Q_i = -\frac{d\lambda}{dt}\sum_{i=1}^{n}\frac{A_i}{\alpha_i} \qquad \text{Eq 5-24}$$

where λ is the strain, α_i is the exponential rate constants, and A_i is the associated weighing coefficient.

Eventually, the equation for isometric tension (T) is following (Niederer et al., 2006):

$$\mathrm{T} = T_{ref} \times (1 + \beta_0(\lambda - 1)) \times \frac{z}{z_{Max}} \qquad \text{Eq 5-25}$$

where T_{ref} is the reference tension, β_0 is the slope of the λ-maximum tension relationship, λ is the extension ratio, *z* is the fraction of available actin sites determined by the filament kinetics, and z_{Max} is the maximum fraction of available actin sites at a given sarcomere length.

5.1.3 Incorporating all components to the whole cell model

All individual modules were implemented as CellML components using the CellML model import facility in OpenCOR (http://www.opencor.ws/), which encompass module variables and mathematics: components for the whole cell model can be distributed among multiple files and copies of components from other files can be made in-memory using the CellML model import facility (Miller et al., 2010).

I illustrate the structure of the model, including separate files for units and component sets.

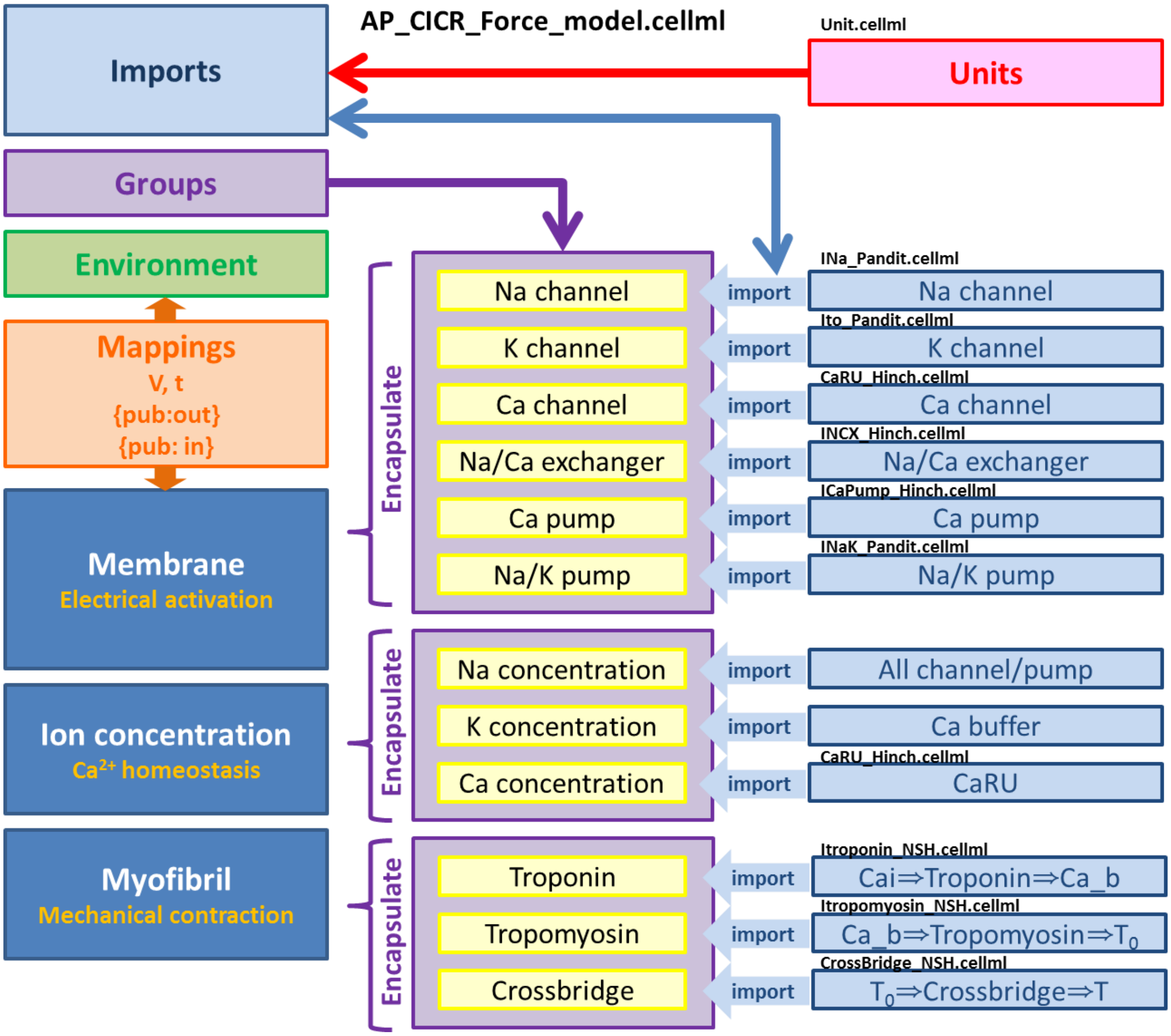

Figure 5.13. Overall structure of the AP_CICR_Force CellML model showing the encapsulation hierarchy (purple), the CellML model imports (blue) and the other key parts (units, components & mappings) of the top level CellML model.

When all components were incorporated, I adjusted the I_{LCC} parameters based on previous results (Kim et al., 2010). The potential when half LCC open (VL, see Appendix A) is the voltage at half-maximal activation, so I applied -15 mV and -10 mV for the LV and RV models, respectively. For I_{SERCA}, is the equation was adapted from earlier work by Jafri et al. (1998), as the maximum pump rate in their work is somewhat different from that in the rat. It is well known that the activity of SERCA is higher in the rat ventricle than in rabbit, ferret, dog, cat, guinea-pig and human ventricles (Bers, 2002). Therefore, g_{SERCA} was increased by 20% to achieve similar activity for rat SERCA, which is consistent with the Ca^{2+} transient results in this study. The parameters used in LV and RV models are summarized in Table 5.2.

I performed trabecular contraction experiments at 37°C, so that modified the parameters of the troponin and the tropomyosin modules. Temperature has some effect on the affinity of Ca^{2+} for TnC (McCubbin et al., 1980) and the affinity of Ca^{2+} for TnC was increased by 0.13 when temperature was increased from 21°C to 37°C (Gillis et al., 2000). Contraction times depend on relaxation rates as well as contraction rates. The close correspondence between the temperature and muscle relaxation has been reported and thus the relaxation kinetics was needed to be adjusted at 37°C. The wide range of Q_{10} values have been reported in order to reveal temperature dependence of force development in various muscles (Janssen et al., 2002; Peiper et al., 1975; Stein et al., 1982), I used 3 of Q_{10} value to parameterization of relaxation rates of tropomyosin.

Table 5.2. The parameters used in LV and RV models

Parameter	**LV**	**RV**
Potential when half LCC open (V_L)	-15 mV	-10 mV
Maximum pump rate of SERCA	0.45 $\mu mol \cdot L^{-1} \cdot s^{-1}$	0.45 $\mu mol \cdot L^{-1} \cdot s^{-1}$

5.2 Simulation results

To elicit an AP, I applied a stimulus current of 0.6 nA for 10 ms at 1 Hz to the model. This is in accordance with the experimental protocol that is generally used to elicit an AP. Before presenting the simulation results, Figure 5.14 shows representative experimental APs recorded from isolated LV and RV myocytes at 1 Hz. The LV AP has a prolonged duration and a more prominent plateau phase than the RV AP.

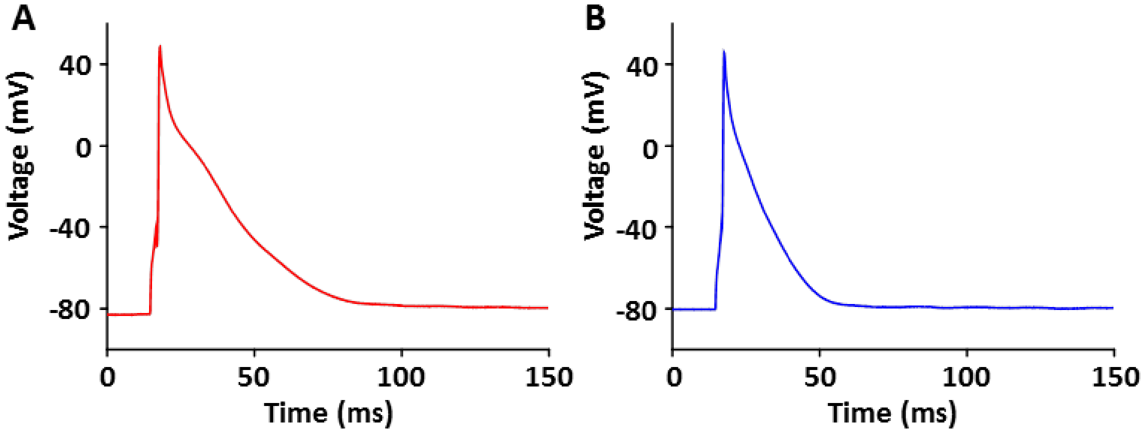

Figure 5.14. Representative LV (A) and RV (B) AP waveforms recorded experimentally.

This section deals with the simulation results of Ca^{2+} transients rather than other ion currents related to my experimental results.

To test the functionality of the model, it was paced at 1 Hz over 10 s. Snapshots of the resultant APs and calcium transients in LV and RV myocytes are shown in Figure 5.15.

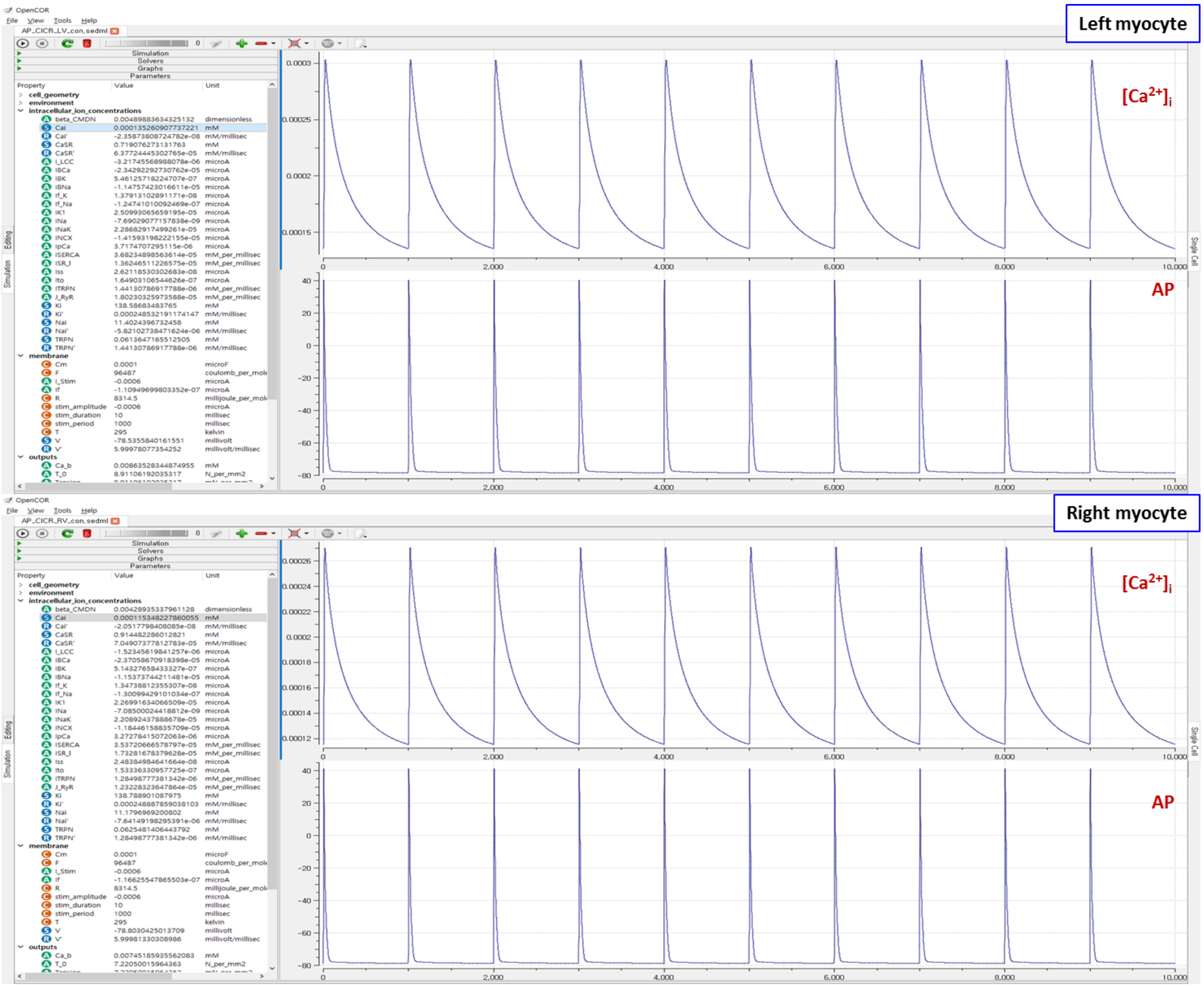

AP_CICR_LV_con.sedml

Property	Value	Unit
cell_geometry		
environment		
intracellular_ion_concentrations		
A beta_CMDN	0.00489883634325132	dimensionless
S Cai	0.000135260907737221	mM
R Cai'	-2.35873808724782e-08	mM/millisec
S CaSR	0.719076273131763	mM
R CaSR'	6.37724445302765e-05	mM/millisec
A I_LCC	-3.21745568988078e-06	microA
A IBCa	-2.34292292730762e-05	microA
A IBK	5.46125718224707e-07	microA
A IBNa	-1.14757423016611e-05	microA
A If_K	1.37913102891171e-08	microA
A If_Na	-1.24741010092469e-07	microA
A IK1	2.50993065659195e-05	microA
A INa	-7.69029077157838e-09	microA
A INaK	2.28682917499261e-05	microA
A INCX	-1.41593198222155e-05	microA
A IpCa	3.7174707295115e-06	microA
A ISERCA	3.68234898563614e-05	mM_per_millisec
A ISR_l	1.36246511226575e-05	mM_per_millisec
A Iss	2.62118530302683e-08	microA
A Ito	1.64903106544626e-07	microA
A ITRPN	1.44130786917788e-06	mM_per_millisec
A J_RyR	1.80230325973588e-05	mM_per_millisec
S Ki	138.58683483765	mM
R Ki'	0.000248532191174147	mM/millisec
S Nai	11.4024396732458	mM
R Nai'	-5.82102738471624e-06	mM/millisec
S TRPN	0.0613647165512505	mM
R TRPN'	1.44130786917788e-06	mM/millisec
membrane		
C Cm	0.0001	microF
C F	96487	coulomb_per_mol
A I_Stim	-0.0006	microA
A If	-1.10949699803352e-07	microA
C R	8314.5	millijoule_per_mol
C stim_amplitude	-0.0006	microA
C stim_duration	10	millisec
C stim_period	1000	millisec
C T	295	kelvin
S V	-78.5355840161551	millivolt
R V'	5.99978077354252	millivolt/millisec
outputs		
A Ca_b	0.00863528344874955	mM
A T_0	8.91106192035317	N_per_mm2

AP_CICR_RV_con.sedml

Property	Value	Unit
cell_geometry		
environment		
intracellular_ion_concentrations		
A beta_CMDN	0.00428935337961128	dimensionless
S Cai	0.000115348227860055	mM
R Cai'	-2.0517798408085e-08	mM/millisec
S CaSR	0.914482286012821	mM
R CaSR'	7.04907377812783e-05	mM/millisec
A I_LCC	-1.52345619841257e-06	microA
A IBCa	-2.37058670918398e-05	microA
A IBK	5.14327658433327e-07	microA
A IBNa	-1.15373744211481e-05	microA
A If_K	1.34738812355307e-08	microA
A If_Na	-1.30099429101034e-07	microA
A IK1	2.26991634066509e-05	microA
A INa	-7.08500024418812e-09	microA
A INaK	2.20892437888678e-05	microA
A INCX	-1.18446158835709e-05	microA
A IpCa	3.27278415072063e-06	microA
A ISERCA	3.53720666578797e-05	mM_per_millisec
A ISR_l	1.73281678379628e-05	mM_per_millisec
A Iss	2.48384984641664e-08	microA
A Ito	1.53336330957725e-07	microA
A ITRPN	1.28498777381342e-06	mM_per_millisec
A J_RyR	1.23228323647864e-05	mM_per_millisec
S Ki	138.788901087975	mM
R Ki'	0.000248887859038103	mM/millisec
S Nai	11.1796969200802	mM
R Nai'	-7.64149198295391e-06	mM/millisec
S TRPN	0.0625481406443792	mM
R TRPN'	1.28498777381342e-06	mM/millisec
membrane		
C Cm	0.0001	microF
C F	96487	coulomb_per_mol
A I_Stim	-0.0006	microA
A If	-1.16625547865503e-07	microA
C R	8314.5	millijoule_per_mol
C stim_amplitude	-0.0006	microA
C stim_duration	10	millisec
C stim_period	1000	millisec
C T	295	kelvin
S V	-78.8030425013709	millivolt
R V'	5.99981330308986	millivolt/millisec
outputs		
A Ca_b	0.00745185935562083	mM
A T_0	7.22050015964363	N_per_mm2

Figure 5.15. Results from OpenCOR for the whole cell electrophysiology model applied to LV and RV myocytes.

First, I compared the AP waveforms for LV and RV myocytes. The simulated results are shown in Figure 5.16 and validated with experimental results in Figure 5.17.

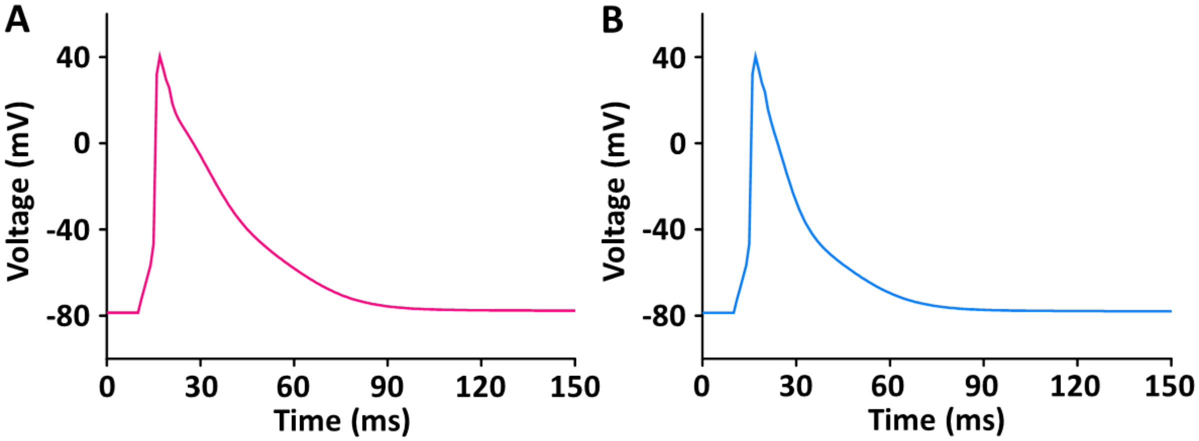

Figure 5.16. Model-generated LV (A) and RV (B) APs at 1 Hz.

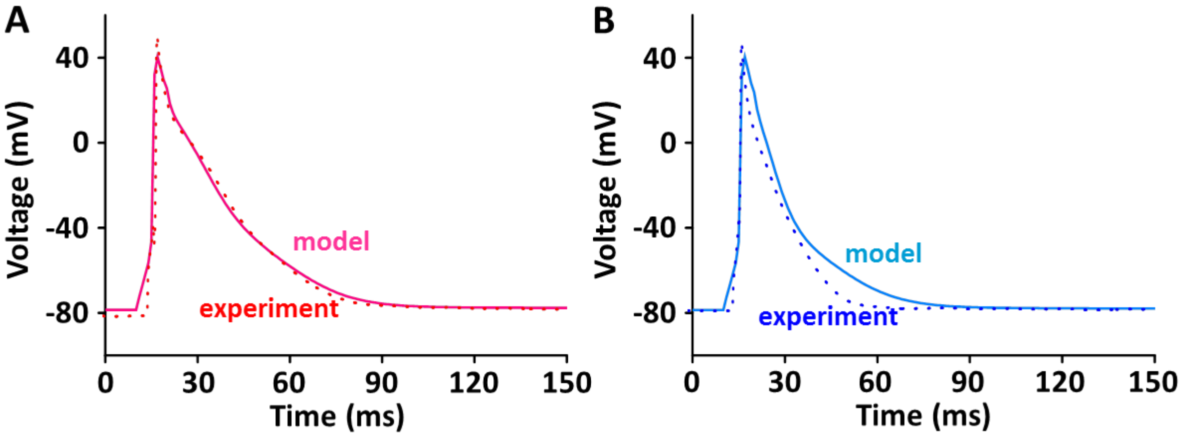

Figure 5.17. Validation of simulated APs with experimentally recorded LV (A) and RV (B) APs. Solid line: simulated result, dashed line: experimental result.

There is close agreement between the experimentally recorded and the simulated AP waveforms. The peak overshoot and duration of the simulated AP is very similar to the experimental recordings. Consistent with experimental results (Figure 5.17 and see (Kaprielian et al., 2002; Kim et al., 2010; Stankovicova et al., 2000)), the simulated LV AP also shows a prolonged AP duration and more prominent plateau phase compared to the simulated RV AP. However, there is a somewhat different configuration of the APs between simulation and experiment. This may be due in part to the fact that rat AP configurations show a variation in duration and shape due to transmural heterogeneity of APs (Kim et al., 2010; Stankovicova et al., 2000).

The model result for Ca^{2+} transients during the AP (Figure 5.18) conforms to the experimental observation that the Ca^{2+} decay is slower in LV than in RV myocytes (see Figures 4.1 - 4.3), which could cause a large Ca^{2+} flux in the LV myocyte. Moreover, the activity of SERCA in RV myocytes is assumed to be higher than in LV myocytes since RT_{50} against $[Ca^{2+}]_i$ was significantly different between LV and RV myocytes (≈ 30%) (see Figures 4.1 and 4.2 and see (Taylor et al., 2004)). This mechanism could contribute to the different change in $[Ca^{2+}]_i$ between LV and RV myocytes of each ventricle.

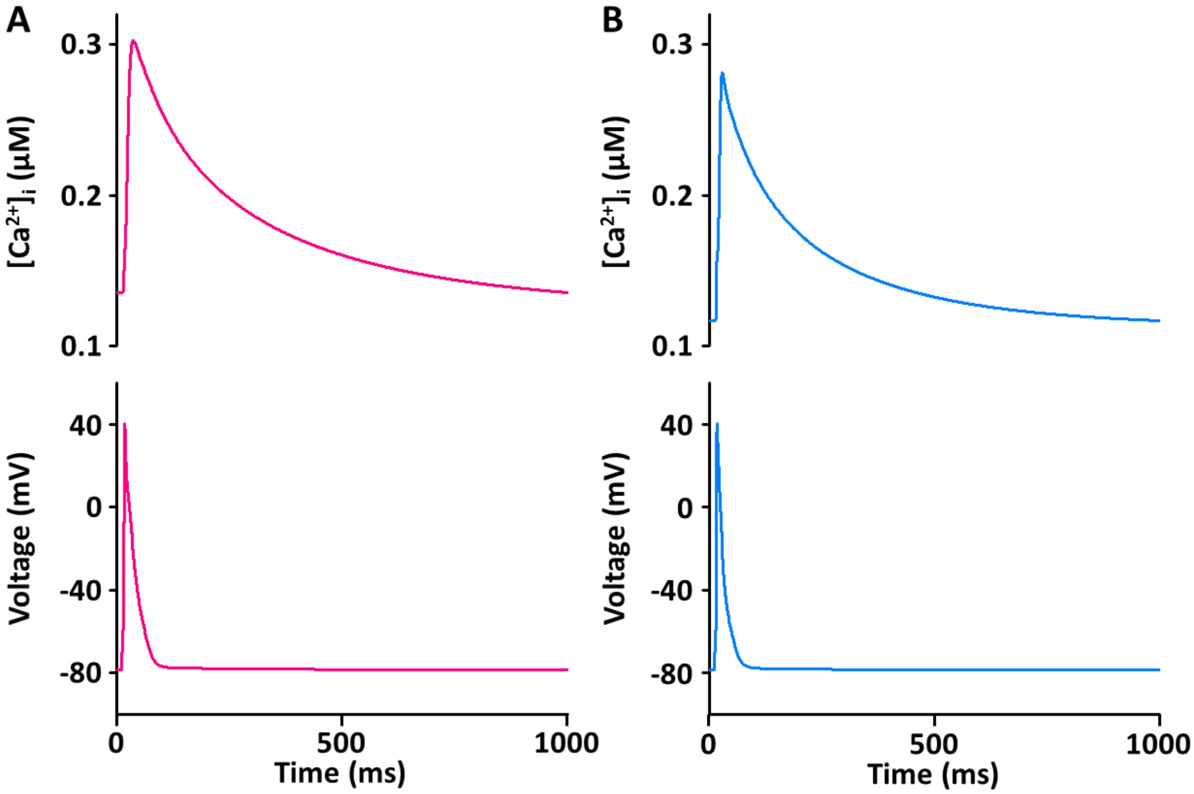

Figure 5.18. Simulated APs and the underlying changes in $[Ca^{2+}]_i$ for LV (A) and RV (B) myocytes.

As shown in simulations describing the changes in $[Ca^{2+}]_i$ (see also Figures 5.18 and 5.19), the predictions from my model for the kinetics of Ca^{2+} transient decay in the LV myocyte are much slower than those for the RV myocyte. These results were very well reproduced by “fine tuning” the model parameters of SERCA activity obtained from the study of Hinch et al. (2004).

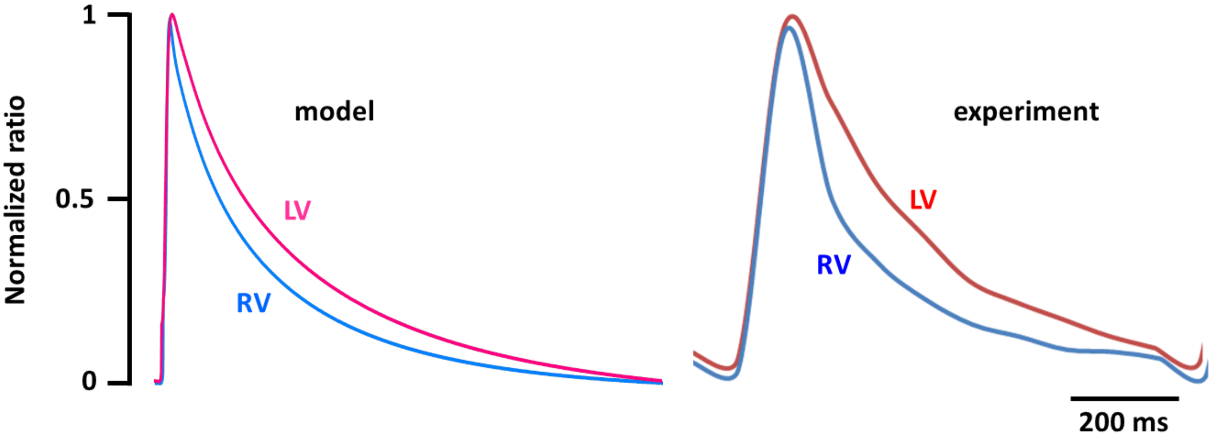

Figure 5.19. Tracings showing the normalized Ca^{2+} transients in model (A) and experimental recordings (B) for LV and RV myocytes.

In fact, the decline of the Ca^{2+} transient is regulated by SERCA as well as NCX. The parameterization of NCX activity may be considered, whereas > 95% of this decline is due to SERCA in rat myocytes (Milani-Nejad and Janssen, 2014). Therefore, the parameterization of SERCA activity is enough to prove the underlying mechanism for different Ca^{2+} transients between LV and RV myocytes.

To elicit tension production, the stimulus was same as in previous protocol. Figure 5.20 shows the simulation results for tension production over 10 s.

The simulated tensions for LV and RV are in close agreement with the experimentally recorded results. The peak and duration of the simulated tension are larger and longer, respectively, in the LV than in the RV myocytes. However, there is a somewhat different values of generated tension between simulated and experimental results.

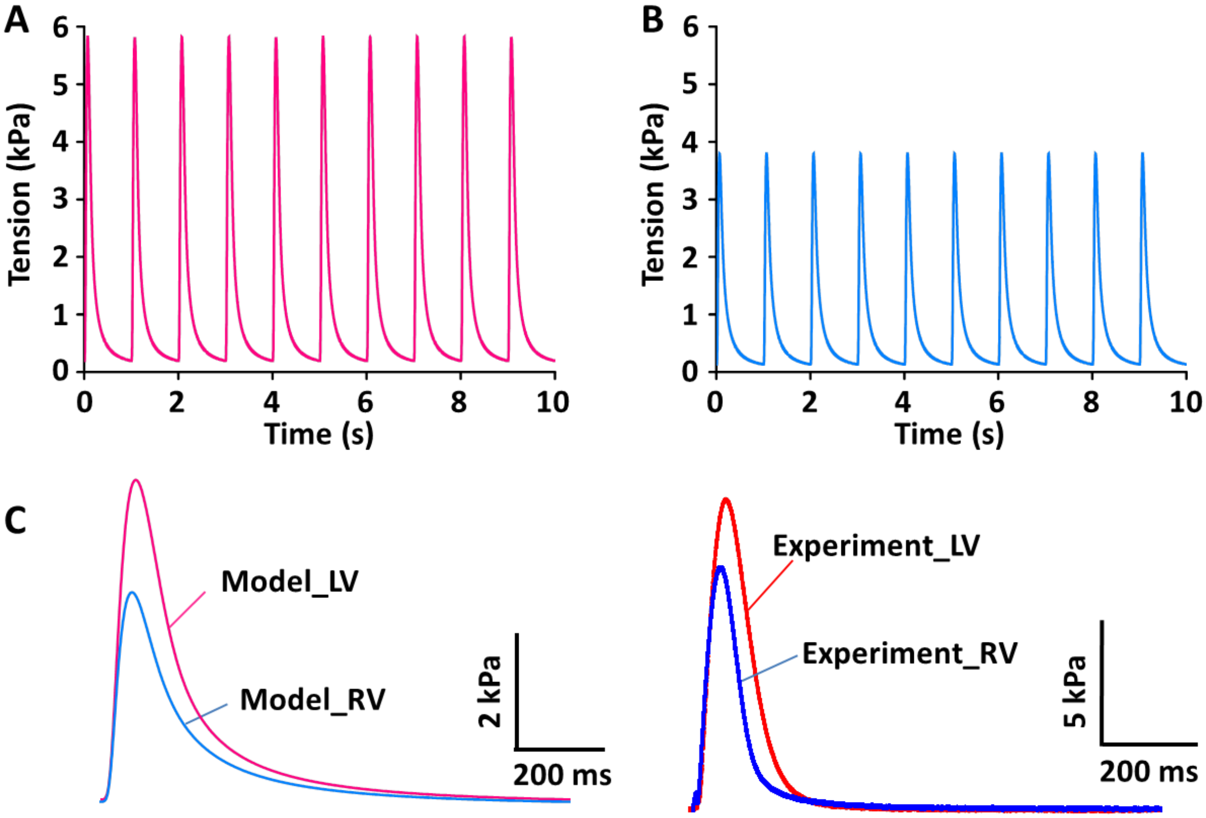

Figure 5.20. Model-generated tension production at 1 Hz. (A) The tension traces for the LV model. (B) The tension traces for the RV model. (C) Validation of simulated tensions with experimentally recorded LV and RV tensions.

Under physiological conditions (37°C), force of contraction and speed of relaxation are complex. Thus using the most variables based mainly on experimental data obtained at room temperature in present model may have a limitation to match perfectly, as temperature would significantly affect myofilament properties as well as Ca^{2+} handling (Janssen et al., 2002). However, even if the properties of troponin and tropomyosin and the activity of Ca^{2+} channel are adjusted, the model result is good enough to match the experimental results in this study. To verify distinct properties of contraction in the LV and RV, one of possible ionic mechanism, here VL of I_{LCC}, underlying the LV and RV APs was suggested and modified, which provide a good electromechanical linkage between the differences in Ca^{2+} handling and the corresponding changes in peak tension and duration of contraction.

Furthermore, Ca^{2+} transporters involved in relaxation under physiological conditions (37°C) has been reported to be accelerated compared to that at room temperature due to differences in temperature sensitivity of the involved systems (Mackiewicz and Lewartowski, 2006; Puglisi et al., 1996). Thus the maximum pump rate of SERCA needs to be adjusted to 37°C using the Q_{10} adjustment factor (1.415) to generate SFR. The SFR results of this simulation work are shown in Figure 5.21. Among Ca^{2+} transport systems, the modification of Ca^{2+} channels and SERCA is good enough to produce different contractility between the LV and RV, which could confirm the important contributors to that.

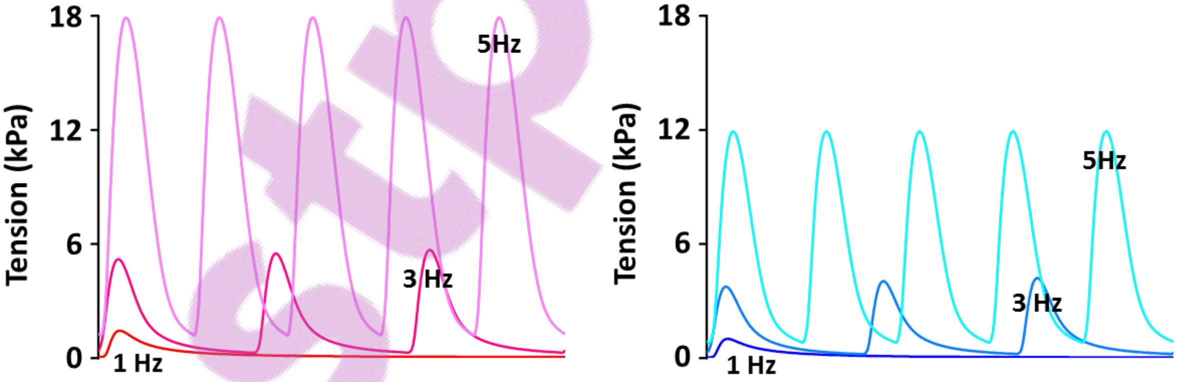

Figure 5.21. SFR of Simulated tension production between LV (A) and RV (B) myocytes.

Tensions simulated showed well positive SFR and their kinetics are close agreement with the experimentally recorded tensions (Figure 5.22).

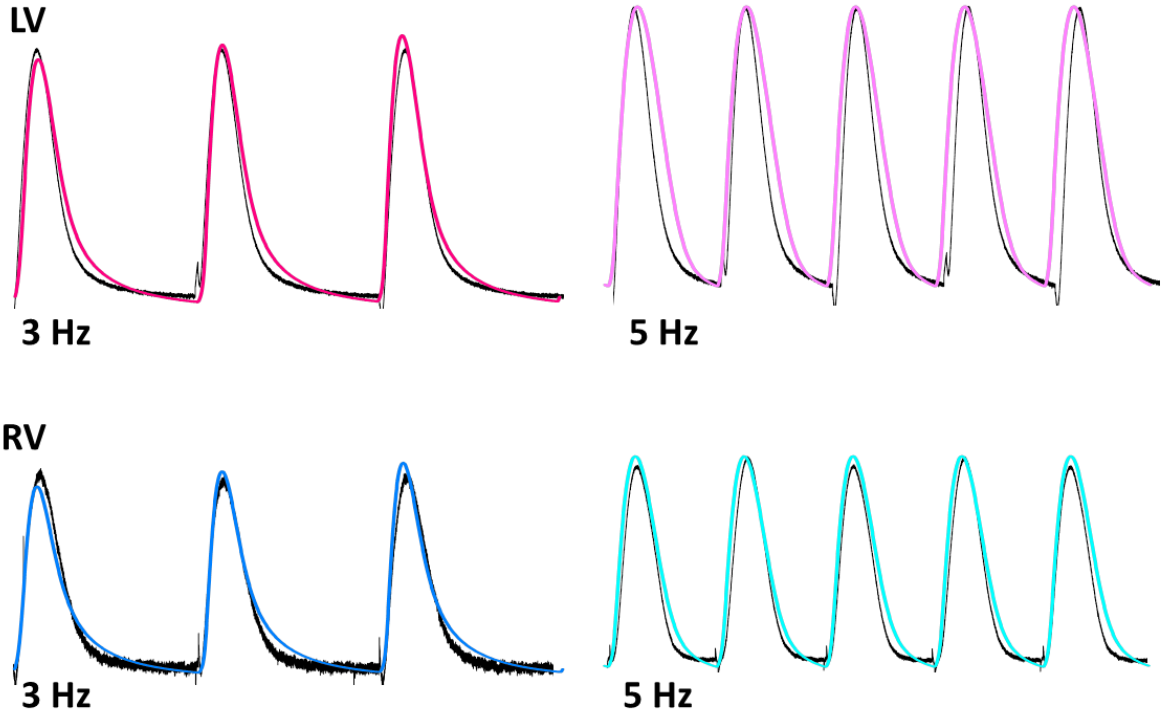

Figure 5.22. Traces for normalized tension at stimulations rates of 3 Hz and 5 Hz. Black lines: experimental data. Colored lines: simulated results.

Lastly, I tested the feasibility of this model to predict certain physiological and pathophysiological conditions by extrapolating ISO effect using parametrization of related module. ISO increases the activity of LCC, RYR, and SERCA via CaMKII and PKA, which lead to increase Ca^{2+} transient and contraction. Although this model dose not account for regulation by CaMKII or PKA, simulated Ca^{2+} transients with ISO treatment by modification of LCC, RYR, and SERCA activity based on previous study (Roof et al., 2011; Saraiva et al., 2003) shows close agreement with the experimentally recorded Ca^{2+} transients (Figure 5.23).

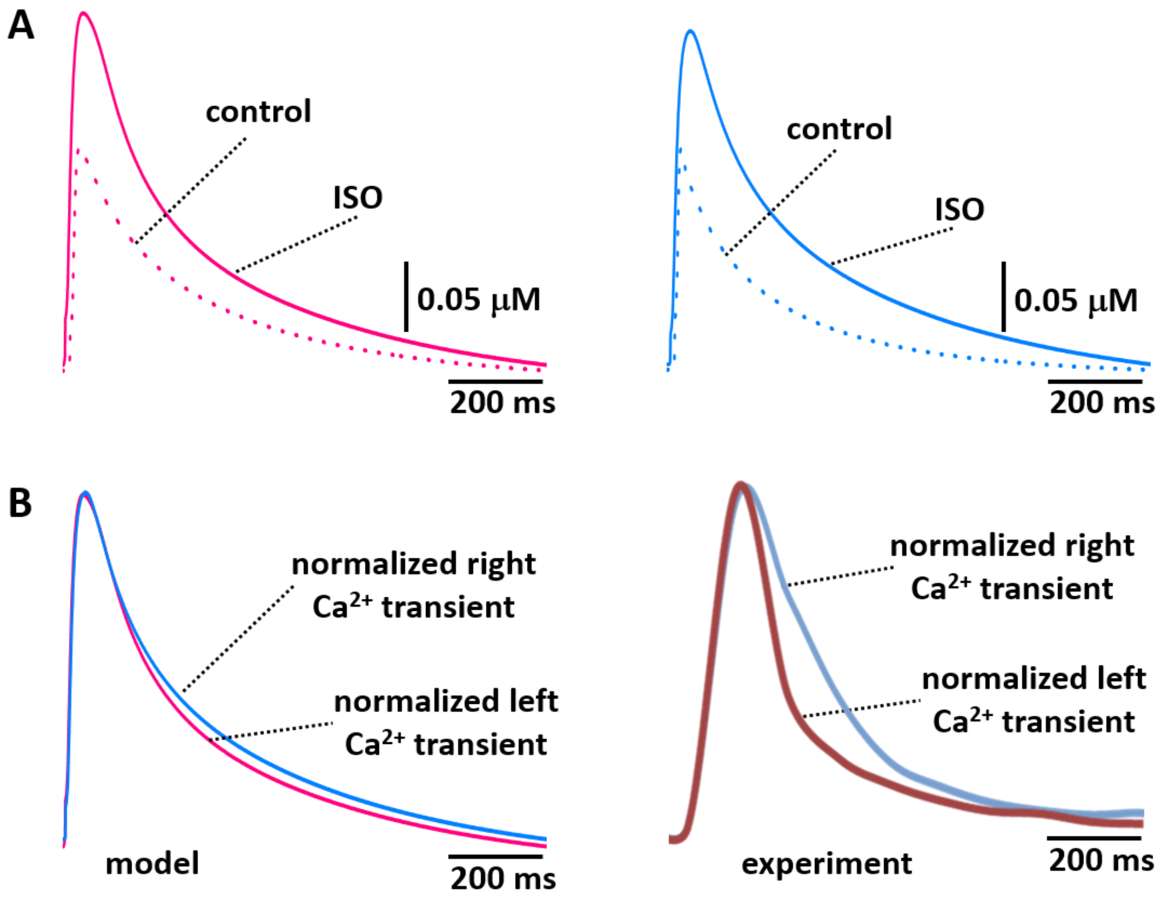

Figure 5.23. Model-generated Ca^{2+} transient by ISO stimulation at 1 Hz. (A) The Ca^{2+} transient traces for the LV (left) and RV (right) model. (B) Validation of simulated Ca^{2+} transient with experimentally recorded LV and RV myocytes.

5.3 Discussion

5.3.1 Numerical investigation for hypothesis verification

This modeling work would be a good example to use in constructing a complex model using the Physiome standard model protocol CellML in an efficient fashion which reuses existing computational models as modules. Importantly, all module models of this study could be subsumed into other or larger models without modification since each module components were separately constructed from existing models and validated based on the results of previous related papers. To implement the comprehensive electromechanical model, I assembled these reusable modules via component instances and encapsulation hierarchies.

The comprehensive electromechanical models for myocytes from the LV and RV regions of the rat are based on biophysical, experimentally derived components of ionic currents, transporters, and Ca^{2+} modulators as well as contractile proteins.

The present study is the first attempt to quantify and integrate an electromechanical model to explain the underlying mechanism for the differences in stress production between LV and RV myocytes. The different AP waveforms result in different Ca^{2+} fluxes, which may result from different SR Ca^{2+} loading and sequestration during the AP. This simulated result provides a plausible mechanistic linkage between prolonged AP duration and increased Ca^{2+} transient and greater stress in the LV compared to the RV. In this study, simulated results were in close agreement with those experimentally recorded. Furthermore, the models demonstrate the distinct properties of LV and RV myocytes.

In adult rat ventricular myocytes, ~ 90% of the Ca^{2+} source of the Ca^{2+} transient is that released from the SR (Bers, 2002), and subsequently, sequestration of Ca^{2+} by SERCA matches SR release. This important phenomenon is, therefore, the reason that this model should be combined with a sophisticated CICR model.

The primary contributor to CICR is LCC. Alteration of the kinetics of LCC would influence in the amount of Ca^{2+} released by RYR because LCC at the T-tubules is spatially tightly coupled with the RYRs of the SR. As shown in section 5.2, only adjustment with potential of half LCC opening and inactivation time provides proof of the hypothesis that the different stresses in the LV and RV result from differences in cellular and subcellular Ca^{2+} modulation proteins. The protein level/activity of SERCA has been suggested to affect the force-frequency behaviour of human myocardium: the protein levels of SERCA determine the systolic contractile reserves with respect to frequency potentiation of contractile force by playing a role in maintaining the SR load and regulating the cytosolic [Ca^{2+}] during both systole and diastole (Hasenfuss et al., 1994b). Even though this study did not directly reveal the activity of SERCA experimentally, the experimental results for SFR per se and the effect of adrenergic agonists on SFR, diastolic stress, and the Ca^{2+} transient permit prediction of how LCC and SERCA determine the electromechanical properties of the heart.

The specific aim for this simulation was to establish that the ionic mechanisms underlying the APs play a role in the variation in force production between ventricles. These simulation results thus provide a good electromechanical linkage between the differences in Ca^{2+} handling and the corresponding tension changes.

This simulation process also provides a useful way to reuse and elaborate upon existing models, as well as individual unit models, in order to develop a new model.

5.3.2 Model application/utility

In this study, the same model frameworks were used to represent physiological function for different cardiac electromechanics by adjusting the parameter values. Parameterization of the important variables governing physiological mechanisms could be exploited to provide a method for quantifying differences in electromechanics between the LV and RV. This provides the opportunity to deeply understand the contributions of ion conductivities and kinetics, myofibrilar kinetics, and adrenergic stimulation to cardiac function. Furthermore, understanding such differences between the LV and RV is important for the use of the models to guide clinical interventions. This simple approach could allow one to account for phenomenological functions which are able to capture signal traces as well as kinetic.

.

5.3.3 Limitations of the study and future work

A general problem in the AP model of the ventricular myocyte is the large variability in the observed phenotypes due to transmural heterogeneity through the ventricular wall, especially in the left ventricle (Kim et al., 2010). However, the representative AP waveform used in this model could minimize the effect of this variability because overall APs in the LV have longer durations than in the RV.

This model is somewhat limited to Ca^{2+}-dependent regulatory proteins such as CaMKII, calcineurin (CaN), phospholamban, and cAMP. These proteins alter the functions of multiple targets and thus are related to rate-dependent cellular response. LCC is influenced by Ca^{2+}-dependent inactivation and Ca^{2+}-dependent facilitation via activations of CaMKII and CaN (Hudmon et al., 2005; Pitt et al., 2001; Tandan et al., 2009). CaMKII and CaN also affect rate-dependent acceleration of relaxation via regulation of SERCA activity (Munch et al., 2002; Toyofuku et al., 1994). β-adrenergic stimulation could upregulate LCC, RYR, NCX, and pump currents via increasing the level of cAMP (Danziger et al., 1990), which also influence SFR in rat ventricular myocytes. Therefore, future work is needed to implement individual modules of these proteins and then combine them with existing model.

In fact, cardiac muscle relaxation is a system level property that requires fundamental integration of three governing systems: intracellular calcium decline, thin filament deactivation, and cross-bridge cycling kinetics (Biesiadecki et al., 2014). Therefore, although this model is a simplified model of a complex multiphysics system, in future work I plan to use this study framework to link the overall process step by step. As this model is modular, all modules are available to reuse, reproduce, and extend to a future larger more complex model.

5.4 Chapter Summary

In this study, I simulated the APs and Ca^{2+} dynamics underlying excitation-contraction coupling in rat LV and RV myocytes based on experimental results, and then linked this electrophysiological model to an existing model of tension production. The experimental and computational methods used simultaneously here could be used to expand our understanding of the functional consequences of physiological and pathophysiological conditions, as well as to analyse reductive data observed in experiments.

I have shown, with experiments and modelling, that important differences exist between LV and RV myocytes. Compared to RV myocytes, LV myocytes have longer AP durations and larger Ca^{2+} sources, with significant contributions via LCC and SERCA. Distinguishing these features helps us to understand the underlying mechanisms behind the different electromechanical properties in myocytes and in trabeculae.

Chapter 6

Thesis Summary

6.1 Main Findings

The aim of my study was to determine whether the stress development in cardiac muscle differs between LV and RV and to examine the underlying mechanism of that difference at the cellular level through a combination of experimental and mathematical modelling studies.

Since myocardial wall stress is known to be one of the primary determinants of myocardial oxygen consumption (Sarnoff et al., 1958), many studies have attempted to understand the alteration of wall stress as part of the feedback mechanism underlying the progression of heart diseases (Alpert et al., 1974; Di Napoli et al., 2003; Zhang et al., 2011). While approaches to improving cardiac performance in heart diseases are equally applicable to the LV and RV, appropriate therapy for LV dysfunction has been shown to be not necessarily ideal for RV dysfunction (Bleasdale and Frenneaux, 2002; Hoch and Rosenfeld, 1992).

This thesis was therefore motivated by the desire to quantify the wall stress in the LV and RV in order to obtain a better understanding of normal ventricular mechanics. This attempt involved using one of the best approaches for obtaining a realistic quantitative assessment of ventricular wall stress: measuring quasi-isometric contraction in isolated cardiac muscles (Chapter 3). To investigate the underlying mechanism, I performed experiments using Ca^{2+} imaging (Chapter 4) and carried out a simulation using biophysical whole cell models (Chapter 5).

The main findings arising from assessing the stresses in isolated trabeculae muscles (Chapter 3) were: (1) the peak stresses in LV and RV trabeculae were not significantly different (see Figure 3.4) but the twitch time constants were significantly smaller in RV trabeculae than in LV trabeculae (see Figure 3.6), and the stress-frequency relationship (SFR) in both groups was flat in the range of physiological frequencies at 37°C (see Figure 3.4); (2) β-adrenergic stimulation with ISO resulted in a positive SFR (see Figure 3.9B) which significantly reduced the twitch time constants and increased maximum rates of stress development in both groups in the range of physiological frequencies at 37°C; and (3) non-specific adrenergic stimulation with norepinephrine (NE) yielded an enhancement in stress, but unchanged (flat) SFR and twitch time constants in both groups in the range of physiological frequencies at 37°C (see Figures 3.13 to 3.15).

The main findings arising from measuring Ca^{2+} transients in isolated single myocytes (Chapter 4) were: (1) the average peak ratio of Ca^{2+} transients between LV and RV myocytes was not significantly different; however, the decay of the Ca^{2+} transients was much faster in RV than in LV myocytes at 25°C (see Figure 4.2); and (2) the effect of β-adrenergic stimulation on Ca^{2+} transient was greater, with delayed decay in RV myocytes compared to LV myocytes at 25°C (see Figure 4.4).

The main findings related to simulating APs, Ca^{2+} dynamics, and isometric tension for single myocytes (Chapter 5) showed: (1) there was close agreement between experimentally recorded and simulated AP and Ca^{2+} transient waveforms; (2) the simulated LV AP showed a prolonged AP duration and a more prominent plateau phase compared with the simulated RV AP; (3) the simulated Ca^{2+} transient showed prolonged duration and higher diastolic value in LV compared to RV myocytes; (4) the peak value and relaxation of the simulated isometric tension were larger and slower, respectively, in LV compared to RV myocytes.

The value of the current experimental study lies in the determination of both quantitative and qualitative differences between the left and right heart at different spatial levels. Findings that the fundamental properties of the myocardium differ between the left and right heart gives us an insight on which to base medical planning or interventions, using appropriate approaches for the two ventricles.

The current modeling study allowed the implementation and testing of each of the currents individually for a database of validated modular models (component models), which are available to reuse. To construct models by reusing components encoded with CellML enables computational efficiency and easy optimization. I successfully constructed the integrated cellular model by using a modular approach with CellML. This model, informed by the present experimental data, demonstrates well how the underlying mechanisms at a molecular level contribute to phenotype in higher levels, especially based on the description of the Ca^{2+} handling mechanism in the sarcoplasmic reticulum and the sarcolemmal membrane. This enables understanding of wall stress development in the left and right ventricles. Therefore, modelling is suggested as one of the best ways to assess both left and right ventricular function together, as the assessment of right ventricular function has previously been very difficult.

To my knowledge, this is the first comprehensive study of multi-scale electromechanics in the rat heart to examine ventricular wall stress. The results from the current study at two discrete spatial scales of the heart reach the same conclusion: there is an unequivocal fundamental difference in electromechanics between the left and right ventricles.

6.2 Limitations and Future Work

In the present study, I suggested varying activity of SERCA as one of the underlying mechanisms that could contribute to the production of different stresses in the LV and RV. However, I did not measure such differences experimentally. The activity of RYR should also be evaluated experimentally for a more comprehensive understanding of Ca^{2+} dynamics in the LV and RV. Further studies that include these measurements would provide helpful information that may help in finding specific candidates to modulate cardiac performance in clinical applications as well as in basic research.

The ultimate goal for the future development of the present model would be to embed and couple the cell model into a whole organ model, using additional existing higher-scale electromechanical models.

Appendix A

Model Summary

1. Membrane potential

$$\frac{dV}{dt} = -\frac{1}{Cm}\left(I_{Na} + I_{CaL} + I_t + I_{ss} + I_f + I_{K1} + I_B + I_{NaK} + I_{NaCa} + I_{CaP} - I_{stim}\right) \quad \text{(A.1.1)}$$

2. Nernst potentials

$$E_{Na} = \frac{RT}{F} \ ln\frac{[Na^+]_o}{[Na^+]_i} \quad \text{(A.2.1)}$$

$$E_K = \frac{RT}{F} \ ln\frac{[K^+]_o}{[K^+]_i} \quad \text{(A.2.2)}$$

$$E_{Ca} = \frac{RT}{2F} \ ln\frac{[Ca^{2+}]_o}{[Ca^{2+}]_i} \quad \text{(A.2.3)}$$

3. Membrane currents

3.1. Na$^+$ current

$$I_{Na} = g_{Na}m^3hj(V - E_{Na}) \quad \text{(A.3.1)}$$

$$\overline{m} = \frac{1}{(1 + e^{(V+45)/-6.5})} \quad \text{(A.3.2)}$$

$$\overline{h} = \overline{J} = \frac{1}{(1 + e^{(V+76)/6.07})} \quad \text{(A.3.3)}$$

$$\frac{dm}{dt} = \frac{\overline{m} - m}{\tau_m} \quad \text{(A.3.4)}$$

$$\frac{dh}{dt} = \frac{\overline{h} - h}{\tau_h} \quad \text{(A.3.5)}$$

$$\frac{dj}{dt} = \frac{\bar{j} - j}{\tau_j} \tag{A.3.6}$$

$$\tau_m = \frac{1.36}{\left(\frac{0.32(V + 47.13)}{1.0 - e^{-0.1(V+47.13)}} + 0.08e^{-V/11}\right)} \tag{A.3.7}$$

$$\tau_h = \begin{cases} \dfrac{3.49}{0.135e^{-\frac{V+80}{6.8}} + 3.5e^{0.079V} + 3.1 \times 10^5 e^{0.35V}}, & V < -40 \\ 0.0004537\left(1.0 + e^{-\frac{(V+10.66)}{11.1}}\right), & V \geq -40 \end{cases} \tag{A.3.8}$$

$$\tau_j = \begin{cases} 3.49 \div \left[\dfrac{V + 37.78}{1.0 + e^{0.311(V+79.23)}}\left(-127140e^{0.2444V} - 3.474 \times 10^{-5}e^{-0.04391V}\right) + \dfrac{0.1212e^{-0.01052V}}{1.0 + e^{-0.1378(V+40.14)}}\right], & V < -40mV \\ \dfrac{11.63\left(1.0 + e^{-\frac{(V+32)}{11.1}}\right)}{e^{-2.535\times 10^{-7}V}}, & V \geq -40\ mV \end{cases} \tag{A.3.9}$$

3.2. *Ca^{2+}-independent transient outward K^{+} current*

$$I_t = g_t r(as + bs_{slow})(V - E_K) \tag{A.3.10}$$

$$a = 0.886, b = 0.114$$

$$\bar{r} = \frac{1}{(1 + e^{(V+10.6)/-11.42})} \tag{A.3.11}$$

$$\bar{s} = \overline{s_{slow}} = \frac{1}{(1 + e^{(V+45.3)/6.8841})} \tag{A.3.12}$$

$$\tau_r = \frac{1000}{45.16e^{0.03577(V+50.0)} + 98.9e^{-0.1(V+38.0)}} \tag{A.3.13}$$

$$\tau_s = 350e^{-(V+70.0/15.0)^2} + 35 \tag{A.3.14}$$

$$\tau_{s_{slow}} = 3700e^{-(V+70.0/30.0)^2} + 35 \tag{A.3.15}$$

$$\frac{dr}{dt} = \frac{\bar{r} - \ r}{\tau_r} \tag{A.3.16}$$

$$\frac{ds}{dt} = \frac{\bar{s} - \ s}{\tau_s} \tag{A.3.17}$$

$$\frac{ds_{slow}}{dt} = \frac{\overline{s_{slow}} - \ s_{slow}}{\tau_{s_{slow}}} \tag{A.3.18}$$

3.3. Steady-state outward K⁺ current

$$I_{ss} = g_{ss} r_{ss} s_{ss} (V - E_K) \tag{A.3.19}$$

$$\overline{r_{ss}} \ = \ \frac{1}{1 + e^{(V+11.5)/-11.82}} \tag{A.3.20}$$

$$\overline{s_{ss}} = \ \frac{1}{1 + e^{(V+87.5)/10.3}} \tag{A.3.21}$$

$$\tau_{r_{ss}} = \frac{10000}{45.16e^{0.03577(V+50.0)} + 98.9e^{-0.1(V+38.0)}} \tag{A.3.22}$$

$$\tau_{s_{ss}} = 2100$$

$$\frac{dr_{ss}}{dt} = \frac{\overline{r_{ss}} - \ r_{ss}}{\tau_{r_{ss}}} \tag{A.3.23}$$

$$\frac{ds_{ss}}{dt} = \frac{\overline{s_{ss}} - \ s_{ss}}{\tau_{s_{ss}}} \tag{A.3.24}$$

3.4. Inward rectifier K⁺ current

$$I_{K1} = \left[\frac{0.048}{e^{\frac{(V+37)}{25}} + e^{\frac{(V+37)}{-25}}} + 0.01\right] \cdot \left[\frac{0.001}{1 + e^{\frac{(V-E_K-76.77)}{-17}}}\right] + \frac{g_{K1}(V - E_K - 1.73)}{(1 + e^{1.613F(V-E_K-1.73)/RT}) \cdot (1 + e^{[K^+]_o - 0.9988/-0.124})} \tag{A.3.25}$$

3.5. Hyperpolarizing-activated current

$$I_f = g_f y[f_{Na}(V - E_{Na}) + f_K(V - E_K)] \tag{A.3.26}$$

$$y_\infty \;=\; \frac{1}{1 + e^{(V+138.6)/10.48}} \tag{A.3.27}$$

$$f_{Na} = 0.2, \qquad f_K = 1 - f_{Na}$$

$$\tau_y = \frac{1000}{(0.11885e^{(V+80.0)/28.37} + 0.56236e^{(V+80.0)/-14.19})} \tag{A.3.28}$$

$$\frac{dy}{dt} = \frac{\overline{y_\infty} - \;\; y}{\tau_y} \tag{A.3.29}$$

3.6. Background Na⁺ current

$$I_{BNa} = g_{BNa}(V - E_{Na}) \tag{A.3.30}$$

3.7. Background K⁺ current

$$I_{BK} = g_{BK}(V - E_K) \tag{A.3.31}$$

3.8. Na^+-K^+ pump current

$$I_{NaK} = \frac{\left(\overline{I_{NaK}} \cdot \frac{1}{\left(1.0 + \ 0.1245 e^{-\frac{0.1VF}{RT}} + 0.0365 \sigma e^{\frac{VF}{RT}}\right)} \ \cdot \ \frac{[K^+]_o}{\left([K^+]_o + k_{m,k}\right)}\right)}{\left(1 + \ \frac{k_{m,Na}}{[Na^+]_i}\right)^4} \qquad \text{(A.3.32)}$$

4. Intracellular ion concentration

$$\frac{d[Na^+]_i}{dt} = \ -(I_{Na} + I_{BNa} + 3I_{NaCa} + 3I_{NaK} + I_{f,Na}) \frac{1.0}{V_{myo\_\mu l} F} \qquad \text{(A.4.1)}$$

$$\frac{d[K^+]_i}{dt} = \ -(I_{ss} + I_{BK} + I_t + I_{K1} + I_{f,K} - 2I_{NaK}) \frac{1.0}{V_{myo\_\mu l} F} \qquad \text{(A.4.2)}$$

5. Calcium dynamics

5.1. Calcium concentration

$$\frac{d[Ca^{2+}]_i}{dt} = \beta_i \ \left\{ I_{RyR} - I_{SERCA} + I_{SR} + I_{TRPN} - (I_{LCC} + I_{BCa} - 2I_{NaCa} + I_{CaP}) \frac{1.0}{2V_{myo} F} \right\} \qquad \text{(A.5.1)}$$

$$\frac{d[Ca^{2+}]_{SR}}{dt} = \left(-I_{RyR} + I_{SERCA} - I_{SR,l}\right) \frac{V_{myo\_\mu l}}{V_{SR\_\mu l}} \qquad \text{(A.5.2)}$$

$$\frac{d[TRPN]}{dt} = I_{TRPN} \qquad \text{(A.5.3)}$$

5.2. Dyadic space calcium concentrations

$$C_{cc} = [Ca^{2+}]_i \tag{A.5.4}$$

$$C_{co} = \frac{[Ca^{2+}]_i + \frac{J_R}{g_D}[Ca^{2+}]_{SR}}{1 + \frac{J_R}{g_D}} \tag{A.5.5}$$

$$C_{oc} = \frac{[Ca^{2+}]_i + \frac{J_L}{g_D}[Ca^{2+}]_e \frac{\delta V e^{-\delta V}}{1 - e^{-\delta V}}}{1 + \frac{J_R}{g_D}\frac{\delta V}{1 - e^{-\delta V}}} \tag{A.5.6}$$

$$C_{oo} = \frac{[Ca^{2+}]_i + \frac{J_R}{g_D}[Ca^{2+}]_{SR} + \frac{J_L}{g_D}[Ca^{2+}]_e \frac{\delta V e^{-\delta V}}{1 - e^{-\delta V}}}{1 + \frac{J_R}{g_D} + \frac{J_L}{g_D}\frac{\delta V}{1 - e^{-\delta V}}} \tag{A.5.7}$$

5.3. Transition rates for the three-state LCC

$$\alpha^{+} = \frac{e^{\frac{(V-V_L)}{\Delta V_L}}}{t_L\left(e^{\frac{(V-V_L)}{\Delta V_L}} + 1\right)} \tag{A.5.8}$$

$$\alpha^{-} = \frac{\varnothing_L}{t_L} \tag{A.5.9}$$

$$\epsilon_{co}^{+} = \frac{C_{co}\left(e^{\frac{(V-V_L)}{\Delta V_L}} + a\right)}{\tau_L K_L\left(e^{\frac{(V-V_L)}{\Delta V_L}} + 1\right)} \tag{A.5.10}$$

$$\epsilon_{cc}^{+} = \frac{[Ca^{2+}]_i\left(e^{\frac{(V-V_L)}{\Delta V_L}} + a\right)}{\tau_L K_L\left(e^{\frac{(V-V_L)}{\Delta V_L}} + 1\right)} \tag{A.5.11}$$

$$\epsilon^- = \frac{b\left(e^{\frac{(V-V_L)}{\Delta V_L}} + \ \ a\right)}{\tau_L\left(be^{\frac{(V-V_L)}{\Delta V_L}} + \ \ a\right)} \tag{A.5.12}$$

5.4. Transition rates for the three-state RYR

$$\beta_{oc}^+ = \frac{(C_{oc})^2}{t_R\left((C_{oc})^2 + \ \ \left(K_{RyR}\right)^2\right)} \tag{A.5.13}$$

$$\beta_{cc}^+ = \frac{([Ca^{2+}]_i)^2}{t_R\left(([Ca^{2+}]_i)^2 + \ \ \left(K_{RyR}\right)^2\right)} \tag{A.5.14}$$

$$\beta^- = \frac{\emptyset_R}{t_R} \tag{A.5.15}$$

$$\mu_{oc}^+ = \frac{(C_{oc})^2 + c\left(K_{RyR}\right)^2}{\tau_R\left((C_{oc})^2 + \ \ \left(K_{RyR}\right)^2\right)} \tag{A.5.16}$$

$$\mu_{cc}^+ = \frac{([Ca^{2+}]_i)^2 + c\left(K_{RyR}\right)^2}{\tau_R\left(([Ca^{2+}]_i)^2 + \ \ \left(K_{RyR}\right)^2\right)} \tag{A.5.17}$$

$$\mu_{oc}^- = \frac{\theta_R d\left((C_{oc})^2 + c\left(K_{RyR}\right)^2\right)}{\tau_R\left(d(C_{oc})^2 + \ \ c\left(K_{RyR}\right)^2\right)} \tag{A.5.18}$$

$$\mu_{cc}^- = \frac{\theta_R d\left(([Ca^{2+}]_i)^2 + c\left(K_{RyR}\right)^2\right)}{\tau_R\left(d([Ca^{2+}]_i)^2 + \ \ c\left(K_{RyR}\right)^2\right)} \tag{A.5.19}$$

5.5. Conditional probabilities of the combined states of the calcium release unit

$$P(y_{oc}|z_1) = \frac{\alpha^+\beta^-(\alpha^+ + \alpha^- + \beta^- + \beta_{cc}^+)}{(\alpha^+ + \alpha^-)((\alpha^- + \beta^- + \beta_{oc}^+)(\beta^- + \beta_{cc}^+) + \alpha^+(\beta^- + \beta_{oc}^+))} \quad \text{(A.5.20)}$$

$$P(y_{co}|z_1) = \frac{\alpha^+\beta_{cc}^+(\alpha^- + \beta^- + \beta_{oc}^+) + \beta_{oc}^+\alpha^+}{(\alpha^+ + \alpha^-)((\alpha^- + \beta^- + \beta_{oc}^+)(\beta^- + \beta_{cc}^+) + \alpha^+(\beta^- + \beta_{oc}^+))} \quad \text{(A.5.21)}$$

$$P(y_{oo}|z_1) = \frac{\alpha^+\beta_{oc}^+(\alpha^+ + \beta^- + \beta_{cc}^+) + \beta_{cc}^+\alpha^-}{(\alpha^+ + \alpha^-)((\alpha^- + \beta^- + \beta_{oc}^+)(\beta^- + \beta_{cc}^+) + \alpha^+(\beta^- + \beta_{oc}^+))} \quad \text{(A.5.22)}$$

$$P(y_{cc}|z_1) = \frac{\alpha^-\beta^-(\alpha^+ + \alpha^- + \beta^- + \beta_{oc}^+)}{(\alpha^+ + \alpha^-)((\alpha^- + \beta^- + \beta_{oc}^+)(\beta^- + \beta_{cc}^+) + \alpha^+(\beta^- + \beta_{oc}^+))} \quad \text{(A.5.23)}$$

$$P(y_{oi}|z_2) = \frac{\alpha^+}{\alpha^+ + \alpha^-} \quad \text{(A.5.24)}$$

$$P(y_{ci}|z_2) = \frac{\alpha^-}{\alpha^+ + \alpha^-} \quad \text{(A.5.25)}$$

$$P(y_{ic}|z_3) = \frac{\beta^-}{\beta_{cc}^+ + \beta^-} \quad \text{(A.5.26)}$$

$$P(y_{io}|z_3) = \frac{\beta_{cc}^+}{\beta_{cc}^+ + \beta^-} \quad \text{(A.5.27)}$$

$$P(y_{io}|z_3) = \frac{\beta_{cc}^+}{\beta_{cc}^+ + \beta^-} \quad \text{(A.5.28)}$$

5.6. Transition rates between the combined states of the calcium release unit

$$r_1 = P(y_{oc}|z_1)\mu_{oc}^+ + P(y_{cc}|z_1)\mu_{cc}^+ \quad \text{(A.5.29)}$$

$$r_2 = \frac{\alpha^+\mu_{oc}^- + \alpha^-\mu_{cc}^-}{\alpha^+ + \alpha^-} \quad \text{(A.5.30)}$$

$$r_3 = \frac{\beta^- \mu_{cc}^+}{\beta_{cc}^+ + \beta^-} \tag{A.5.31}$$

$$r_4 = \mu_{cc}^- \tag{A.5.32}$$

$$r_5 = P(y_{co}|z_1)\epsilon_{co}^+ + P(y_{cc}|z_1)\epsilon_{cc}^+ \tag{A.5.33}$$

$$r_6 = \epsilon^- \tag{A.5.34}$$

$$r_7 = \frac{\alpha^- \epsilon_{cc}^+}{\alpha^+ + \alpha^-} \tag{A.5.35}$$

$$r_8 = \epsilon^- \tag{A.5.36}$$

5.7. Calcium fluxes

$$J_{R,co} = J_R \frac{[Ca^{2+}]_{SR} - [Ca^{2+}]_i}{1 + \frac{J_R}{g_D}} \tag{A.5.37}$$

$$J_{R,oo} = J_R \frac{\left([Ca^{2+}]_{SR} - [Ca^{2+}]_i + \frac{J_L}{g_D} \cdot \frac{\delta V}{1 - e^{-\delta V}} ([Ca^{2+}]_{SR} - [Ca^{2+}]_e e^{-\delta V})\right)}{1 + \frac{J_R}{g_D} + \frac{J_L}{g_D} \cdot \frac{\delta V}{1 - e^{-\delta V}}} \tag{A.5.38}$$

$$J_{L,oc} = J_L \frac{\delta V}{1 - e^{-\delta V}} \cdot \frac{\left([Ca^{2+}]_e e^{-\delta V} - [Ca^{2+}]_i\right)}{1 + \frac{J_L}{g_D} \cdot \frac{\delta V}{1 - e^{-\delta V}}} \tag{A.5.39}$$

$$J_{L,oo} = J_L \frac{\delta V}{1 - e^{-\delta V}} \cdot \frac{\left([Ca^{2+}]_e e^{-\delta V} - [Ca^{2+}]_i + \frac{J_R}{g_D} ([Ca^{2+}]_e e^{-\delta V} - [Ca^{2+}]_{SR})\right)}{1 + \frac{J_R}{g_D} + \frac{J_L}{g_D} \frac{\delta V}{1 - e^{-\delta V}}} \tag{A.5.40}$$

5.8. Calcium buffering

$$I_{TRPN} = 2V_{myo}F\{k^{-}{}_{TRPN}([B]_{TRPN} - [TRPN]) - k^{+}{}_{TRPN}[TRPN][Ca^{2+}]_i\} \qquad \text{(A.5.41)}$$

$$\beta\_CMDN = \left(1 + \frac{K_{CMDN}[B]_{CMDN}}{(K_{CMDN} + [Ca^{2+}]_i)^2} + \frac{K_m^{EGTA}[EGTA]_{tot}}{(K_m^{EGTA} + [Ca^{2+}]_i)^2}\right)^{-1} \qquad \text{(A.5.42)}$$

5.9. Calcium release unit

$$\frac{dz_1}{dt} = -(r_1 + r_5)z_1 + r_2 z_2 + r_6 z_3 \qquad \text{(A.5.43)}$$

$$\frac{dz_2}{dt} = r_1 z_1 - (r_2 + r_7)z_2 + r_8(1 - z_1 - z_2 - z_3) \qquad \text{(A.5.3)}$$

$$\frac{dz_3}{dt} = r_5 z_1 - (r_6 + r_3)z_3 + r_4(1 - z_1 - z_2 - z_3) \qquad \text{(A.5.44)}$$

5.10. L-type Ca^{2+} current

$$I_{LCC} = \frac{N}{V_{myo}}\left((J_{L,oo}P(y_{oo}|z_1) + J_{L,oc}P(y_{oc}|z_1))z_1 + \frac{J_{L,oc}\alpha^+}{\alpha^+ + \alpha^-}z_2\right)(-2 \times V_{myo\_\mu l} \times F) \qquad \text{(A.5.45)}$$

5.11. Ryanodine receptor

$$I_{RyR} = \frac{N}{V_{myo}}\left((J_{R,oo}P(y_{oo}|z_1) + J_{R,co}P(y_{co}|z_1))z_1 + \frac{J_{R,co}\beta_{cc}^+}{\beta_{cc}^+ + \beta^-}z_3\right) \qquad \text{(A.5.46)}$$

5.12. SR Ca^{2+} pump current

$$I_{SERCA} = g_{SERCA}\frac{[Ca^{2+}]_i^2}{K_{SERCA}^2 + [Ca^{2+}]_i^2} \qquad \text{(A.5.47)}$$

5.13. Sarcoplasmic Ca^{2+} pump current

$$I_{pCa} = \frac{g_{pCa}[\mathrm{Ca}^{2+}]_\mathrm{i}}{[\mathrm{Ca}^{2+}]_\mathrm{i} + K_{m,pCa}} \left(2 \times V_{myo\_\mu l} \times F\right) \tag{A.5.48}$$

5.14. Na^{+}-Ca^{2+} exchanger current

$$I_{NCX} = g_{NCX} \frac{e^{\eta VF/RT}[Na^{+}]_i^3[Ca^{2+}]_e - e^{(\eta-1)VF/RT}[Na^{+}]_e^3[Ca^{2+}]_i}{\left(K_{m,Na}^3 + [Na^{+}]_e^3\right)\left([Ca^{2+}]_e + K_{m,Ca}\right)\left(1 + k_{sat}e^{(\eta-1)VF/RT}\right)} \tag{A.5.49}$$

5.15. Background Ca^{2+} current

$$I_{BCa} = g_{BCa}(V - E_{Ca})\left(-2 \times V_{myo\_\mu l} \times F\right) \tag{A.5.50}$$

Table A.1. Physical constants and geometry

Parameter	Definition	Value
F	Faraday's constant	96.487 kC·mol^{-1}
T	Temperature	295 K
R	Universal gas constant	8.3145 J·mol^{-1}·K^{-1}
V_{myo}	Volume of myoplasm	25850 µm^3
V_{SR}	Volume of SR	2098 µm^3
$V_{myo\_\mu l}$		25.85 pL
$V_{SR\_\mu l}$		2.098 pL
$[Na^+]_o$	Extracellular Na^+ concentration	145 mmol·L^{-1}
$[K^+]_o$	Intracellular K^+ concentration	5.4 mmol·L^{-1}
$[Ca^{2+}]_o$	Extracellular Ca^{2+} concentration	1.2 mmol·L^{-1}

Table A.2. Membrane current parameters

Parameter	Definition	Value
Cm	Total membrane capacitance	100 pF
g_{Na}	Maximum conductance for I_{Na}	0.8 µS
g_t	Maximum conductance for I_t	17.5 nS
g_{ss}	Maximum conductance for I_{ss}	0.7 nS
g_{K1}	Maximum conductance for I_{K1}	24 nS
g_{BNa}	Maximum conductance for I_{BNa}	80.15 pS
g_{BK}	Maximum conductance for I_{BK}	138 pS
g_f	Maximum conductance for I_f	145 pS
$I_{NaK,max}$	Maximum I_{NaK}	95 pA
$K_{m,Na}$	Half-maximum Na^+ binding constant for I_{NaK}	10 mol·L^{-1}
$K_{m,K}$	Half-maximum K^+ binding constant for I_{NaK}	1.5 mol·L^{-1}

Table A.3. Ca^{2+} handling parameters

Parameter	Definition	Value
g_D	Calcium flux rate from dyadic space to cytosol	65 µm^3·s^{-1}
J_R	Permeability of single RYR	20 µm^3·s^{-1}
J_L	Permeability of single LCC	0.913 µm^3·s^{-1}
N	Number of release units	50000
VL	Potential when half LCC open	-15 mV
ΔV_L	Width of opening potentials	7 mV
ϕ_L	Proportion of time closed in open mode	2.35
t_L	Time switching between C and O states	1 ms
t_R	Time switching between C and O states	1.17 * t_L ms
τ_L	Inactivation time	650 ms
τ_R	Inactivation time	2.43 ms
ϕ_R	Proportion of time closed in open mode	0.05
θ_R	Reciprocal of proportion of time inactivated in open mode	0.012
K_{RyR}	Half concentration of activation	41 µmol·L^{-1}
K_L	Concentration at inactivation	0.22 µmol·L^{-1}
a		0.0625
b		14
c	Biasing to make inactivation a function of [Ca^{2+}]$_{ds}$	0.01
d	Biasing to make inactivation a function of [Ca^{2+}]$_{ds}$	100
K_{mNa}	Sodium half saturation of NCX	87.5 mmol·L^{-1}
K_{mCa}	Calcium half saturation of NCX	1.38 mmol·L^{-1}
η	Voltage dependence of NCX control	0.35
k_{sat}	Low potential saturation factor of NCX	0.1
g_{NCX}	Pump rate of NCX	38.5 µmol·L^{-1}·s^{-1}
g_{SERCA}	Maximum pump rate of SERCA	0.45 µmol·L^{-1}·s^{-1}
K_{SERCA}	Half saturation of SERCA	0.5 µmol·L^{-1}
g_{pCa}	Maximum I_{pCa}	0.7 µS·s^{-1}
K_{pCa}	Half saturation of sarcolemmal pump	0.5 µmol·L^{-1}
g_{BCa}	Maximum conductance for I_{BCa}	26.875 µmol·L^{-1}·V^{-1}·s^{-1}
$g_{SR,l}$	Rate of leak from SR to cytosol	0.018951 s^{-1}
$[B]_{CMDN}$	Total cytosolic calmodulin concentration	0.05 mmol·L^{-1}
$[K]_{CMDN}$	Half saturation constant of calmodulin	2.382 µmol·L^{-1}
k^-_{TRPN}	Dissociation rate of [Ca^{2+}] to troponin	0.045 s^{-1}
k^+_{TRPN}	Binding rate of [Ca^{2+}] to troponin	40 mmol·L^{-1}·s^{-1}
$[B]_{TRPN}$	Total cytosolic troponin concentration	0.07 mmol·L^{-1}

Table A.4. Initial conditions for state variables

Variable-	Definition	Initial value
m	I_{Na} activation gating variable	0.0054828
h	I_{Na} fast inactivation gating variable	0.6095126
j	I_{Na} slow inactivation gating variable	0.60876276
r	I_t activation gating variable	0.002542
s	I_t fast inactivation gating variable	0.8823
s_{slow}	I_t slow inactivation gating variable	0.42756
r_{ss}	I_{ss} activation gating variable	0.002907171
s_{ss}	I_{ss} inactivation gating variable	0.3142767
y	inactivation gating variable	$3.578708e^{-3}$
z_1		0.9886
z_2		0.008873
z_3		0.002366
V	Membrane potential	-80 mV
$[Ca^{2+}]_{SR}$	SR Ca^{2+} concentration	721.96 $\mu mol \cdot L^{-1}$
[TRPN]	Intracellular troponin concentration	63.6364 $\mu mol \cdot L^{-1}$
$[Na^+]_i$	Intracellular Na^+ concentration	11.28 $mmol \cdot L^{-1}$
$[K^+]_i$	Intracellular K^+ concentration	138.7225 $mmol \cdot L^{-1}$
$[Ca^{2+}]_i$	Intracellular Ca^{2+} concentration	0.11423 $\mu mol \cdot L^{-1}$

Appendix B

CellML Models

The mathematical models presented in this thesis have been encoded in the CellML format. More information regarding CellML is available at: http://cellml.org/. The models used to generate the results presented in Chapter 5 are available in the Physiome Model Repository in the workspace https://models.physiomeproject.org/workspace/25c. I briefly describe here the models available in that workspace

1. *Membrane current and subcellular models*

As presented in Chapter 5, each of the currents and subcellular components in the electrophysiology cell model were implemented and tested individually. Within the workspace above, the following model files correspond to each of the currents presented in Section 5.1.2. The latest revision of each of the models in the table below can be reached by visiting the location https://models.physiomeproject.org/workspace/25c in your web browser and navigating to the corresponding file (Table B.1).

Table B.1. CellML model files for each the currents

Current or subcellular component	**CellML model file**
5.1.2.1 Na$^+$ current (I_{Na}) module	INa_Pandit.cellml
5.1.2.2 Ca^{2+}-independent transient outward K$^+$ current (I_{to}) module	Ito_Pandit.cellml
5.1.2.3. Steady-state outward K$^+$ current (I_{ss}) module	Iss_Pandit.cellml
5.1.2.4. Inward rectifier K$^+$ current (I_{K1}) module	IK1_Pandit.cellml
5.1.2.5. Hyperpolarization-activated current (I_f) module	If_Pandit.cellml
5.1.2.6. Background Na$^+$ current (I_{BNa}) module	IBNa_Pandit.cellml
5.1.2.7. Background K$^+$ current (I_{BK}) module	IBK_Pandit.cellml
5.1.2.8. Na$^+$/K$^+$ pump current (I_{NaK}) module	INaK_Pandit.cellml
5.1.2.9. Ca^{2+} release unit (CaRU) module	CaRU_Hinch.cellml
5.1.2.10. Ca^{2+} pump current	
• SR Ca^{2+} pump, SERCA current (I_{SERCA}) module	ISERCA_Hinch.cellml
• Sarcolemmal Ca^{2+} pump current (I_{pCa}) module	ICaPump_Hinch.cellml
5.1.2.11. Na$^+$-Ca^{2+} exchanger current (I_{NCX}) module	INCX_Hinch.cellml
5.1.2.12. Background Ca^{2+} current (I_{BCa}) module	IBCa_Hinch.cellml
5.1.2.13 Calmodulin (β_CMDN) module	Icalmodulin_new.cellml
5.1.2.14 Troponin module	Itroponin_NSH.cellml
5.1.2.15 Tropomyosin module	Itropomyosin_NSH.cellml
5.1.2.16 Crossbridge module	CrossBridge_NSH.cellml

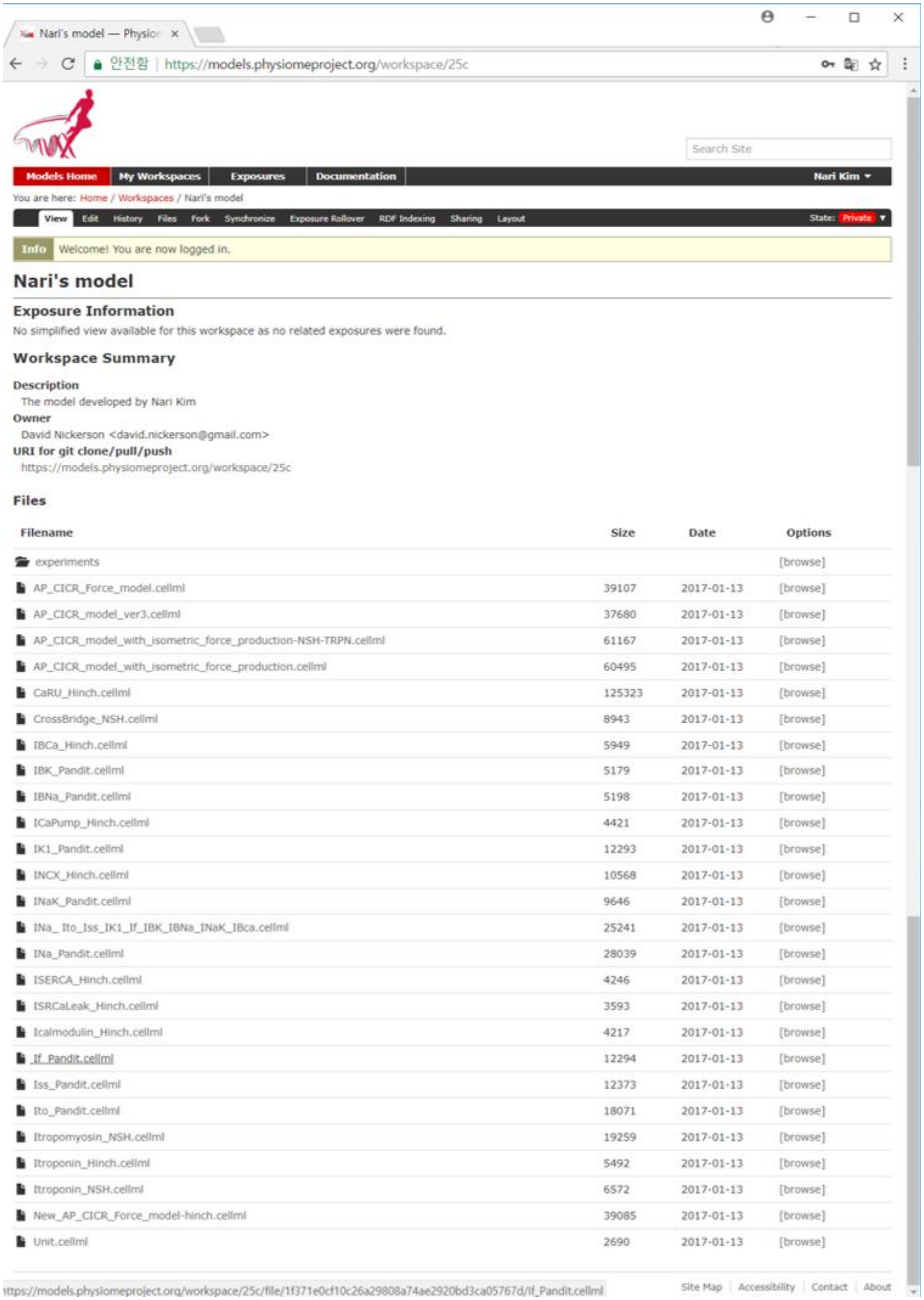

Welcome! You are now logged in.

Nari's model

Exposure Information

No simplified view available for this workspace as no related exposures were found.

Workspace Summary

Description

The model developed by Nari Kim

Owner

David Nickerson <david.nickerson@gmail.com>

URI for git clone/pull/push

https://models.physiomeproject.org/workspace/25c

Files

Filename	Size	Date	Options
experiments			[browse]
AP_CICR_Force_model.cellml	39107	2017-01-13	[browse]
AP_CICR_model_ver3.cellml	37680	2017-01-13	[browse]
AP_CICR_model_with_isometric_force_production-NSH-TRPN.cellml	61167	2017-01-13	[browse]
AP_CICR_model_with_isometric_force_production.cellml	60495	2017-01-13	[browse]
CaRU_Hinch.cellml	125323	2017-01-13	[browse]
CrossBridge_NSH.cellml	8943	2017-01-13	[browse]
IBCa_Hinch.cellml	5949	2017-01-13	[browse]
IBK_Pandit.cellml	5179	2017-01-13	[browse]
IBNa_Pandit.cellml	5198	2017-01-13	[browse]
ICaPump_Hinch.cellml	4421	2017-01-13	[browse]
IK1_Pandit.cellml	12293	2017-01-13	[browse]
INCX_Hinch.cellml	10568	2017-01-13	[browse]
INaK_Pandit.cellml	9646	2017-01-13	[browse]
INa_ Ito_Iss_IK1_If_IBK_IBNa_INaK_IBca.cellml	25241	2017-01-13	[browse]
INa_Pandit.cellml	28039	2017-01-13	[browse]
ISERCA_Hinch.cellml	4246	2017-01-13	[browse]
ISRCaLeak_Hinch.cellml	3593	2017-01-13	[browse]
Icalmodulin_Hinch.cellml	4217	2017-01-13	[browse]
If_Pandit.cellml	12294	2017-01-13	[browse]
Iss_Pandit.cellml	12373	2017-01-13	[browse]
Ito_Pandit.cellml	18071	2017-01-13	[browse]
Itropomyosin_NSH.cellml	19259	2017-01-13	[browse]
Itroponin_Hinch.cellml	5492	2017-01-13	[browse]
Itroponin_NSH.cellml	6572	2017-01-13	[browse]
New_AP_CICR_Force_model-hinch.cellml	39085	2017-01-13	[browse]
Unit.cellml	2690	2017-01-13	[browse]

ttps://models.physiomeproject.org/workspace/25c/file/1f371e0cf10c26a29808a74ae2920bd3ca05767d/If_Pandit.cellml

2. *Whole cell model*

Sections 5.1.3 and 5.2 present the whole cell model developed in this work. The corresponding CellML model (AP_CICR_Force_model.cellml) is defined as the collection of the sub-models given in the table above (Table B.1) with the addition of the transmembrane voltage equation (Eq 5-1), the stimulus current, and the intracellular mass conservation equations (Eq 2-7).

CellML codes of AP_CICR_Force model including ODEs is available in the Physiome Model Repository in the workspace https://models.physiomeproject.org/workspace/25c.

References

Afzal, N., and Dhalla, N.S. (1992). Differential changes in left and right ventricular SR calcium transport in congestive heart failure. Am J Physiol *262*, H868-874.

Agus, Z.S., Dukes, I.D., and Morad, M. (1991). Divalent cations modulate the transient outward current in rat ventricular myocytes. Am J Physiol *261*, C310-318.

Alpert, N.R., Hamrell, B.B., and Halpern, W. (1974). Mechanical and biochemical correlates of cardiac hypertrophy. Circ Res *35*, suppl II:71-82.

Alpert, N.R., Leavitt, B.J., Ittleman, F.P., Hasenfuss, G., Pieske, B., and Mulieri, L.A. (1998). A mechanistic analysis of the force-frequency relation in non-failing and progressively failing human myocardium. Basic Res Cardiol *93 Suppl 1*, 23-32.

Alpert, N.R., and Mulieri, L.A. (1982). Increased myothermal economy of isometric force generation in compensated cardiac hypertrophy induced by pulmonary artery constriction in the rabbit. A characterization of heat liberation in normal and hypertrophied right ventricular papillary muscles. Circ Res *50*, 491-500.

Alter, P., Rupp, H., Stoll, F., Adams, P., Figiel, J.H., Klose, K.J., Rominger, M.B., and Maisch, B. (2012). Increased end diastolic wall stress precedes left ventricular hypertrophy in dilative heart failure--use of the volume-based wall stress index. Int J Cardiol *157*, 233-238.

Anversa, P., Beghi, C., Kikkawa, Y., and Olivetti, G. (1986). Myocardial infarction in rats. Infarct size, myocyte hypertrophy, and capillary growth. Circ Res *58*, 26-37.

Apkon, M., and Nerbonne, J.M. (1991). Characterization of two distinct depolarization-activated K^+ currents in isolated adult rat ventricular myocytes. J Gen Physiol *97*, 973-1011.

Barclay, C.J. (2005). Modelling diffusive O_2 supply to isolated preparations of mammalian skeletal and cardiac muscle. J Muscle Res Cell Motil *26*, 225-235.

Basile-Filho, A., Campos, A.C., Esteves, S.C., Bordin, S., and Mantovani, M. (1991). Influence of subacute starvation on cardiac response to isoproterenol in rats. Nutrition *7*, 280-282.

Beeler, G.W., and Reuter, H. (1977). Reconstruction of the action potential of ventricular myocardial fibres. J Physiol *268*, 177-210.

Belin, R.J., Sumandea, M.P., Sievert, G.A., Harvey, L.A., Geenen, D.L., Solaro, R.J., and de Tombe, P.P. (2011). Interventricular differences in myofilament function in experimental congestive heart failure. Pflugers Arch *462*, 795-809.

Berger, F., Borchard, U., Hafner, D., and Weis, T.M. (1998). Different inhibition patterns of tedisamil for fast and slowly inactivating transient outward current in rat ventricular myocytes. Naunyn Schmiedebergs Arch Pharmacol *357*, 291-298.

Bers, D.M. (2000). Calcium fluxes involved in control of cardiac myocyte contraction. Circ Res *87*, 275-281.

Bers, D.M. (2002). Cardiac excitation-contraction coupling. Nature *415*, 198-205.

Bhargava, V., Shabetai, R., Mathiasen, R.A., Dalton, N., Hunter, J.J., and Ross, J., Jr. (1998). Loss of adrenergic control of the force-frequency relation in heart failure secondary to idiopathic or ischemic cardiomyopathy. Am J Cardiol *81*, 1130-1137.

Biesiadecki, B.J., Davis, J.P., Ziolo, M.T., and Janssen, P.M. (2014). Tri-modal regulation of cardiac muscle relaxation; intracellular calcium decline, thin filament deactivation, and cross-bridge cycling kinetics. Biophys Rev *6*, 273-289.

Blaustein, M.P., and Lederer, W.J. (1999). Sodium/calcium exchange: its physiological implications. Physiol Rev *79*, 763-854.

Bleasdale, R.A., and Frenneaux, M.P. (2002). Prognostic importance of right ventricular dysfunction. Heart *88*, 323-324.

Bode, E.F., Briston, S.J., Overend, C.L., O'Neill, S.C., Trafford, A.W., and Eisner, D.A. (2011). Changes of SERCA activity have only modest effects on sarcoplasmic reticulum Ca^{2+} content in rat ventricular myocytes. J Physiol *589*, 4723-4729.

Bondarenko, V.E., Bett, G.C., and Rasmusson, R.L. (2004). A model of graded calcium release and *L*-type Ca^{2+} channel inactivation in cardiac muscle. Am J Physiol Heart Circ Physiol *286*, H1154-1169.

Borbely, A., Falcao-Pires, I., van Heerebeek, L., Hamdani, N., Edes, I., Gavina, C., Leite-Moreira, A.F., Bronzwaer, J.G., Papp, Z., van der Velden, J.*, et al.* (2009). Hypophosphorylation of the Stiff N2B titin isoform raises cardiomyocyte resting tension in failing human myocardium. Circ Res *104*, 780-786.

Borzak, S., Murphy, S., and Marsh, J.D. (1991). Mechanisms of rate staircase in rat ventricular cells. Am J Physiol *260*, H884-892.

Brette, F., and Orchard, C. (2003). *T*-tubule function in mammalian cardiac myocytes. Circ Res *92*, 1182-1192.

Bristow, M.R., Minobe, W., Rasmussen, R., Larrabee, P., Skerl, L., Klein, J.W., Anderson, F.L., Murray, J., Mestroni, L., Karwande, S.V.*, et al.* (1992). Beta-adrenergic neuroeffector abnormalities in the failing human heart are produced by local rather than systemic mechanisms. J Clin Invest *89*, 803-815.

Brooks, W.W., Bing, O.H., Blaustein, A.S., and Allen, P.D. (1987). Comparison of contractile state and myosin isozymes of rat right and left ventricular myocardium. J Mol Cell Cardiol *19*, 433-440.

Buckley, N.M., Penefsky, Z.J., and Litwak, R.S. (1972). Comparative force-frequency relationships in human and other mammalian ventricular myocardium. Pflugers Arch *332*, 259-270.

Buxton, I.L., and Brunton, L.L. (1986). Alpha-adrenergic receptors on rat ventricular myocytes: characteristics and linkage to cAMP metabolism. Am J Physiol *251*, H307-313.

Cannell, M.B., Berlin, J.R., and Lederer, W.J. (1987). Effect of membrane potential changes on the calcium transient in single rat cardiac muscle cells. Science *238*, 1419-1423.

Carlsson, M., Heiberg, E., Toger, J., and Arheden, H. (2012). Quantification of left and right ventricular kinetic energy using four-dimensional intracardiac magnetic resonance imaging flow measurements. Am J Physiol Heart Circ Physiol *302*, H893-900.

Cerbai, E., Barbieri, M., and Mugelli, A. (1996). Occurrence and properties of the hyperpolarization-activated current If in ventricular myocytes from normotensive and hypertensive rats during aging. Circulation *94*, 1674-1681.

Chu, C., Thai, K., Park, K.W., Wang, P., Makwana, O., Lovett, D.H., Simpson, P.C., and Baker, A.J. (2013). Intraventricular and interventricular cellular heterogeneity of inotropic responses to alpha1-adrenergic stimulation. Am J Physiol Heart Circ Physiol *304*, H946-953.

Clark, R.B., Bouchard, R.A., Salinas-Stefanon, E., Sanchez-Chapula, J., and Giles, W.R. (1993). Heterogeneity of action potential waveforms and potassium currents in rat ventricle. Cardiovasc Res *27*, 1795-1799.

Clark, R.B., Sanchez-Chapula, J., Salinas-Stefanon, E., Duff, H.J., and Giles, W.R. (1995). Quinidine-induced open channel block of K^+ current in rat ventricle. Br J Pharmacol *115*, 335-343.

Clayton, R.H. (2001). Computational models of normal and abnormal action potential propagation in cardiac tissue: linking experimental and clinical cardiology. Physiol Meas *22*, R15-34.

Copello, J.A., Zima, A.V., Diaz-Sylvester, P.L., Fill, M., and Blatter, L.A. (2007). Ca^{2+} entry-independent effects of *L*-type Ca^{2+} channel modulators on Ca^{2+} sparks in ventricular myocytes. Am J Physiol Cell Physiol *292*, C2129-2140.

Correia Pinto, J., Henriques-Coelho, T., Roncon-Albuquerque, R., Jr., and Leite-Moreira, A.F. (2006). Differential right and left ventricular diastolic tolerance to acute afterload and NCX gene expression in Wistar rats. Physiol Res *55*, 513-526.

Danziger, R.S., Sakai, M., Lakatta, E.G., and Hansford, R.G. (1990). Interactive alpha- and beta-adrenergic actions of norepinephrine in rat cardiac myocytes. J Mol Cell Cardiol *22*, 111-123.

Dell'Italia, L.J., and Walsh, R.A. (1988a). Acute determinants of the hangout interval in the pulmonary circulation. Am Heart J *116*, 1289-1297.

Dell'Italia, L.J., and Walsh, R.A. (1988b). Right ventricular diastolic pressure-volume relations and regional dimensions during acute alterations in loading conditions. Circulation *77*, 1276-1282.

Demir, S.S., Clark, J.W., Murphey, C.R., and Giles, W.R. (1994). A mathematical model of a rabbit sinoatrial node cell. Am J Physiol *266*, C832-852.

Dhalla, N.S., Sulakhe, P.V., Lee, S.L., Singal, P.K., Varley, K.G., and Yates, J.C. (1980). Subcellular Ca^{2+} transport in different areas of dog heart. Can J Physiol Pharmacol *58*, 360-367.

Di Diego, J.M., Sun, Z.Q., and Antzelevitch, C. (1996). I_{to} and action potential notch are smaller in left vs. right canine ventricular epicardium. Am J Physiol *271*, H548-561.

Di Napoli, P., Taccardi, A.A., Grilli, A., Felaco, M., Balbone, A., Angelucci, D., Gallina, S., Calafiore, A.M., De Caterina, R., and Barsotti, A. (2003). Left ventricular wall stress as a direct correlate of cardiomyocyte apoptosis in patients with severe dilated cardiomyopathy. Am Heart J *146*, 1105-1111.

Dibb, K.M., Eisner, D.A., and Trafford, A.W. (2007). Regulation of systolic $[Ca^{2+}]_i$ and cellular Ca^{2+} flux balance in rat ventricular myocytes by SR Ca^{2+}, *L*-type Ca^{2+} current and diastolic $[Ca^{2+}]_i$. J Physiol *585*, 579-592.

Ezzaher, A., el Houda Bouanani, N., and Crozatier, B. (1992). Force-frequency relations and response to ryanodine in failing rabbit hearts. Am J Physiol *263*, H1710-1715.

Fares, N., Bois, P., Lenfant, J., and Potreau, D. (1998). Characterization of a hyperpolarization-activated current in dedifferentiated adult rat ventricular cells in primary culture. J Physiol *506 (Pt 1)*, 73-82.

Freeman, G.L., Little, W.C., and O'Rourke, R.A. (1987). Influence of heart rate on left ventricular performance in conscious dogs. Circ Res *61*, 455-464.

Fukuda, N., Wu, Y., Nair, P., and Granzier, H.L. (2005). Phosphorylation of titin modulates passive stiffness of cardiac muscle in a titin isoform-dependent manner. J Gen Physiol *125*, 257-271.

Gerdes, A.M., Moore, J.A., Hines, J.M., Kirkland, P.A., and Bishop, S.P. (1986). Regional differences in myocyte size in normal rat heart. Anat Rec *215*, 420-426.

Gillis, T.E., Marshall, C.R., Xue, X.H., Borgford, T.J., and Tibbits, G.F. (2000). Ca^{2+} binding to cardiac troponin C: effects of temperature and pH on mammalian and salmonid isoforms. Am J Physiol Regul Integr Comp Physiol *279*, R1707-1715.

Greenstein, J.L., and Winslow, R.L. (2002). An integrative model of the cardiac ventricular myocyte incorporating local control of Ca^{2+} release. Biophys J *83*, 2918-2945.

Grossman, W., Jones, D., and McLaurin, L.P. (1975). Wall stress and patterns of hypertrophy in the human left ventricle. J Clin Invest *56*, 56-64.

Haddad, F., Hunt, S.A., Rosenthal, D.N., and Murphy, D.J. (2008). Right ventricular function in cardiovascular disease, part I: Anatomy, physiology, aging, and functional assessment of the right ventricle. Circulation *117*, 1436-1448.

Han, J.C., Taberner, A.J., Kirton, R.S., Nielsen, P.M., Archer, R., Kim, N., and Loiselle, D.S. (2011). Radius-dependent decline of performance in isolated cardiac muscle does not reflect inadequacy of diffusive oxygen supply. Am J Physiol Heart Circ Physiol *300*, H1222-1236.

Han, J.C., Taberner, A.J., Kirton, R.S., Nielsen, P.M., Smith, N.P., and Loiselle, D.S. (2009). A unique micromechanocalorimeter for simultaneous measurement of heat rate and force production of cardiac trabeculae carneae. J Appl Physiol *107*, 946-951.

Hasenfuss, G., Holubarsch, C., Hermann, H.P., Astheimer, K., Pieske, B., and Just, H. (1994a). Influence of the force-frequency relationship on haemodynamics and left ventricular function in patients with non-failing hearts and in patients with dilated cardiomyopathy. Eur Heart J *15*, 164-170.

Hasenfuss, G., Reinecke, H., Studer, R., Meyer, M., Pieske, B., Holtz, J., Holubarsch, C., Posival, H., Just, H., and Drexler, H. (1994b). Relation between myocardial function and expression of sarcoplasmic reticulum Ca^{2+}-ATPase in failing and nonfailing human myocardium. Circ Res *75*, 434-442.

Hefner, L.L., Sheffield, L.T., Cobbs, G.C., and Klip, W. (1962). Relation between mural force and pressure in the left ventricle of the dog. Circ Res *11*, 654-663.

Hidalgo, C., Hudson, B., Bogomolovas, J., Zhu, Y., Anderson, B., Greaser, M., Labeit, S., and Granzier, H. (2009). PKC phosphorylation of titin's PEVK element: a novel and conserved pathway for modulating myocardial stiffness. Circ Res *105*, 631-638, 617 p following 638.

Higginbotham, M.B., Morris, K.G., Williams, R.S., McHale, P.A., Coleman, R.E., and Cobb, F.R. (1986). Regulation of stroke volume during submaximal and maximal upright exercise in normal man. Circ Res *58*, 281-291.

Hinch, R., Greenstein, J.L., Tanskanen, A.J., Xu, L., and Winslow, R.L. (2004). A simplified local control model of calcium-induced calcium release in cardiac ventricular myocytes. Biophys J *87*, 3723-3736.

Ho, S.Y. (2009). Anatomy and myoarchitecture of the left ventricular wall in normal and in disease. Eur J Echocardiogr *10*, iii3-7.

Ho, S.Y., and Nihoyannopoulos, P. (2006). Anatomy, echocardiography, and normal right ventricular dimensions. Heart *92 Suppl 1*, i2-13.

Hoch, D.H., and Rosenfeld, L.E. (1992). Tachycardias of right ventricular origin. Cardiol Clin *10*, 151-164.

Hodgkin, A.L., and Huxley, A.F. (1952). A quantitative description of membrane current and its application to conduction and excitation in nerve. J Physiol *117*, 500-544.

Holubarsch, C., Ruf, T., Goldstein, D.J., Ashton, R.C., Nickl, W., Pieske, B., Pioch, K., Ludemann, J., Wiesner, S., Hasenfuss, G.*, et al.* (1996). Existence of the Frank-Starling mechanism in the failing human heart. Investigations on the organ, tissue, and sarcomere levels. Circulation *94*, 683-689.

Hood, W.P., Jr., Rackley, C.E., and Rolett, E.L. (1968). Wall stress in the normal and hypertrophied human left ventricle. Am J Cardiol *22*, 550-558.

Huang, B., Qin, D., and El-Sherif, N. (2001). Spatial alterations of Kv channels expression and K^+ currents in post-MI remodeled rat heart. Cardiovasc Res *52*, 246-254.

Hudmon, A., Schulman, H., Kim, J., Maltez, J.M., Tsien, R.W., and Pitt, G.S. (2005). CaMKII tethers to *L*-type Ca^{2+} channels, establishing a local and dedicated integrator of Ca^{2+} signals for facilitation. J Cell Biol *171*, 537-547.

Imanaga, I. (2010). Pathological remodeling of cardiac gap junction connexin 43-With special reference to arrhythmogenesis. Pathophysiology *17*, 73-81.

Itoya, M., Mallet, R.T., Gao, Z.P., Williams, A.G., Jr., and Downey, H.F. (1996). Stability of high-energy phosphates in right ventricle: myocardial energetics during right coronary hypotension. Am J Physiol *271*, H320-328.

Jafri, M.S., Rice, J.J., and Winslow, R.L. (1998). Cardiac Ca^{2+} dynamics: the roles of ryanodine receptor adaptation and sarcoplasmic reticulum load. Biophys J *74*, 1149-1168.

Janssen, P.M., Stull, L.B., Leppo, M.K., Altschuld, R.A., and Marban, E. (2003). Selective contractile dysfunction of left, not right, ventricular myocardium in the SHHF rat. Am J Physiol Heart Circ Physiol *284*, H772-778.

Janssen, P.M., Stull, L.B., and Marban, E. (2002). Myofilament properties comprise the rate-limiting step for cardiac relaxation at body temperature in the rat. Am J Physiol Heart Circ Physiol *282*, H499-507.

Kambayashi, M., Miura, T., Oh, B.H., Rockman, H.A., Murata, K., and Ross, J., Jr. (1992). Enhancement of the force-frequency effect on myocardial contractility by adrenergic stimulation in conscious dogs. Circulation *86*, 572-580.

Kaplan, J.H. (2002). Biochemistry of Na,K-ATPase. Annu Rev Biochem *71*, 511-535.

Kaprielian, R., Sah, R., Nguyen, T., Wickenden, A.D., and Backx, P.H. (2002). Myocardial infarction in rat eliminates regional heterogeneity of AP profiles, I_{to} K^+ currents, and $[Ca^{2+}]_i$ transients. Am J Physiol Heart Circ Physiol *283*, H1157-1168.

Kass, D.A., Bronzwaer, J.G., and Paulus, W.J. (2004). What mechanisms underlie diastolic dysfunction in heart failure? Circ Res *94*, 1533-1542.

Kassiri, Z., Myers, R., Kaprielian, R., Banijamali, H.S., and Backx, P.H. (2000). Rate-dependent changes of twitch force duration in rat cardiac trabeculae: a property of the contractile system. J Physiol *524 Pt 1*, 221-231.

Keung, E.C., and Aronson, R.S. (1981). Non-uniform electrophysiological properties and electrotonic interaction in hypertrophied rat myocardium. Circ Res *49*, 150-158.

Kim, H.K., Youm, J.B., Lee, S.R., Lim, S.E., Lee, S.Y., Ko, T.H., Long le, T., Nilius, B., Won du, N., Noh, J.H.*, et al.* (2012). The angiotensin receptor blocker and PPAR-gamma agonist, telmisartan, delays inactivation of voltage-gated sodium channel in rat heart: novel mechanism of drug action. Pflugers Arch *464*, 631-643.

Kim, N., Cannell, M.B., and Hunter, P.J. (2010). Changes in the calcium current among different transmural regions contributes to action potential heterogeneity in rat heart. Prog Biophys Mol Biol *103*, 28-34.

Kondo, R.P., Dederko, D.A., Teutsch, C., Chrast, J., Catalucci, D., Chien, K.R., and Giles, W.R. (2006). Comparison of contraction and calcium handling between right and left ventricular myocytes from adult mouse heart: a role for repolarization waveform. J Physiol *571*, 131-146.

Korhonen, T., Hanninen, S.L., and Tavi, P. (2009). Model of excitation-contraction coupling of rat neonatal ventricular myocytes. Biophys J *96*, 1189-1209.

Kranias, E.G., and Solaro, R.J. (1983). Coordination of cardiac sarcoplasmic reticulum and myofibrillar function by protein phosphorylation. Fed Proc *42*, 33-38.

Krishna, A., Valderrabano, M., Palade, P.T., and Clark, W.J., Jr. (2012). Multiphysics model of a rat ventricular myocyte: a voltage-clamp study. Theor Biol Med Model *9*, 48.

Kruger, M., Kotter, S., Grutzner, A., Lang, P., Andresen, C., Redfield, M.M., Butt, E., dos Remedios, C.G., and Linke, W.A. (2009). Protein kinase G modulates human myocardial passive stiffness by phosphorylation of the titin springs. Circ Res *104*, 87-94.

Kruger, M., and Linke, W.A. (2006). Protein kinase-A phosphorylates titin in human heart muscle and reduces myofibrillar passive tension. J Muscle Res Cell Motil *27*, 435-444.

Kushnir, A., Shan, J., Betzenhauser, M.J., Reiken, S., and Marks, A.R. (2010). Role of CaMKIIdelta phosphorylation of the cardiac ryanodine receptor in the force frequency relationship and heart failure. Proc Natl Acad Sci U S A *107*, 10274-10279.

Layland, J., and Kentish, J.C. (1999). Positive force- and $[Ca^{2+}]_i$-frequency relationships in rat ventricular trabeculae at physiological frequencies. Am J Physiol *276*, H9-H18.

Lee, H.C., Lu, T., Weintraub, N.L., VanRollins, M., Spector, A.A., and Shibata, E.F. (1999). Effects of epoxyeicosatrienoic acids on the cardiac sodium channels in isolated rat ventricular myocytes. J Physiol *519 Pt 1*, 153-168.

Li, G.R., Feng, J., Yue, L., and Carrier, M. (1998). Transmural heterogeneity of action potentials and Ito1 in myocytes isolated from the human right ventricle. Am J Physiol *275*, H369-377.

Li, Q., Cui, N., Du, Y., Ma, H., and Zhang, Y. (2013). Anandamide reduces intracellular Ca^{2+} concentration through suppression of Na^+/Ca^{2+} exchanger current in rat cardiac myocytes. PLoS One *8*, e63386.

Lindemann, J.P., Jones, L.R., Hathaway, D.R., Henry, B.G., and Watanabe, A.M. (1983). beta-Adrenergic stimulation of phospholamban phosphorylation and Ca^{2+}-ATPase activity in guinea pig ventricles. J Biol Chem *258*, 464-471.

Linz, K.W., and Meyer, R. (2000). Profile and kinetics of L-type calcium current during the cardiac ventricular action potential compared in guinea-pigs, rats and rabbits. Pflugers Arch *439*, 588-599.

Lopatin, A.N., and Nichols, C.G. (2001). Inward rectifiers in the heart: an update on I_{K1}. J Mol Cell Cardiol *33*, 625-638.

Luo, C.H., and Rudy, Y. (1991). A model of the ventricular cardiac action potential. Depolarization, repolarization, and their interaction. Circ Res *68*, 1501-1526.

Luo, C.H., and Rudy, Y. (1994). A dynamic model of the cardiac ventricular action potential. I. Simulations of ionic currents and concentration changes. Circ Res *74*, 1071-1096.

Lytton, J., Westlin, M., Burk, S.E., Shull, G.E., and MacLennan, D.H. (1992). Functional comparisons between isoforms of the sarcoplasmic or endoplasmic reticulum family of calcium pumps. J Biol Chem *267*, 14483-14489.

Mackiewicz, U., and Lewartowski, B. (2006). Temperature dependent contribution of Ca^{2+} transporters to relaxation in cardiac myocytes: important role of sarcolemmal Ca^{2+}-ATPase. J Physiol Pharmacol *57*, 3-15.

Martin, C.A., Siedlecka, U., Kemmerich, K., Lawrence, J., Cartledge, J., Guzadhur, L., Brice, N., Grace, A.A., Schwiening, C., Terracciano, C.M.*, et al.* (2012). Reduced Na^+ and higher K^+ channel expression and function contribute to right ventricular origin of arrhythmias in Scn5a+/- mice. Open Biol *2*, 120072.

McAllister, R.E., Noble, D., and Tsien, R.W. (1975). Reconstruction of the electrical activity of cardiac Purkinje fibres. J Physiol *251*, 1-59.

McCubbin, W.D., Hincke, M.T., and Kay, C.M. (1980). The effect of temperature on some calcium-binding properties of troponin C and calmodulin. Can J Biochem *58*, 683-691.

McMahon, W.S., Mukherjee, R., Gillette, P.C., Crawford, F.A., and Spinale, F.G. (1996). Right and left ventricular geometry and myocyte contractile processes with dilated cardiomyopathy: myocyte growth and beta-adrenergic responsiveness. Cardiovasc Res *31*, 314-323.

Milani-Nejad, N., and Janssen, P.M. (2014). Small and large animal models in cardiac contraction research: advantages and disadvantages. Pharmacol Ther *141*, 235-249.

Miller, A.K., Marsh, J., Reeve, A., Garny, A., Britten, R., Halstead, M., Cooper, J., Nickerson, D.P., and Nielsen, P.F. (2010). An overview of the CellML API and its implementation. BMC Bioinformatics *11*, 178.

Mirsky, I. (1969). Left ventricular stresses in the intact human heart. Biophys J *9*, 189-208.

Molina, C.E., Johnson, D.M., Mehel, H., Spatjens, R.L., Mika, D., Algalarrondo, V., Slimane, Z.H., Lechene, P., Abi-Gerges, N., van der Linde, H.J.*, et al.* (2014). Interventricular differences in beta-adrenergic responses in the canine heart: role of phosphodiesterases. J Am Heart Assoc *3*, e000858.

Mulieri, L.A., Hasenfuss, G., Ittleman, F., Blanchard, E.M., and Alpert, N.R. (1989). Protection of human left ventricular myocardium from cutting injury with 2,3-butanedione monoxime. Circ Res *65*, 1441-1449.

Munch, G., Bolck, B., Karczewski, P., and Schwinger, R.H. (2002). Evidence for calcineurin-mediated regulation of SERCA 2a activity in human myocardium. J Mol Cell Cardiol *34*, 321-334.

Nagueh, S.F., Shah, G., Wu, Y., Torre-Amione, G., King, N.M., Lahmers, S., Witt, C.C., Becker, K., Labeit, S., and Granzier, H.L. (2004). Altered titin expression, myocardial stiffness, and left ventricular function in patients with dilated cardiomyopathy. Circulation *110*, 155-162.

Nerbonne, J.M., Nichols, C.G., Schwarz, T.L., and Escande, D. (2001). Genetic manipulation of cardiac K^+ channel function in mice: what have we learned, and where do we go from here? Circ Res *89*, 944-956.

Niederer, S.A., Hunter, P.J., and Smith, N.P. (2006). A quantitative analysis of cardiac myocyte relaxation: a simulation study. Biophys J *90*, 1697-1722.

Niwa, N., and Nerbonne, J.M. (2010). Molecular determinants of cardiac transient outward potassium current (I_{to}) expression and regulation. J Mol Cell Cardiol *48*, 12-25.

Noble, D. (1962). A modification of the Hodgkin--Huxley equations applicable to Purkinje fibre action and pace-maker potentials. J Physiol *160*, 317-352.

Olivetti, G., Ricci, R., and Anversa, P. (1987). Hyperplasia of myocyte nuclei in long-term cardiac hypertrophy in rats. J Clin Invest *80*, 1818-1821.

Ottolia, M., Torres, N., Bridge, J.H., Philipson, K.D., and Goldhaber, J.I. (2013). Na/Ca exchange and contraction of the heart. J Mol Cell Cardiol *61*, 28-33.

Oudit, G.Y., Kassiri, Z., Sah, R., Ramirez, R.J., Zobel, C., and Backx, P.H. (2001). The molecular physiology of the cardiac transient outward potassium current (I_{to}) in normal and diseased myocardium. J Mol Cell Cardiol *33*, 851-872.

Palakodeti, V., Oh, S., Oh, B.H., Mao, L., Hongo, M., Peterson, K.L., and Ross, J., Jr. (1997). Force-frequency effect is a powerful determinant of myocardial contractility in the mouse. Am J Physiol *273*, H1283-1290.

Pandit, S.V., Clark, R.B., Giles, W.R., and Demir, S.S. (2001). A mathematical model of action potential heterogeneity in adult rat left ventricular myocytes. Biophys J *81*, 3029-3051.

Pandit, S.V., Giles, W.R., and Demir, S.S. (2003). A mathematical model of the electrophysiological alterations in rat ventricular myocytes in type-I diabetes. Biophys J *84*, 832-841.

Peiper, U., Laven, R., and Ehl, M. (1975). Force velocity relationships in vascular smooth muscle. The influence of temperature. Pflugers Arch *356*, 33-45.

Perreault, C.L., Bing, O.H., Brooks, W.W., Ransil, B.J., and Morgan, J.P. (1990). Differential effects of cardiac hypertrophy and failure on right versus left ventricular calcium activation. Circ Res *67*, 707-712.

Piacentino, V., 3rd, Dipla, K., Gaughan, J.P., and Houser, S.R. (2000). Voltage-dependent Ca^{2+} release from the SR of feline ventricular myocytes is explained by Ca^{2+}-induced Ca^{2+} release. J Physiol *523 Pt 3*, 533-548.

Piot, C., LeMaire, S.A., Albat, B., Seguin, J., Nargeot, J., and Richard, S. (1996). High frequency-induced upregulation of human cardiac calcium currents. Circulation *93*, 120-128.

Pitt, G.S., Zuhlke, R.D., Hudmon, A., Schulman, H., Reuter, H., and Tsien, R.W. (2001). Molecular basis of calmodulin tethering and Ca Ca^{2+}-dependent inactivation of *L*-type Ca^{2+} channels. J Biol Chem *276*, 30794-30802.

Puglisi, J.L., Bassani, R.A., Bassani, J.W., Amin, J.N., and Bers, D.M. (1996). Temperature and relative contributions of Ca transport systems in cardiac myocyte relaxation. Am J Physiol *270*, H1772-1778.

Rayment, I., Holden, H.M., Whittaker, M., Yohn, C.B., Lorenz, M., Holmes, K.C., and Milligan, R.A. (1993). Structure of the actin-myosin complex and its implications for muscle contraction. Science *261*, 58-65.

Reuter, H. (1967). The dependence of slow inward current in Purkinje fibres on the extracellular calcium-concentration. J Physiol *192*, 479-492.

Richard, S., Leclercq, F., Lemaire, S., Piot, C., and Nargeot, J. (1998). Ca^{2+} currents in compensated hypertrophy and heart failure. Cardiovasc Res *37*, 300-311.

Rodriguez, E.K., Hunter, W.C., Royce, M.J., Leppo, M.K., Douglas, A.S., and Weisman, H.F. (1992). A method to reconstruct myocardial sarcomere lengths and orientations at transmural sites in beating canine hearts. Am J Physiol *263*, H293-306.

Roof, S.R., Shannon, T.R., Janssen, P.M., and Ziolo, M.T. (2011). Effects of increased systolic Ca^{2+} and phospholamban phosphorylation during beta-adrenergic stimulation on Ca^{2+} transient kinetics in cardiac myocytes. Am J Physiol Heart Circ Physiol *301*, H1570-1578.

Ross, J., Jr., Miura, T., Kambayashi, M., Eising, G.P., and Ryu, K.H. (1995). Adrenergic control of the force-frequency relation. Circulation *92*, 2327-2332.

Rouleau, J.L., Paradis, P., Shenasa, H., and Juneau, C. (1986). Faster time to peak tension and velocity of shortening in right versus left ventricular trabeculae and papillary muscles of dogs. Circ Res *59*, 556-561.

Saari, J.T., and Johnson, J.A. (1980). Calcium kinetics in individual heart segments. Cardiovasc Res *14*, 731-734.

Santamore, W.P., and Dell'Italia, L.J. (1998). Ventricular interdependence: significant left ventricular contributions to right ventricular systolic function. Prog Cardiovasc Dis *40*, 289-308.

Santana, L.F., Cheng, H., Gomez, A.M., Cannell, M.B., and Lederer, W.J. (1996). Relation between the sarcolemmal Ca^{2+} current and Ca^{2+} sparks and local control theories for cardiac excitation-contraction coupling. Circ Res *78*, 166-171.

Saraiva, R.M., Chedid, N.G., Quintero, H.C., Diaz, G.L., and Masuda, M.O. (2003). Impaired beta-adrenergic response and decreased *L*-type calcium current of hypertrophied left ventricular myocytes in postinfarction heart failure. Braz J Med Biol Res *36*, 635-648.

Sarnoff, S.J., Braunwald, E., Welch, G.H., Jr., Case, R.B., Stainsby, W.N., and Macruz, R. (1958). Hemodynamic determinants of oxygen consumption of the heart with special reference to the tension-time index. Am J Physiol *192*, 148-156.

Sasaki, T., Inui, M., Kimura, Y., Kuzuya, T., and Tada, M. (1992). Molecular mechanism of regulation of Ca^{2+} pump ATPase by phospholamban in cardiac sarcoplasmic reticulum. Effects of synthetic phospholamban peptides on Ca^{2+} pump ATPase. J Biol Chem *267*, 1674-1679.

Sathish, V., Xu, A., Karmazyn, M., Sims, S.M., and Narayanan, N. (2006). Mechanistic basis of differences in Ca^{2+}-handling properties of sarcoplasmic reticulum in right and left ventricles of normal rat myocardium. Am J Physiol Heart Circ Physiol *291*, H88-96.

Scales, D.J. (1981). Aspects of the mammalian cardiac sarcotubular system revealed by freeze fracture electron microscopy. J Mol Cell Cardiol *13*, 373-380.

Schram, G., Pourrier, M., Melnyk, P., and Nattel, S. (2002). Differential distribution of cardiac ion channel expression as a basis for regional specialization in electrical function. Circ Res *90*, 939-950.

Shannon, T.R., Wang, F., Puglisi, J., Weber, C., and Bers, D.M. (2004). A mathematical treatment of integrated Ca dynamics within the ventricular myocyte. Biophys J *87*, 3351-3371.

Sheikh, F., Ross, R.S., and Chen, J. (2009). Cell-cell connection to cardiac disease. Trends Cardiovasc Med *19*, 182-190.

Singer, S.J., and Nicolson, G.L. (1972). The fluid mosaic model of the structure of cell membranes. Science *175*, 720-731.

Skomedal, T., Osnes, J.B., and Oye, I. (1982). Differences between alpha-adrenergic and beta-adrenergic inotropic effects in rat heart papillary muscles. Acta Pharmacol Toxicol (Copenh) *50*, 1-12.

Stankovicova, T., Szilard, M., De Scheerder, I., and Sipido, K.R. (2000). M cells and transmural heterogeneity of action potential configuration in myocytes from the left ventricular wall of the pig heart. Cardiovasc Res *45*, 952-960.

Stein, R.B., Gordon, T., and Shriver, J. (1982). Temperature dependence of mammalian muscle contractions and ATPase activities. Biophys J *40*, 97-107.

Stengl, M., Carmeliet, E., Mubagwa, K., and Flameng, W. (1998). Modulation of transient outward current by extracellular protons and Cd^{2+} in rat and human ventricular myocytes. J Physiol *511 (Pt 3)*, 827-836.

Stern, M.D., Song, L.S., Cheng, H., Sham, J.S., Yang, H.T., Boheler, K.R., and Rios, E. (1999). Local control models of cardiac excitation-contraction coupling. A possible role for allosteric interactions between ryanodine receptors. J Gen Physiol *113*, 469-489.

Stimers, J.R., and Dobretsov, M. (1998). Adrenergic stimulation of Na/K pump current in adult rat cardiac myocytes in short-term culture. J Membr Biol *163*, 205-216.

Strauer, B.E., Beer, K., Heitlinger, K., and Hofling, B. (1977). Left ventricular systolic wall stress as a primary determinant of myocardial oxygen consumption: comparative studies in patients with normal left ventricular function, with pressure and volume overload and with coronary heart disease. Basic Res Cardiol *72*, 306-313.

Subramani, S., Balakrishnan, S., Jyoti, T., Mohammed, A.A., Arasan, S., and Vijayanand, C. (2005). Force-frequency relation in frog-ventricle is dependent on the direction of sodium/calcium exchange in diastole. Acta Physiol Scand *185*, 193-202.

Suga, H., Sagawa, K., and Shoukas, A.A. (1973). Load independence of the instantaneous pressure-volume ratio of the canine left ventricle and effects of epinephrine and heart rate on the ratio. Circ Res *32*, 314-322.

Tandan, S., Wang, Y., Wang, T.T., Jiang, N., Hall, D.D., Hell, J.W., Luo, X., Rothermel, B.A., and Hill, J.A. (2009). Physical and functional interaction between calcineurin and the cardiac *L*-type Ca^{2+} channel. Circ Res *105*, 51-60.

Taylor, D.G., Parilak, L.D., LeWinter, M.M., and Knot, H.J. (2004). Quantification of the rat left ventricle force and Ca^{2+}-frequency relationships: similarities to dog and human. Cardiovasc Res *61*, 77-86.

Terkildsen, J.R., Niederer, S., Crampin, E.J., Hunter, P., and Smith, N.P. (2008). Using Physiome standards to couple cellular functions for rat cardiac excitation-contraction. Exp Physiol *93*, 919-929.

Toyofuku, T., Curotto Kurzydlowski, K., Narayanan, N., and MacLennan, D.H. (1994). Identification of Ser38 as the site in cardiac sarcoplasmic reticulum Ca^{2+}-ATPase that is phosphorylated by Ca^{2+}/calmodulin-dependent protein kinase. J Biol Chem *269*, 26492-26496.

Trafford, A.W., Diaz, M.E., and Eisner, D.A. (2001). Coordinated control of cell Ca^{2+} loading and triggered release from the sarcoplasmic reticulum underlies the rapid inotropic response to increased *L*-type Ca^{2+} current. Circ Res *88*, 195-201.

Trautwein, W., and Hescheler, J. (1990). Regulation of cardiac *L*-type calcium current by phosphorylation and G proteins. Annu Rev Physiol *52*, 257-274.

Undrovinas, A.I., Maltsev, V.A., Kyle, J.W., Silverman, N., and Sabbah, H.N. (2002). Gating of the late Na^+ channel in normal and failing human myocardium. J Mol Cell Cardiol *34*, 1477-1489.

Vila Petroff, M.G., Palomeque, J., and Mattiazzi, A.R. (2003). Na^+- Ca^{2+} exchange function underlying contraction frequency inotropy in the cat myocardium. J Physiol *550*, 801-817.

Volders, P.G., Sipido, K.R., Carmeliet, E., Spatjens, R.L., Wellens, H.J., and Vos, M.A. (1999). Repolarizing K+ currents I_{to1} and I_{Ks} are larger in right than left canine ventricular midmyocardium. Circulation *99*, 206-210.

Volk, T., Nguyen, T.H., Schultz, J.H., Faulhaber, J., and Ehmke, H. (2001). Regional alterations of repolarizing K+ currents among the left ventricular free wall of rats with ascending aortic stenosis. J Physiol *530*, 443-455.

Vornanen, M. (1992). Maximum heart rate of soricine shrews: correlation with contractile properties and myosin composition. Am J Physiol *262*, R842-851.

Wagner, J., and Keizer, J. (1994). Effects of rapid buffers on Ca^{2+} diffusion and Ca^{2+} oscillations. Biophys J *67*, 447-456.

Walker, L.A., and Buttrick, P.M. (2009). The right ventricle: biologic insights and response to disease. Curr Cardiol Rev *5*, 22-28.

Wang, H., Kohr, M.J., Traynham, C.J., Wheeler, D.G., Janssen, P.M., and Ziolo, M.T. (2008). Neuronal nitric oxide synthase signaling within cardiac myocytes targets phospholamban. Am J Physiol Cell Physiol *294*, C1566-1575.

Warda, M., Kim, H.K., Kim, N., Ko, K.S., Rhee, B.D., and Han, J. (2013). A matter of life, death and diseases: mitochondria from a proteomic perspective. Expert Rev Proteomics *10*, 97-111.

Warren, M., Guha, P.K., Berenfeld, O., Zaitsev, A., Anumonwo, J.M., Dhamoon, A.S., Bagwe, S., Taffet, S.M., and Jalife, J. (2003). Blockade of the inward rectifying potassium current terminates ventricular fibrillation in the guinea pig heart. J Cardiovasc Electrophysiol *14*, 621-631.

Watanabe, K., Abe, Y., Sato, S., Wahed, M., Wen, J., Narasimman, G., Ma, M., Ali, F., Saito, Y., Suresh, P.*, et al.* (2003). Contribution of sympathetic nervous system activity during administration of carvedilol in rats with dilated cardiomyopathy. J Cardiovasc Pharmacol *42 Suppl 1*, S93-97.

Watanabe, T., Delbridge, L.M., Bustamante, J.O., and McDonald, T.F. (1983). Heterogeneity of the action potential in isolated rat ventricular myocytes and tissue. Circ Res *52*, 280-290.

Weber, K.T., and Brilla, C.G. (1991). Pathological hypertrophy and cardiac interstitium. Fibrosis and renin-angiotensin-aldosterone system. Circulation *83*, 1849-1865.

Weis, T., Berger, F., and Borchard, U. (1993). A slowly inactivating transient outward current in rat ventricular myocytes. Pflugers Arch *425*, 184-186.

Wettwer, E., Amos, G., Gath, J., Zerkowski, H.R., Reidemeister, J.C., and Ravens, U. (1993). Transient outward current in human and rat ventricular myocytes. Cardiovasc Res *27*, 1662-1669.

Wier, W.G., Egan, T.M., Lopez-Lopez, J.R., and Balke, C.W. (1994). Local control of excitation-contraction coupling in rat heart cells. J Physiol *474*, 463-471.

Wier, W.G., and Yue, D.T. (1986). Intracellular calcium transients underlying the short-term force-interval relationship in ferret ventricular myocardium. J Physiol *376*, 507-530.

Winslow, R.L., Rice, J., Jafri, S., Marban, E., and O'Rourke, B. (1999). Mechanisms of altered excitation-contraction coupling in canine tachycardia-induced heart failure, II: model studies. Circ Res *84*, 571-586.

Youm, J.B., Choi, S.W., Jang, C.H., Kim, H.K., Leem, C.H., Kim, N., and Han, J. (2011). A computational model of cytosolic and mitochondrial [Ca^{2+}] in paced rat ventricular myocytes. Korean J Physiol Pharmacol *15*, 217-239.

Zahradnikova, A., Kubalova, Z., Pavelkova, J., Gyorke, S., and Zahradnik, I. (2004). Activation of calcium release assessed by calcium release-induced inactivation of calcium current in rat cardiac myocytes. Am J Physiol Cell Physiol *286*, C330-341.

Zhang, Z., Tendulkar, A., Sun, K., Saloner, D.A., Wallace, A.W., Ge, L., Guccione, J.M., and Ratcliffe, M.B. (2011). Comparison of the Young-Laplace law and finite element based calculation of ventricular wall stress: implications for postinfarct and surgical ventricular remodeling. Ann Thorac Surg *91*, 150-156.